Applied Computational Electromagnetics Society

Journal

Special Issue on the 8th International Conference on Computation in Electromagnetics (CEM 2011), Wroclaw, Poland

Guest Editor: Osama Mohammed

September 2011 Vol. 26 No. 9

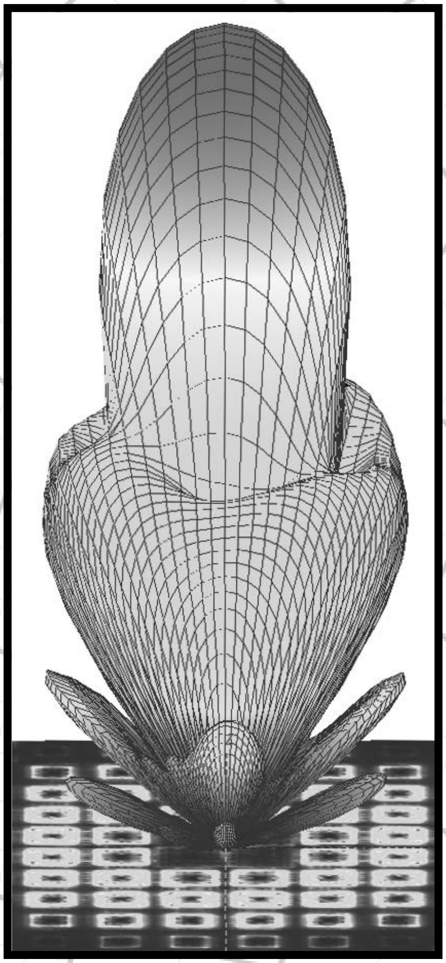

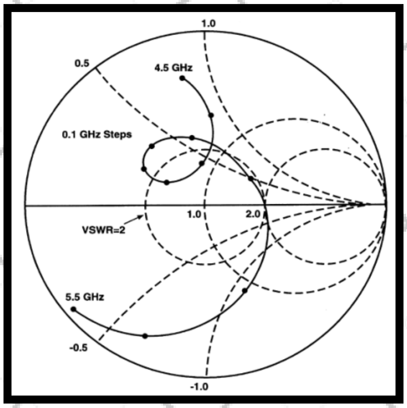

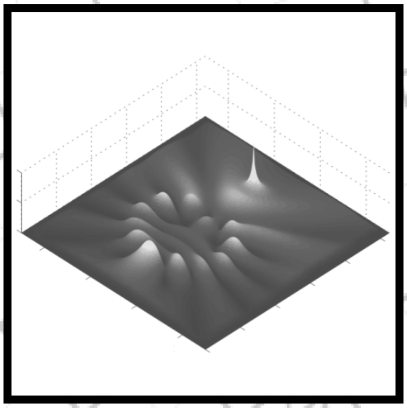

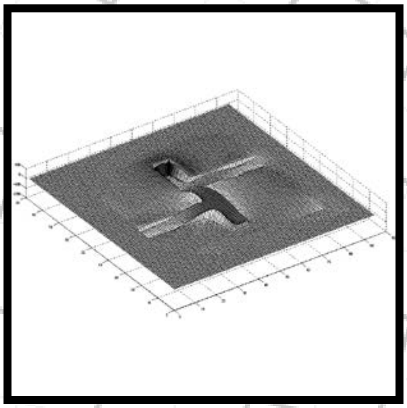

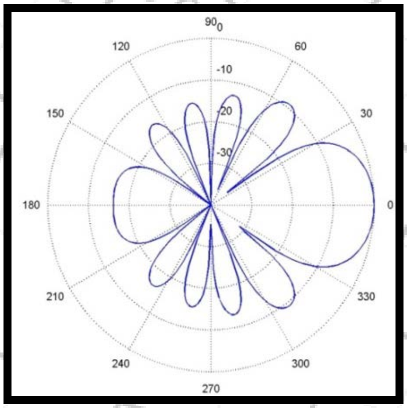

ISSN 1054-4887

GENERAL PURPOSE AND SCOPE: The Applied Computational Electromagnetics Society ***(ACES)*** Journal hereinafter known as the ***ACES Journal*** is devoted to the exchange of information in computational electromagnetics, to the advancement of the state-of-the art, and the promotion of related technical activities. The primary objective of the information exchange is to inform the scientific community on the developments of new computational electromagnetics tools and their use in electrical engineering, physics, or related areas. The technical activities promoted by this publication include code validation, performance analysis, and input/output standardization; code or technique optimization and error minimization; innovations in solution technique or in data input/output; identification of new applications for electromagnetics modeling codes and techniques; integration of computational electromagnetics techniques with new computer architectures; and correlation of computational parameters with physical mechanisms.

SUBMISSIONS: The ***ACES Journal*** welcomes original, previously unpublished papers, relating to applied computational electromagnetics. Typical papers will represent the computational electromagnetics aspects of research in electrical engineering, physics, or related disciplines. However, papers which represent research in applied computational electromagnetics itself are equally acceptable.

Manuscripts are to be submitted through the upload system of ***ACES*** web site http://aces.ee.olemiss.edu See "Information for Authors" on inside of back cover and at ***ACES*** web site. For additional information contact the Editor-in-Chief:

Dr. Atef Elsherbeni
Department of Electrical Engineering
The University of Mississippi
University, MS 386377 USA
Phone: 662-915-5382
Email: atef@olemiss.edu

SUBSCRIPTIONS: All members of the Applied Computational Electromagnetics Society are entitled to access and download the ***ACES Journal*** any published journal article available at http://aces.ee.olemiss.edu. Printed issues of the ***ACES Journal*** are delivered to institutional members. Each author of published papers receives a printed issue of the ***ACES Journal*** in which the paper is published.

Back issues, when available, are $50 each. Subscription to ***ACES*** is through the web site. Orders for back issues of the ***ACES Journal*** and change of address requests should be sent directly to ***ACES*** office at:

Department of Electrical Engineering
The University of Mississippi
University, MS 386377 USA
Phone: 662-915-7231
Email: aglisson@olemiss.edu

Allow four weeks advance notice for change of address. Claims for missing issues will not be honored because of insufficient notice, or address change, or loss in the mail unless the ***ACES*** office is notified within 60 days for USA and Canadian subscribers, or 90 days for subscribers in other countries, from the last day of the month of publication. For information regarding reprints of individual papers or other materials, see "Information for Authors".

LIABILITY. Neither ***ACES***, nor the ***ACES Journal*** editors, are responsible for any consequence of misinformation or claims, express or implied, in any published material in an ***ACES Journal*** issue. This also applies to advertising, for which only camera-ready copies are accepted. Authors are responsible for information contained in their papers. If any material submitted for publication includes material which has already been published elsewhere, it is the author's responsibility to obtain written permission to reproduce such material.

APPLIED COMPUTATIONAL ELECTROMAGNETICS SOCIETY JOURNAL

Special Issue on the Eighth International Conference on Computation in Electromagnetics (CEM 2011), Wroclaw, Poland

Guest Editor
Osama Mohammed

September 2011
Vol. 26 No. 9
ISSN 1054-4887

The ACES Journal is abstracted in INSPEC, in Engineering Index, DTIC, Science Citation Index Expanded, the Research Alert, and to Current Contents/Engineering, Computing & Technology.

The illustrations on the front cover have been obtained from the research groups at the Department of Electrical Engineering, The University of Mississippi.

THE APPLIED COMPUTATIONAL ELECTROMAGNETICS SOCIETY
http://aces.ee.olemiss.edu

EDITOR-IN-CHIEF

Atef Elsherbeni
University of Mississippi, EE Dept.
University, MS 38677, USA

ASSOCIATE EDITORS-IN-CHIEF

Sami Barmada
University of Pisa. EE Dept.
Pisa, Italy, 56126

Fan Yang
University of Mississippi, EE Dept.
University, MS 38677, USA

Mohamed Bakr
McMaster University, ECE Dept.
Hamilton, ON, L8S 4K1, Canada

Yasushi Kanai
Niigata Inst. of Technology
Kashiwazaki, Japan

Mohammed Hadi
Kuwait University, EE Dept.
Safat, Kuwait

Mohamed Abouzahra
MIT Lincoln Laboratory
Lexington, MA, USA

EDITORIAL ASSISTANTS

Matthew J. Inman
University of Mississippi, EE Dept.
University, MS 38677, USA

Anne Graham
University of Mississippi, EE Dept.
University, MS 38677, USA

EMERITUS EDITORS-IN-CHIEF

Duncan C. Baker
EE Dept. U. of Pretoria
0002 Pretoria, South Africa

Allen Glisson
University of Mississippi, EE Dept.
University, MS 38677, USA

David E. Stein
USAF Scientific Advisory Board
Washington, DC 20330, USA

Robert M. Bevensee
Box 812
Alamo, CA 94507-0516, USA

Ahmed Kishk
University of Mississippi, EE Dept.
University, MS 38677, USA

EMERITUS ASSOCIATE EDITORS-IN-CHIEF

Alexander Yakovlev
University of Mississippi, EE Dept.
University, MS 38677, USA

Erdem Topsakal
Mississippi State University, EE Dept.
Mississippi State, MS 39762, USA

EMERITUS EDITORIAL ASSISTANTS

Khaled ElMaghoub
University of Mississippi, EE Dept.
University, MS 38677, USA

Mohamed Al Sharkawy
Arab Academy for Science and
Technology, ECE Dept.
Alexandria, Egypt

Christina Bonnington
University of Mississippi, EE Dept.
University, MS 38677, USA

SEPTEMBER 2011 REVIEWERS

Ahmed Abdelrahman
Iftikhar Ahmed
Giulio Antonini
Deb Chatterjee
Jingyi Chen
Jorge Costa
Quizhao Dong
Joseph Harrison
Park Hyun Ho
Todd Hubing
Mousa Hussein
Yasushi Kanai
Nikolaos Kantartzis
Haider Khaleel
Fadi Khalil
Fernando Las Heras
David Lautru
Mengmeng Li
Sean Mercer
Mohammad Mohammadirad
Arash Nejadpak
Eesa Rahimi
Luca Rienzo
Mehdi Salehi
Binay Sarkar
Levent Sevgi
Hossein Torkaman
Hui Wang
Su Yan

THE APPLIED COMPUTATIONAL ELECTROMAGNETICS SOCIETY

JOURNAL

Vol. 26 No. 9 September 2011

TABLE OF CONTENTS

Boundary Element Computation of Line Parameters of On-chip Interconnects on Lossy Silicon Substrate

Dongwei Li [1, 2] and Luca Di Rienzo [2]

[1] State Key Laboratory of Electrical Insulation and Power Equipment
Xi'an Jiaotong University, Xi'an, 710049, P. R. China
dongwei.li@mail.polimi.it

[2] Dipartimento di Elettrotecnica
Politecnico di Milano, Milano, 20133, Italy
luca.dirienzo@polimi.it

***Abstract* ─** A BEM formulation is applied to the extraction of series parameters of interconnects on lossy silicon substrate. The numerical formulation can take into account both a semi-infinite homogeneous conductive substrate and a homogeneous conductive substrate of finite thickness with backside metallization and needs the discretization of only the contours of the traces.

***Index Terms* ─** Boundary element method, per-unit-length parameters, transmission lines, interconnects, silicon substrate.

I. INTRODUCTION

The broad-band transmission line behavior of interconnects on a lossy silicon substrate has been studied extensively by full-wave electromagnetic analysis [1-3] and, more recently, by quasistatic electromagnetic approaches [4-6]. The former, generally, is too time-consuming to be viable. In order to apply the latter, an accurate knowledge of the frequency-dependent per-unit-length (p.u.l.) parameters is needed and as far as the series parameters are concerned, different approaches have been proposed.

In [4], a general quasi-magnetostatic solver based on an integral formulation is adopted to compute the frequency-dependent distributed resistance and inductance parameters.

Alternatively, closed-form expressions for the series impedance parameters were derived using a complex image approach to approximate the effects of the complicated eddy-current loss mechanism in the silicon substrate [7, 8]. In the complex image approach, image conductors are placed at a frequency-dependent complex depth below the interconnects.

In the present paper, the same boundary integral formulation proposed in [9] for a different application is validated for the extraction of the series parameters of interconnects on a lossy silicon substrate, largely extending in this way the range of applications covered by this integral formulation. The adopted Green functions are those derived in [7, 8] and can take into account a semi-infinite homogeneous conductive substrate or a homogeneous conductive substrate of finite thickness with backside metallization. For the considered application, the proposed integral formulation has many advantages: compared to FEM or other volume approaches like that in [4], it does not need to discretize the substrate or to define a large enough computational domain and it only needs to discretize the surface of the conductors. Furthermore, compared to the existing approximate expressions (like those in [7, 8]) it can take into account any shape of the cross sections of the conductors, and not only rectangles. In Sec. III, some more details of the memory requirements will be given.

Submitted On: May 10, 2011
Accepted On: October 8, 2011

II. THE BEM FORMULATION

The BEM formulation proposed in [9] for the modeling of railway systems is adapted here to interconnect structures. For validation purposes, we apply it to a typical on-chip interconnect structure on silicon substrate (Fig. 1).

Under the hypothesis of a time-harmonic regime with angular frequency ω, vector fields are represented using phasors. Displacement currents are neglected.

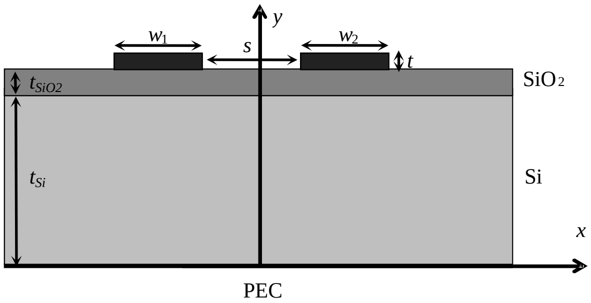

Fig. 1. The typical on-chip interconnect structure on silicon substrate.

Introducing the magnetic vector potential (MVP) as

$$\vec{B} = \mu\vec{H} = \nabla \times \vec{A}, \tag{1}$$

the electric field can be expressed as

$$\vec{E} = -j\omega\vec{A} - \nabla V, \tag{2}$$

where V is the electric scalar potential.

We decompose the MVP in a "source" and an "eddy" component

$$\vec{A}(\vec{r},t) = \vec{A}^s(\vec{r},t) + \vec{A}^e(\vec{r},t), \tag{3}$$

where the "source" component $\vec{A}^s$ satisfies the following condition

$$j\omega\vec{A}^s = -\nabla V, \tag{4}$$

so that the electric field is obtained in terms of the "eddy" component $\vec{A}^e$ only, i.e.

$$\vec{E} = -j\omega\vec{A}^e. \tag{5}$$

If the z-axis parallel of the cartesian coordinate system is parallel to the conductor's axis, the z-component of the magnetic field is zero ($\vec{H} = H_x\vec{e}_x + H_y\vec{e}_y$) and all the other fields are z-directed ($\vec{E} = E\vec{e}_z$, $\vec{A} = A\vec{e}_z$, $\vec{A^s} = A^s\vec{e}_z$, and $\vec{A}^e = A^e\vec{e}_z$).

Furthermore, $\nabla V = (\partial V/\partial x)\vec{e}_x$ and A^s are only functions of frequency and do not depend on coordinates y and z, being constant values for each conductor.

Application of the Coulomb's gauge to MVP leads to the Laplace equation for the MVP A_0 in air ($\Delta A_0 = 0$), so that the following boundary integral equation holds

$$\frac{1}{2}A_0 = \int_{c_1 \cup c_2} \left(A_0\frac{\partial g}{\partial n} - g\frac{\partial A_0}{\partial n}\right) dl, \tag{6}$$

where g is the Green's function of the Laplace equation out of the conductors. Taking into account the following boundary conditions

$$A_0 = A^e = A - A^s, \tag{7}$$

$$\frac{\partial A_0}{\partial n} = \mu_r\frac{\partial A}{\partial n} = \mu_r\frac{\partial A^e}{\partial n}, \tag{8}$$

where μ_r is the permeability of the conductor, we obtain

$$\frac{1}{2}A - \int_{c_1 \cup c_2}\left(A\frac{\partial g}{\partial n} - g\mu_r\frac{\partial A}{\partial n}\right) dl - \left(\frac{1}{2}A_k^s - A_1^s\int_{c_1}\frac{\partial g}{\partial n}dl - A_2^s\int_{c_2}\frac{\partial g}{\partial n}dl\right) = 0, \tag{9}$$

$$\frac{1}{2}A + \int_{c_k}(A\frac{\partial g_k}{\partial n} - g_k\frac{\partial A}{\partial n})dl = 0, \tag{10}$$

that can be solved together with Ampere's law

$$\int_{c_k}\frac{\partial A}{\partial n}dl = -\mu_k I_k. \tag{11}$$

In (10), g_k is the fundamental solution of the Helmholtz equation. Note that the terms A_k^s in (9) are out of the sign of the integrals since they are constant over the cross-sections of the corresponding conductors.

In order to take into account a lossy substrate with ground plane, a complex image approximation of the Green’s function can be used [7, 8]

$$g = \frac{1}{2\pi} log\sqrt{(x-x')^2+(y+y'+d)^2} + g_0, \quad (12)$$

$$g_0 = \frac{1}{2\pi}\log\left(\frac{1}{|r|}\right), \quad (13)$$

with d = (1-j)·δ in the case of a semi-infinite homogeneous conductive substrate and d = (1-j)·δ ·tanh[(1+j)t_{Si}] in the case of finite thickness with backside metallization, where δ is the skin depth in the substrate and t_{Si} is the substrate thickness. If a multilayer model for the substrate is to be considered, d can be computed from the surface impedance of the substrate as in [8].

The entries of the p.u.l. impedance matrix can be finally computed by means of the following formulas

$$Z_{hh} = \frac{j\omega A_h^s}{I_h}\bigg|_{I_k=0}; \text{ (14a) } Z_{hk} = \frac{j\omega A_k^s}{I_h}\bigg|_{I_k=0}. \quad (14)$$

In this work, the surface boundary integral equations (1-2) are discretized by means of constant boundary elements [10-11]. In order to check if the presence of corners introduces inaccuracies, the case of the two identical rectangular conductors without the presence of the lossy substrate is considered. Our BEM results are compared with FEM results obtained using a commercial software [12]. A good agreement is obtained in the frequency range 1-10 GHz (errors in resistance lower than 0.5 % and errors in inductance lower than 0.1 %).

III. NUMERICAL SIMULATIONS

For validation purposes, first a single copper microstrip line of a rectangular cross-section (Fig. 2) is considered. Our results are compared with those given by the commercial FEM software [12] (Figs. 3-4). FEM simulations are obtained using a mesh of 154987 triangles and requires 1.4 GByte of RAM, while BEM simulations use 100 nodes and 538 MByte of RAM.

In order to show the validity of the proposed method for any shape of the conductor cross-sections, the case of a single mictrostrip line of trapezoidal cross-section is also considered (Figs. 5-7). A good agreement with FEM results is obtained.

The self and mutual resistance and inductance parameters for the coupled on-chip interconnect structure of Fig. 1 on a high conductivity (10^4 S/m) and a medium conductivity (16.66 S/m) silicon substrate with t_{Si} = 300 μm thickness analysed in [6] have been computed by means of the proposed formulation (Figs. 8-11). The dimensions of the cross section of each conductor are $w_1 = w_2$ = 2 μm, t = 1 μm, and the separation between the conductors is s = 2 μm. Results are compared with those reported in [6] and those obtained by means of the FEM commercial software [12]. As it can be noted, BEM results are in good agreement with the FEM results, while the self resistance computed as proposed in [6] is not accurate (Fig. 8).

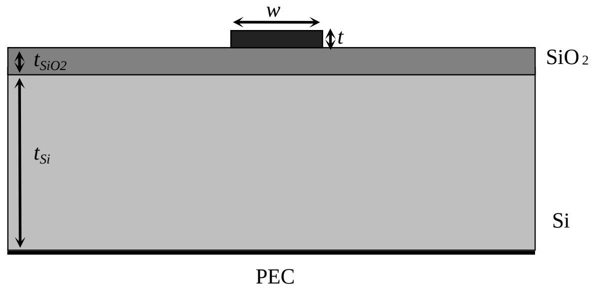

Fig. 2. A single copper (σ = $5.8 \cdot 10^7$ S/m) microstrip line with w = 4 μm, t = 1 μm, t_{SiO2} = 2 μm and t_{Si} = 300 μm.

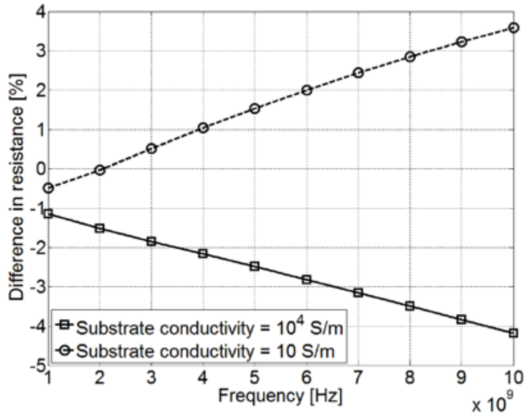

Fig. 3. Relative difference in resistance (FEM-BEM).

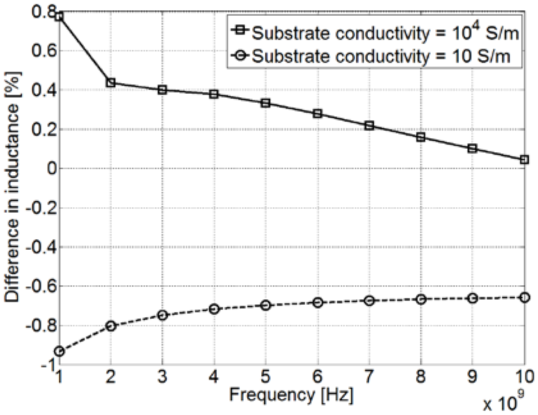

Fig. 4. Relative difference in inductance (FEM-BEM).

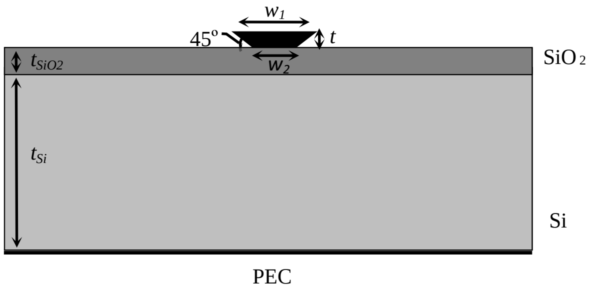

Fig. 5. A single copper microstrip line of trapezoidal cross-section with w_1 = 4 μm, w_2 = 2 μm, t = 1 μm, t_{SiO2} = 2 μm and t_{Si} = 300 μm.

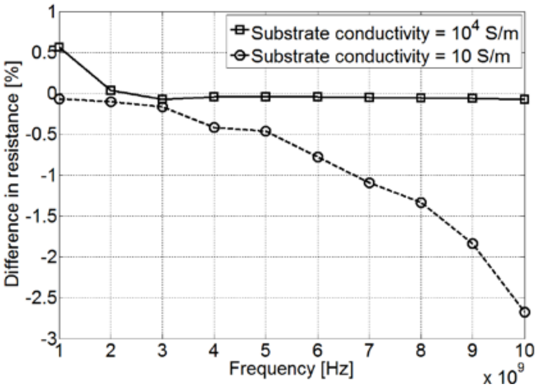

Fig. 6. Relative difference in resistance (FEM-BEM).

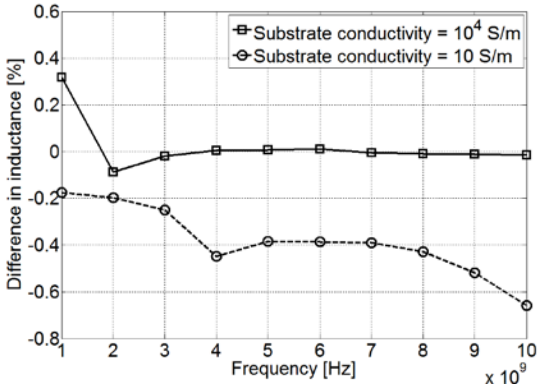

Fig. 7. Relative difference in inductance (FEM-BEM).

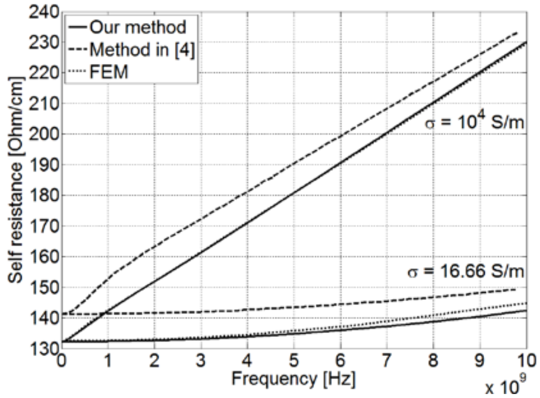

Fig. 8. Self resistance of symmetric coupled interconnects of Fig. 1.

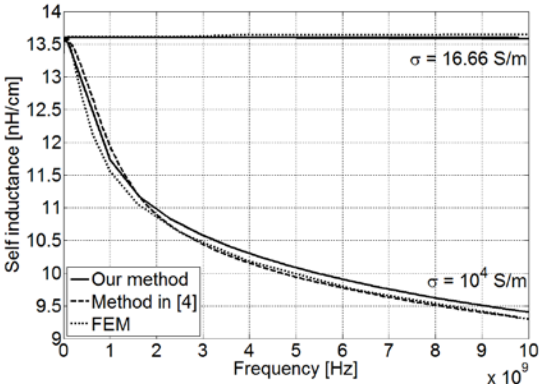

Fig. 9. Self inductance of symmetric coupled interconnects of Fig. 1.

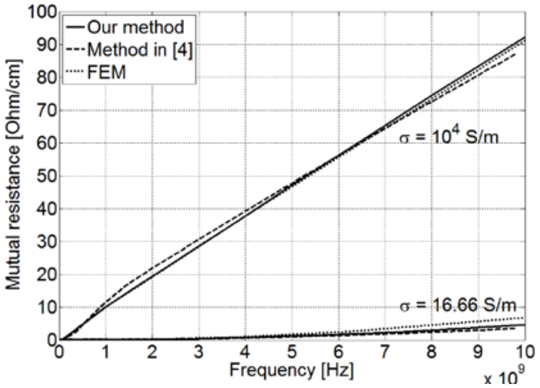

Fig. 10. Mutual resistance of symmetric coupled interconnects of Fig. 1.

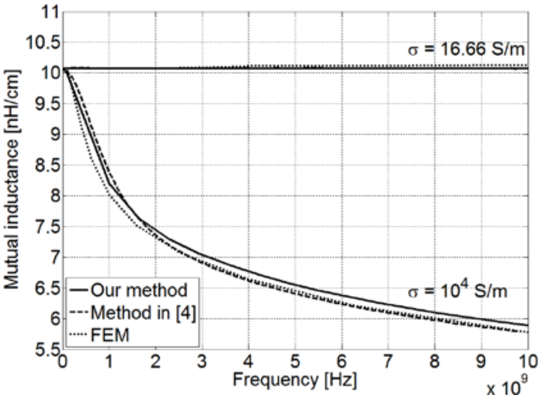

Fig. 11. Mutual inductance of symmetric coupled interconnects of Fig. 1.

BEM results are also compared with FEM results for self and mutual resistances of asymmetric interconnects, obtaining good agreement (Figs. 12-17). The following numerical values are considered (Fig. 1): $w_1 = 2$ µm, $w_2 = 1$ µm, $t = 1$ µm, $s = 2$ µm, $t_{SiO2} = 3$ µm, $t_{Si} = 300$ µm, $\sigma = 3.5\text{x}10^7$ S/m, and $\sigma_{Si} = 10^4$ S/m.

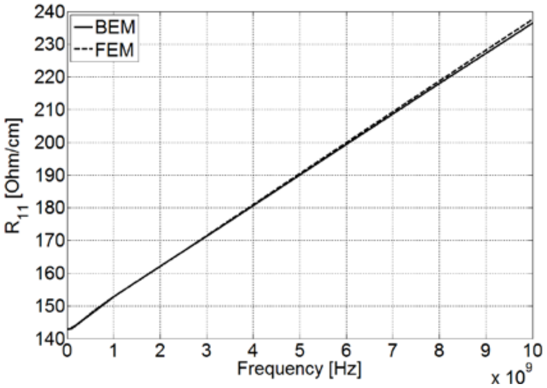

Fig. 12. Self resistance R_{11} for asymmetric coupled interconnects.

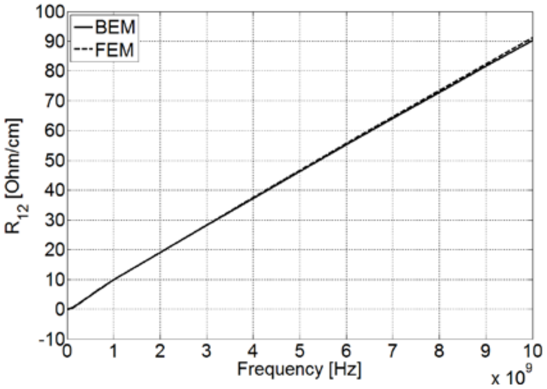

Fig. 13. Mutual resistance R_{12} for asymmetric coupled interconnects.

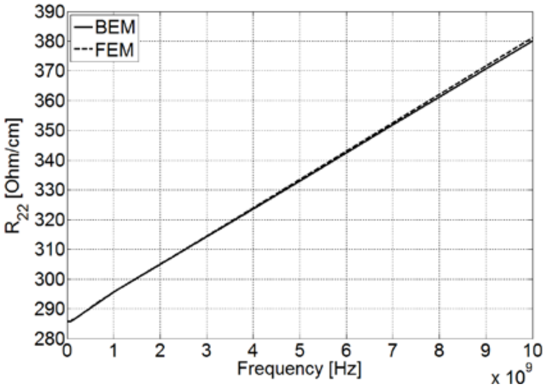

Fig. 14. Self resistance R_{22} for asymmetric coupled interconnects.

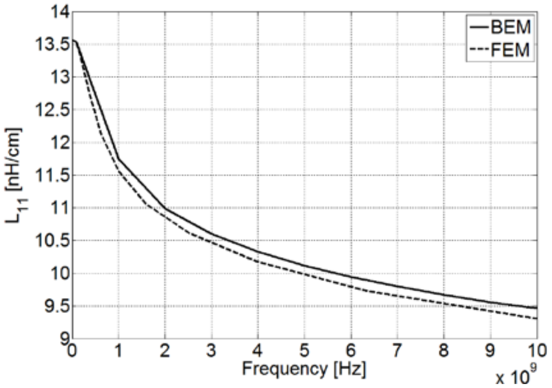

Fig. 15. Self inductance L_{11} for asymmetric coupled interconnects.

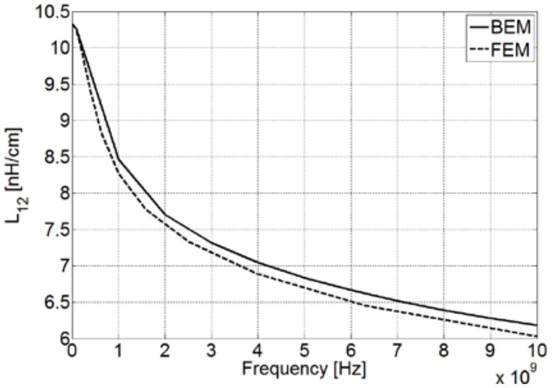

Fig. 16. Mutual inductance L_{12} for asymmetric coupled interconnects.

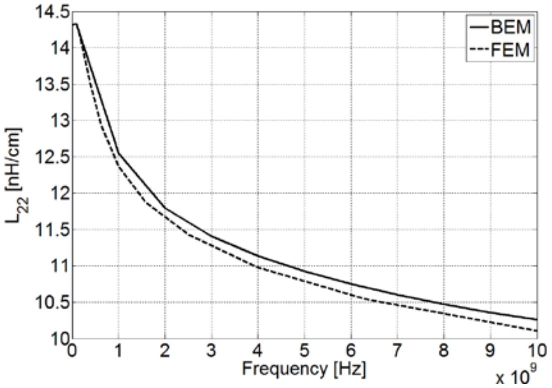

Fig. 17. Self inductance L_{22} for asymmetric coupled interconnects.

IV. CONCLUSION

The proposed formulation is proven to be a good compromise between general quasi-magnetostatic numerical solvers and approximate analytical expressions. The BEM formulation has been validated by comparison with other techniques for some typical test problems and the advantages of the proposed approach in terms of memory requirement have been shown. Future work will deal with the extension of the formulation to multilayer silicon substrates, 3D geometries, the modeling of roughness of the surfaces of the traces, and the implementation of surface impedance boundary conditions in order to further reduce the computational cost.

REFERENCES

[1] E. Grotelüschen, L. S. Dutta, and S. Zaage, “Full-Wave Analysis and Analytical Formulas for the Line Parameters of Transmission Lines on Semiconductor Substrates,” *Integration, VLSI J.*, vol. 16, pp. 33-58, 1993.

[2] A. G. Chiariello, A. Maffucci, G. Miano, F. Villone, and W. Zamboni, “High-Frequency Full-Wave Analysis of Interconnects with Inhomogeneous Dielectrics through an Enhanced Transmission Line Model,” *Applied Computational Electromagnetic Society (ACES) Journal*, vol. 23, no. 1, pp. 31 - 38, March 2008.

[3] K. Chatterjee, “A Stochastic Algorithm for the Extraction of Partial Inductances in IC Interconnect Structures,” *Applied Computational Electromagnetic Society (ACES) Journal*, vol. 21, no. 1, pp. 81 - 89, March 2006.

[4] J. Zheng, V. K. Tripathi, and A. Weisshaar, “Characterization and Modelling of Multiple Coupled On-Chip Interconnects on Silicon Substrate,” *IEEE Trans. Microwave Theory Tech.*, vol. 49, no. 10, 2001.

[5] J. Zheng, Y.-C. Hahm, V. K. Tripathi, and A. Weisshaar, “CAD-Oriented Equivalent Circuit Modeling of On-Chip Interconnects on Lossy Silicon Substrate,” *IEEE Trans. Microwave Theory Tech.*, vol. 48, pp. 1443-1451, 2000.

[6] A. Tripathi, Y. C. Hahm, A. Weisshaar, and V. K. Tripathi, “A Quasi-TEM Spectral Domain Approach for Calculating Distributed Inductance and Resistance of Microstrip on Si–SiO$_2$ Substrate,” *Electron. Lett.*, vol. 34, pp. 1330-1331, 1998.

[7] A. Weisshaar, H. Lan, and A. Luoh, “Accurate Closed-Form Expressions for the Frequency-Dependent Line Parameters of On-Chip Interconnects on Lossy Silicon

Substrate," *IEEE Adv. Packag.*, vol. 25, no. 2, 2002.

[8] A. Weisshaar and A. Luoh, "Closed-Form Expressions for the Series Impedance Parameters of On-Chip Interconnects on Multilayer Silicon Substrates", *IEEE Adv. Packag.*, vol. 27, no. 1, 2004.

[9] L. Di Rienzo, Z. Zhang, and S. A. Pignari, "Boundary Element Computation of Per-Unit-Length Series Parameters of Railway Lines," *IEEE Trans. Electromagn. Compat.*, vol. 51, no. 3, pp. 825-832, 2009.

[10] J. Shen, *Computational Electromagnetics Using Boundary Elements*, Southampton: CMP, 1995.

[11] C. A. Brebbia, J. C. F. Telles, and L. C. Wrobel, *Boundary Element Techniques*. New York: Springer-Verlag, 1984.

[12] Maxwell 2D v. 11, *Ansoft Corporation*, 1984-2006; software available at: http://www.ansoft.com.

Dongwei Li is currently a Ph.D. candidate of both Politecnico di Milano - Dipartimento di Elettrotecnica and Xi'an Jiaotong University - State Key Laboratory of Electrical Insulation and Power Equipment. His research interests focus on boundary element analysis of eddy current problems and electromagnetic modeling of innovative current sensors.

Luca Di Rienzo received the Laurea and Ph.D. degrees in Electrical Engineering from Politecnico di Milano, Milan, Italy, in 1996 and 2001, respectively. From 2000 to 2004, he was a Research Assistant with the Dipartimento di Elettrotecnica of Politecnico di Milano, where he has been an Assistant Professor since 2005. At present, his research interests are in the field of computational electromagnetics and include electromagnetic inverse problems, surface impedance boundary conditions, and the boundary element method. Dr. Di Rienzo is a member of the IEEE EMC Society and the International Compumag Society (ICS).

Evaluation of Circular Aperture Transmission Coefficients in the Presence Of Obscurations

J. G. Davis, P. Shakespeare, and N. Kiley

BAE Systems, Military Air Solutions, Electromagnetic Engineering, W423
Warton Aerodrome, Preston, PR4 1AX, United Kingdom
john.g.davis@baesystems.com

Abstract **—** This paper describes a novel parametric approach to the simulation of circular aperture transfer functions in the presence of obscurations at microwave frequencies. A novel virtual 'absorbing box' power loss integration technique is applied to successfully demonstrate its validity for conditions where the aperture diameter approaches one tenth of the plate largest dimension.

Index Terms **—** Aperture, diffraction, transmission coefficient.

I. INTRODUCTION

The formulation of the transmission coefficient for a circular aperture in a plate of finite cross section has been the subject of much scientific interest over the years [1, 2]. The complex nature of the complete solution has lead to a variety of approximate empirical formulations based on uni-mode propagation models. Amongst these is the simple Huygens wavefront approach adopted by Koch/Airy which produces an impressive correlation with experimental data [1]. However, this method breaks down for larger apertures where multi-mode propagation prevails. Hybrid solutions attributable to Seshadri & Wu [3], based on a truncated form of the infinite modal series, have been formulated to accommodate larger apertures. Historically, these are preferred to rigorous solutions incorporating all propagating and evanescent modes as these require the implementation of intricate mode matching techniques [4]. In this paper, a novel, alternative parametric solution based on the Seshadri formulation is proposed. This yields an elementary basis function which can be readily applied to bounded apertures both in isolation and in cavity based mode stirred reverberation conditions. The development of the parametric algorithm is described first followed by comparisons with a transmission line method (TLM) solver simulation, which employs a novel means of eliminating diffraction at the aperture plate edges. The method is further expanded to incorporate diffraction shadow attenuation effects and multiple reflection modulation arising from obscurations.

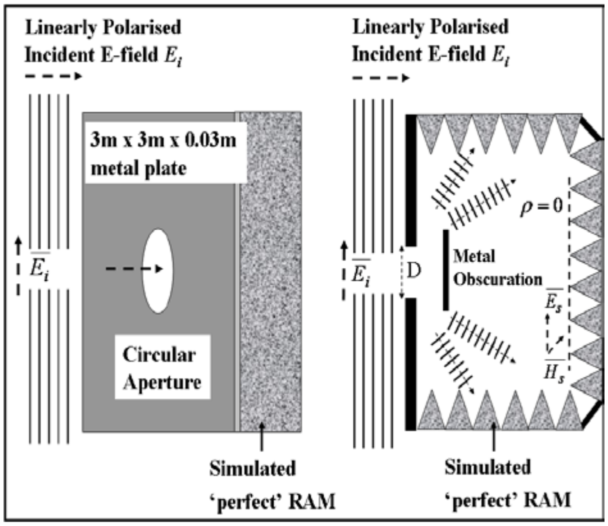

Fig. 1. TLM numerical circular aperture model showing the virtual absorbing box used for edge diffraction elimination.

II. APERTURE FINITE DIFFERENCE SIMULATIONS

The first step in producing the aperture transmission numerical solution: comprise a reduction in the considerable $9\ m^3$ modelled mesh volume in order to minimise simulation run times.

Submitted On: May 23, 2011
Accepted On: October 20, 2011

1054-4887 © 2011 ACES

As the aperture is a symmetrical shape with two planes of symmetry, it is possible to define orthogonal electric and magnetic wall boundary conditions in order to reduce the computational domain by a factor of 3 quarters. Secondly, as the aperture plate dimensions are limited within the modelling constraints of the chosen transmission line method (TLM) solver, there may be an undesirable leakage of energy around the plate periphery due to edge diffraction. Suppression of this phenomena, however, may be effected via the introduction of a virtual 'absorbing box' coincident with the plate edges and boundary mesh perfect matched layer shown in Fig. 1. If the box walls are configured within the TLM solver as metallic sheets with a 377Ω surface impedance (i.e equal to the characteristic impedance of unbounded propagating waves with the box volume), then the reflection coefficient at the interior box walls will be zero. Under these circumstances all energy impinging on the interior will be absorbed at the walls. Conversely, the exterior boundaries of the box present a surface impedance of zero to any external waves diffracted around its periphery, thus resulting in total external reflection. Under these conditions, the interior walls behave as a perfect matched layer (PML) and the exterior walls as perfect reflecting surfaces. The computation of the aperture transmitted power may then be effected via the selection of the CST microstripes, the TLM solver 'integrate loss over volume' and 'integrate loss over surface' output options, thus enabling computation of the aperture transmission coefficient from the ratio of energy transmitted to that absorbed in the RAM enclosure. This absorbing mechanism is analogous to that of radar absorbent material (RAM) found in an anechoic chamber as illustrated symbolically in Fig. 1.

A. Absorbing box simulation

Essentially, the aperture transmission coefficient is simulated via exploitation of the CST microstripes, in-built wall loss calculation capability [5]. The configuration of Fig. 1 used for this purpose, comprises a perfect RAM absorbing box modelled as a basic 'enclosure' shape with 3 mm thick walls. The enclosure aperture face is formed from a 3 mm thick copper plate with 400 mm diameter circular aperture located at its centre. The materials chosen to configure the RAM enclosure and aperture respectively, i.e copper plate of conductivity 5.8 x 10^7 S/m and absorbing box of 377Ω surface impedance, ensured total containment and absorption of transmitted energy by the enclosure walls. The plane wave signal excitation, derived from a gaussian pulse source positioned 0.5 m in front of the aperture, was monitored in *E* and *H-field* cartesian component form at various points along the absorbing enclosure axis. The cuboidal PML simulation boundary, comprising dimensions 10% greater than the complete absorbing enclosure, was discretised to provide sufficient plate and aperture edge resolution without incurring excessive run times. A summary of all modelling parameters including system bandwidth, run and time step duration are detailed in Table 1 above.

Table 1: Aperture model simulation parameters

CST Simulation Parameter	**Value**
Simulation Bandwidth	0.01 to 3 GHz
Run Duration	10 μs
No. of timesteps	6153
Total run time	30 mins
Number of cells	212,589
Maximum Cell Size	9.88 mm
Metal Plate Dimensions	3.x 3.x 0.003 m
Absorbing Enc. Dimensions	3.x 3. x 0.5 m
Conductivity (Metal Plate)	5.8x10^{-7} S/m
Encl. Surface Impedance	377 Ω

III. TRANSMISSION COEFFICIENT MODELLING

The TLM solver, simulated transmission coefficient, is defined as the ratio of the total power transmitted through the aperture (i.e that dissipated on the inside of the absorbing box) to that power incident on the aperture of diameter D, as derived from the Poynting theorem, i.e :

$$S = \frac{\frac{1}{2}\mathrm{Re}\iint\left(\overline{E_s}\times\overline{H_s}^{*}\right)dA}{\pi D^2\left|E_i\right|^2/\eta_0}, \qquad (1)$$

where $\mathbf{E_s}$ and $\mathbf{H_s}$ are the electric and magnetic vector fields on the inside surface of the 'perfect RAM' absorbing box in Fig. 1 and $\mathbf{E_i}$ is the incident *E-field* at the aperture. The transmission coefficients S, attributable to the theoretical formulations of Seshadri [3] and Andrewski [6],

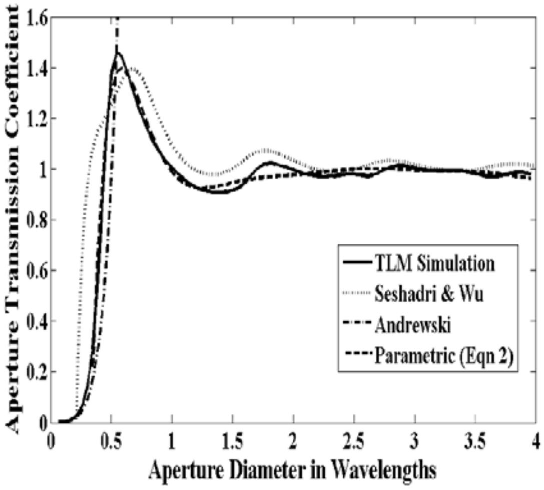

Fig. 2. Comparison of simulated transmission coefficients showing theoretical, simulated, and parametric solutions.

are plotted along with the equivalent TLM simulation as a function of the aperture diameter in wavelengths in Fig. 2. A comparison of the resulting profiles reveals a strong correlation between theoretical and modelled responses at the start of the wave number (kD) range for the Andrewski formulation (i.e 0<kD<1/pi), and in the latter part of the range for the Seshadri case (3/pi<kD<10/pi). These features enable a hybrid solution (2) to be formulated combining the functional dependencies attributable to both [3] and [6], thereby yielding an equivalent parametric response for the composite range as :

$$A_p(\omega) = \frac{\begin{array}{c}1 - \gamma^{-3/2} a_1(\sin\varphi) + \gamma^{-2}(a_2 + a_3 \sin 2\varphi) - \ldots \\ \ldots.\, a_6(a_4 + a_5 \sin 2\varphi)\gamma^{-5/2}\end{array}}{a_7 K \exp - [a_8(a_9 + K)]/\pi}, \quad (2)$$

where $\gamma = D/\lambda$, $\varphi = 2\gamma - \pi/4$. The coefficients a_n in the parametric function, optimised to provide the ‘best fit' using the inversion algorithm specified in [10], are defined as:

$$a = \begin{bmatrix} -0.163 & -0.950 & 0.039 & -1.042 \ldots \\ -0.058 & 0.490 & -0.744 & 0.601 & -1.118 \end{bmatrix}. \quad (3)$$

A comparison between the optimised parametric and TLM simulated responses in Fig. 2 yields an impressive correlation, demonstrating the validity of the function of (2) as an elementary, universal transmission coefficient representation applicable to circular apertures of any dimension.

IV. APERTURE OBSCURATION MODELLING

The modelling of aperture transmission coefficients in the presence of blockages or obscurations is an important element in the analysis of the energy transfer between cavities and equipment bays in aircraft and ships, as the geometry of adjoining bay openings and physical obstructions within its proximity, ultimately determines the extent of the internal energy transfer within the structure [7, 8]. In this section, a method of modelling the perturbing effect of a metal plate, positioned in close proximity to a circular aperture, is established for any given aperture diameter in wavelengths.

A. Obscuration theory

The modulation of the open aperture transmission coefficient for a square obscuration plate twice the width of the aperture shown in Fig. 1, may be modelled as the convolution of three distinct functions, i.e the open aperture transfer algorithm of (2), a blockage or obscuration function, and a multiple reflection standing wave function. The obscuration function, may be derived via application of the standard geometric diffraction theory to the resultant scattered signal at the plate edges. This analysis requires the evaluation of the Fresnel-Kirchoff diffraction parameter [9] at the obscuration plate boundaries. Application of this theory to the upper and lower knife edges in Fig. 3 yields :

$$v_u(\omega) = \alpha_u\left[\frac{\omega L d}{\pi c_0(L+d)}\right]; \; v_l(\omega) = \alpha_l\left[\frac{\omega L d}{\pi c_0(L+d)}\right], \quad (4)$$

where the orthogonal symmetry of the box and aperture, enables an identical result to be derived for the plate left and right, vertical edges. The complex Fresnel integrals, representing the sum of all secondary Huygens sources on each of the upper and lower plate edges may be expressed in terms of their diffraction parameters v_u as :

$$F_u(\omega) = \int_0^{v_u(\omega)} \exp\left(-j\pi v^2\right) dv, \quad (5)$$

and similarly for v_l. The resultant scattered field in the shadow region beyond the plate in Fig. 3, attributable to a given edge, may be derived via integration of the Fresnel parameters v in (5) as :

$$E = 0.5(1 + j)(0.5(1 - j) - F(\omega)). \qquad (6)$$

For which, the total diffracted field located at the intersection of position vectors r_2^u and r_2^l in Fig. 3, corresponding to the vector summation of *E-fields* E_u and E_l may be expressed thus :

$$E_T(\mathbf{r},\omega) = \frac{E_u(v_u)e^{j[\omega t - \beta_0 r_u]}}{r_1^u r_2^u} + \frac{E_l(v_l)e^{j[\omega t - \beta_0 r_l]}}{r_1^l r_2^l}, \qquad (7)$$

where β_0 is the free space propagation coefficient, and the vectors $r_u = r_u^1 + r_u^2$ and $r_l = r_l^1 + r_l^2$ represent the total path length from source to measurement position via the plate upper and lower edges. Normalising the summation of *E-field* components at all position vectors in (7) for identical upper / lower & left / right orthogonal edge pairings, enables the total energy propagating into the shadow region to be expressed as a fraction of total transmitted power through the aperture, i.e

$$H(\omega) = 2\sum_n^N \left|E_T(\mathbf{r}_n,\omega)\right|^2 \Big/ \left|E_o\right|^2 \cong pe^{[-r\omega]} + qe^{[-s\omega]}, \qquad (8)$$

where $p = E_u(v_u)/r_1^u r_2^u$; $q = E_l(v_l)/r_1^l r_2^l$ etc. The parametric formulation on the RHS in (8), equivalent to the finite exponential series summation on the left, provides an approximate representation of the total diffracted field energy at all N sample positions within the modelled mesh space for both edge pair combinations. A close approximation to the rigorous solution may now be acquired via application of the inversion process [10] to yield coefficients p, q, r, s which provide an optimum fit to the interpolation surface defined in (8). In essence, this function, when convolved with the open aperture formulation in (2), defines that fraction of total incident *E-field* energy which propagates beyond the plate's geometric obstruction to ultimately be absorbed by the walls of the RAM enclosure.

B. Standing wave function

The characteristic standing wave pattern arising from the multiple reflections between aperture and plate [11] is deduced from the ray tracing schematic in Fig. 4 and may be expressed by the infinite time domain series:

$$r(t) = (1 - \rho_A) \otimes \left[\delta(t - t_0) - p_0 p_A \delta(t - 3t_0) + \ldots\right], \qquad (9)$$

where ρ_o and ρ_A represent the equivalent reflection coefficients at plate and aperture impedance discontinuities respectively, whilst $t_0 = d/c_0$ is the propagation delay over distance d between aperture and plate. The resultant standing

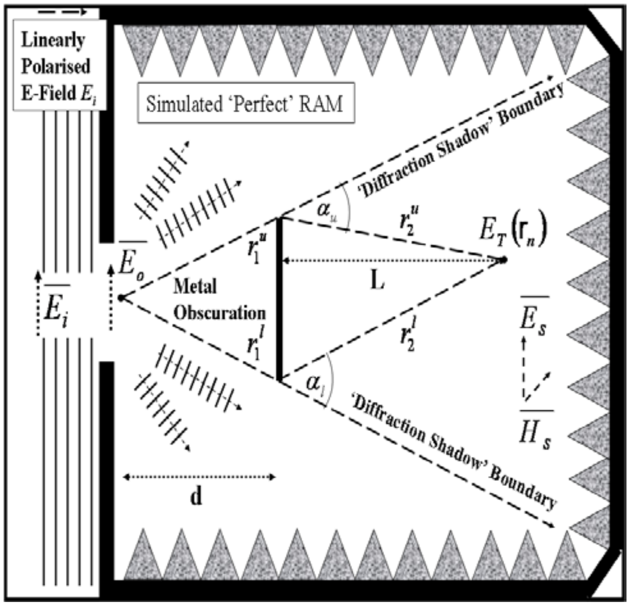

Fig. 3. Schematic showing Fresnel diffraction and plate obscuration geometry used to calculate the modified aperture transmission coefficient.

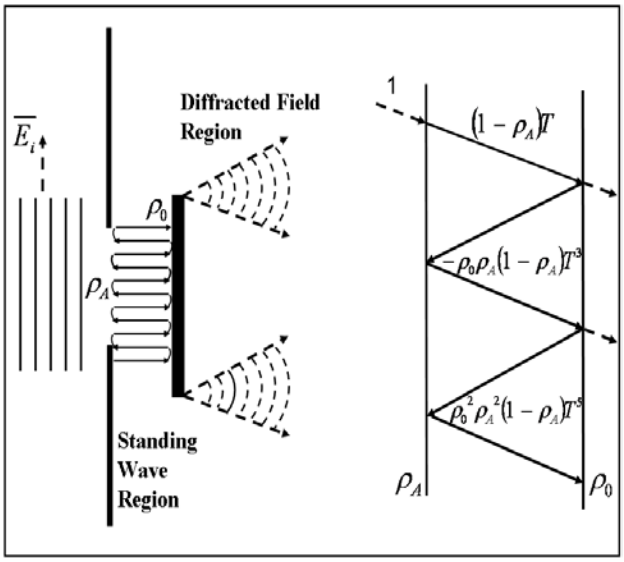

Fig. 4. Schematic of circular aperture and obstruction showing equivalent signal flow path model for multiple reflection and standing wave pattern evaluation.

wave function frequency dependence is derived from the FFT of (9) as:

$$R(\omega) = \left(1-\rho_A(\omega)\right)\left[T - \rho_0(\omega)\rho_A(\omega)T^3 + ...\right], \quad (10)$$

where $T = \exp(-j\omega d/c_0)$ is the mesh space propagation coefficient. Note, in (10), $\rho_o(\omega) \approx -1$, is assumed to equal the reflection coefficient of the plate metallic conducting surface, whilst $\rho_A(\omega) \approx 1 - A_p(\omega)$, is derived via application of the unity property theorem [12] to the aperture transmission coefficient in (2). Finally, having evaluated the respective open aperture, standing wave pattern, and plate obscuration functions, the resultant transmission coefficient for the incident field $\boldsymbol{E_i}$ may be expressed as :

$$S_{OB}(\omega) = \eta_0 \left|A_p(\omega)H(\omega)R(\omega)\right|^2 \Big/ \left|E_i\right|^2 . \quad (11)$$

C. Obscuration simulation results

The obscuration coefficient of (11) was simulated using the CST microstripes TLM solver for a metal plate 50% larger than the aperture at displacements of 0.4 m, 0.6 m, and 0.8 m. The results are plotted and compared with their parametric, theoretical counterparts in Figs. 5, 6 and 7. Here, the attenuating effect of the plate and standing wave pattern attributable to the infinite series of reflections between impedance discontinuities at the aperture and plate itself are in evidence. Note, the decrease in the standing wave amplitude for an increase in plate displacement (d) from 0.4 to 0.8 m, and subsequent reduction in the diffraction boundary angle α, as less transmitted flux is caught in the plate shadow region and reflected. For large separations, as $d \to \infty$, T approaches zero and R tends to unity, the response asymptotically approaches that obtained in the absence of the plate. Both separations exhibit a good agreement between simulation and parametric theory.

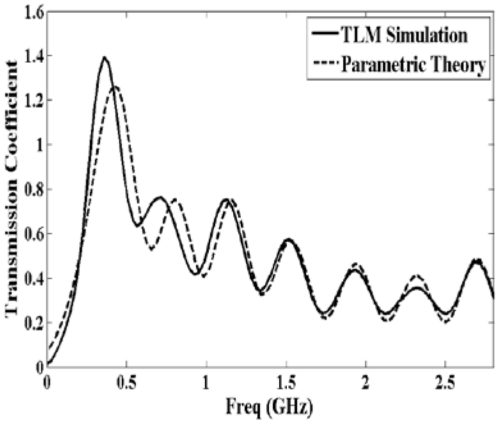

Fig. 5. Comparison between TLM simulation and parametric solution for a circular aperture model with obscuration plate at 400 mm separation.

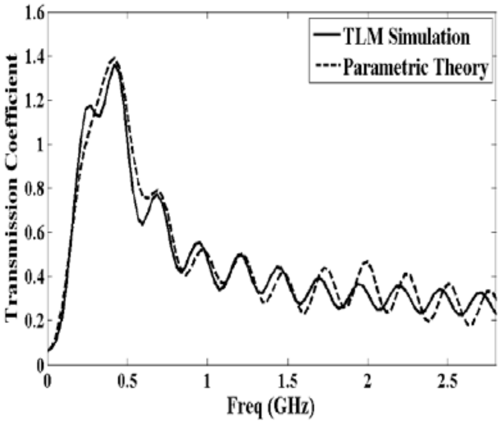

Fig. 6. Comparison between TLM simulation and parametric solution for a circular aperture model with obscuration plate at 600 mm separation.

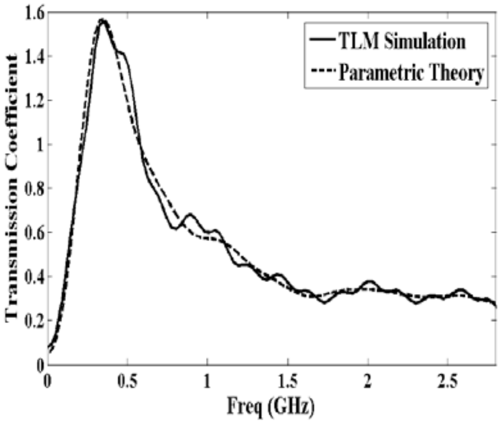

Fig. 7. Comparison between TLM simulation and parametric solution for a circular aperture model with obscuration plate at 800 mm separation.

V. CONCLUSIONS

This paper demonstrates how parametric expressions can greatly simplify the non-trivial computation of energy transfer through a circular aperture in a metal plate. The validity was confirmed via comparison with a standard TLM commercial solver model incorporating a virtual ‘absorbing box’ loss analysis algorithm. The method was further extended to accommodate modulation arising from the presence of obscurations, where both the characteristic geometrical shadowing and standing wave pattern associated with multiple reflections were recreated.

REFERENCES

[1] G. F. Koch and D. K. Kolbig, “Transmission Coefficient of Elliptical and Rectangular Apertures for Electromagnetic Waves,” *IEEE Trans. Ant. and Prop.*, vol. AP-16, no. 1, Jan 1968.

[2] S. T. Imeci, F. Altunkilic, J. R. Mautz, and E. Arvas, “Transmission through an Arbitrarily Shaped Aperture in a Conducting Plane Separating Air and a Chiral Medium,” *Applied Computational Electromagnetic Society (ACES) Journal*, vol. 25, no. 7, pp. 587 – 599, July 2010.

[3] S. R. Seshadri and T. T. Wu, “High Frequency Diffraction of Electromagnetic Wave by a Circular Aperture in an Infinite Plane Conducting Screen,” *IRE Trans. Ant. Prop*, vol. AP-8, 1960.

[4] K. Hongo and Q. A. Naqvi, Diffraction of Electromagnetic Waves by Disk and Circular Hole in a Perfectly Conducting Plane, *Progress In Electromag. Research,* PIER 68, 113–150, 2007.

[5] CST STUDIO SUITE 2011, “Integrating Simulation Technology,” *Microwave Journal*, vol. 53, no. 12, p. 92, December 2010.

[6] W. Andrejewski, “Die Beugung Elektromagnetischen Wellen an der Leitende Kreissheibe und an Der Kreisformigne ÌˆOffnung im Leitenden Ebenen Schirm,” Z. Angew. Phys., vol. 5, 1950.

[7] D. A. Hill, M. T. Ma, A. R. Ondrejka, B. Riddle, M. L. Crawford, and R. T. Jonk, “Aperture Excitation of Electrically Large Lossy Cavities,” *IEEE Trans. Electromagnetic Compatibility*, vol. 36, issue 3, pp. 169–179, 1994.

[8] I. Junqua and F. Issac, “Expérimentations sur RAFALE—Rapport d’essais,” Technical Report ONERA RT 1/08212 DEMR, Sept. 2003.

[9] D. Parsons, *The Mobile Radio Propagation Channel*, pp. 35 to 45, Pentech Press, London 1992.

[10] M. Nakhkash, Y. Huang, and M. T. C. Fang, “Application of the Multi-Level Single Linkage Method to One-Dimensional EM Inverse Scattering,” *IEEE Trans. Ant. and Prop,* p. 22, July 2003.

[11] F. Weinmann, “UTD Shooting-and-Bouncing Extension to a PO/PTD Ray Tracing Algorithm,” *Applied Computational Electromagnetic Society (ACES) Journal*, vol. 24, no. 3, pp. 281 – 293, June 2009.

[12] S. Liao, *Microwave Devices and Circuits*, 2nd Edition, pp. 161-162, Prentice Hall, 1980.

Prospective Method for Partial Discharge Detection in Large AC Machines using Magnetic Sensors in Low Electric Field Zones

S. Savin [1,2], S. Ait-Amar [1,2], D. Roger [1,2], and G. Vélu [1,2]

[1] Université Lille Nord de France, F59000 Lille, France

[2] UArtois, LSEE, Faculté des Sciences Appliquées, Technoparc Futura F62400 Béthune, France
sonia.aitamar@univ-artois.fr, serghei_savin@ens.univ-artois.fr, daniel.roger@univ-artois.fr,
gabriel.velu@univ-artois.fr

Abstract **─** The aim of the paper is to present a prospective method for on-line monitoring of partial discharge (PD) in large AC motors. The principle of this system consists to measure the weak high frequency magnetic field, due to PD, in the space between the magnetic core and the external frame of large generators. Special sensor, with a bandwidth adapted to the resonance frequencies of the machine winding, can perform such weak-field measurements. With several sensors, it will be possible to localize PD activities corresponding to insulation weaknesses.

Index Terms **─** Large machine insulation aging, magnetic field sensor, partial discharge monitoring.

I. INTRODUCTION

The insulation systems of large machines which operate at high voltages are made of composite insulating materials that support partial discharges (PD) [1]. These materials are stable over time when the number of PD and their corresponding energy remain within reasonable limits. Many monitoring systems evaluate the overall PD activity for the whole machine insulation system taking information in the machine terminals or connection bars with coupling capacitors or Rogowski coils [2-5]. Other systems use microwave technologies by inserting directional antennas in stator slots; these Stator-Slot-Couplers (SSC) identify whether the PD is originating in the end-winding or in the slot [6-7]. A third family of monitoring systems is based on the detection of mechanical waves (noise specific to PD) [6]. All of these techniques are complementary, they give interesting information on the machine aging; however, the maintenance decisions are still difficult to make. The monitoring of large and expensive machines remains a problem.

The paper proposes a new monitoring method which consists of measuring the low level high frequency magnetic field, created by PD activity, in the cooling gap between the laminated magnetic core and the machine frame.

After a description of the scientific and technological background, a paragraph is devoted to electromagnetic phenomenon in the laminated magnetic core of the machine. It explains how the high-frequency electromagnetic signal is transmitted from the stator bars, in slots, to the free space between the machine laminated core and the frame. Thereafter, the paper is devoted to the experimental demonstration of the ability to implement the new approach on a large machine. The experimental device is built around the stator of the 125MW generator available for research works at the LSEE. Two stator bars are replaced by an experimental line, of similar size, on which a favorable zone to the onset of partial discharges is fitted. A high-frequency equivalent model of the line confirms that the measured signals in the cooling gap circuit are representative of partial discharges created in the stator bar.

Submitted On: May 27, 2011
Accepted On: December 15, 2011

II. SCIENTIFIC AND TECHNOLIGICAL BACKGROUND

The design of large machines has evolved considerably in recent years with the development of simulation tools [7-11]. Their insulation system is made of mineral insulating materials impregnated with resins based on polymers [12]. This technology has proven its reliability despite the inevitable gas vacuoles which remain within the insulation system. When the electric field in a vacuole exceeds a certain threshold, the gas is ionized by a fast electronic avalanche effect; it is the beginning of the partial discharge [13]. Then, the movement of ions and electrons in the gas causes an accumulation of charges on the insulating walls of the vacuole. The direction of motion of the charges is imposed by the electric field vector and the charge accumulation creates an opposite field which shut down the discharge after a few hundred nanoseconds. The electronic avalanche creates a very fast transient in the electrical circuit near the vacuole; the duration of the second phase depends on the response of this external circuit. For a large machine, the external electric circuit corresponds to parallel stator copper bars which form a transmission line for the PD pulse, and the response of such a line creates electromagnetic emissions which can be detected.

For dc voltages, the polarity of the fields and charges does not change, when the internal surfaces of all the vacuoles are charged the PD activity stops naturally. For alternaitve voltages, the charge polarity of the internal walls of each vacuole is reversed at each half-period and the PD global activity does not stops [14].

During each partial discharge the internal surfaces of vacuoles are bombarded by ions and electrons. High energy photons are also emitted. This activity degrades the molecular chains of the polymer while the mineral crystals are more resistant. Therefore, partial discharges cause an erosion of the composite insulation system and tend to increase the volume of vacuoles. The number of partial discharges and the charge quantity displaced tend to increase during the aging of the composite insulation system. These processes are well known, they are at the basis of many monitoring systems of aging of electrical insulation of large machines [1]. Indeed, for a vacuole, the number of partial discharges per period of the voltage and the charge of each of them are two parameters characterizing the vacuole. When these two parameters remain constant over the years, the vacuole is stable. It is obviously impossible to consider separately each vacuole, however, a statistical treatment of the number of PD and their average charge is a good indication of the aging of the whole composite electrical insulation system.

III. HIGH FREQUENCY BEHAVIOR OF LAMINATED CORE

The fast transient phenomena in the windings caused by partial discharges correspond to the upper frequency part of the spectrum, beyond 1MHz. At these frequencies, the eddy currents in the magnetic sheets of the laminated core have a major influence. These currents flow in a very thin layer under the surfaces of each magnetic sheet as shown on Fig. 1, which represents the cross section of the external part of 3 stator sheets.

The eddy current lines, flowing from a side to the other of each magnetic sheet, produce the magnetic field in the cooling gap between the magnetic core and the frame. These current lines are created by high frequency currents in the stator bars, therefore the eddy-current loops act as transmission belts for the information coming from the HF current component in the stator bars.

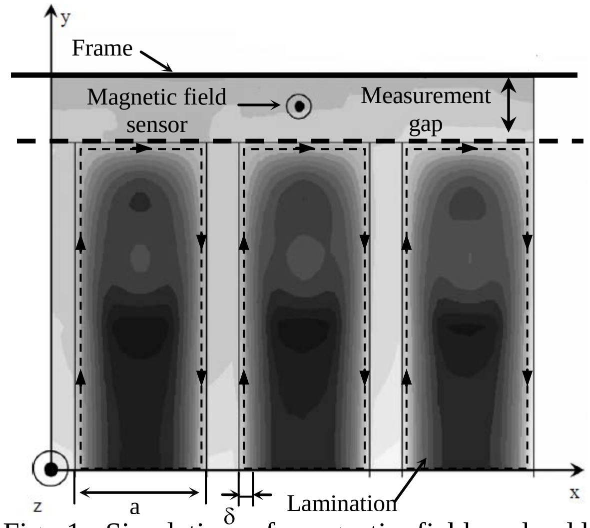

Fig. 1. Simulation of magnetic field and eddy current for large skin depth δ.

Previous studies have demonstrated that, for a skin depth δ much lower than the sheet thickness *a* (δ<*a/40*), the laminated core can ne considered as transparent for HF phenomena in stator slots [15-

16]. Therefore, when a partial discharge occurs in the isolation between bars, it is possible to detect the resulting fast transient current pulse and quantify the charge by measuring the magnetic field in the cooling gap between the laminated core and the machine frame.

When a partial discharge occurs between two stator bars, a HF current *i* flows in the two bars in opposite directions. The corresponding flux density in the cooling gap can be determined with the Ampere's Law, considering the transparency of the laminated core for such HF phenomena. The magnetic field H consists of two components due to the current in each conductor as describes in Fig. 2 where distances d and e are defined. The resulting magnetic field is weak but it can be estimated by:

$$H = \frac{i}{2\pi(d+e)} - \frac{i}{2\pi d} \ , \qquad (1)$$

where *H* is the magnetic field (A/m), *i* is the partial discharge current (A), *e* is the distance between the conductors (m) and *d* the distance between a conductor and the magnetic field sensor (m).

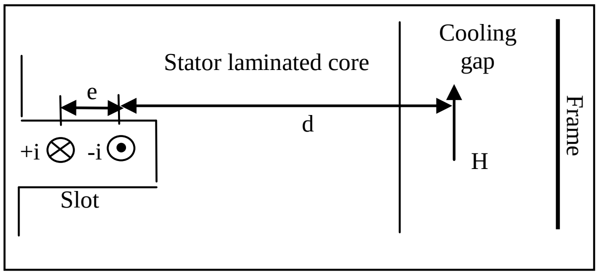

Fig. 2. Magnetic field due to PD between two stator bars.

IV. EXPERIMENTAL VALIDATION

A. Experimental setup

Feasibility of the new PD detection method is tested in the stator of a 125 MW machine (Fig. 3). The stator length is 6.5 m. This machine is used for research, the rotor is removed. A portion of the frame is cut in order to have an access window on the cooling gap, where the magnetic probe is installed.

The stator winding is not powered and two 5 m length cables simulating the HF behavior of stator bars are used. Both cables are spaced at a fixed distance of 2 cm. At the line end, a normalized twisted pair is added to forms a weak point for PD initiation. Once created in the twisted pair, the partial discharge pulse will propagate in the line as it does in the stator bars of a working machine.

To demonstrate the HF behavior of laminated core, the testing protocol is conducted in two parts.

The first measurements are performed outside the stator. The magnetic field probe is placed above the cables, at a distance equal to the width of the stator laminated core (d=65 cm). The position along the cable (1.5 m from the twisted pair) is chosen to coincide with the measurement position of the probe in the free space between the external frame and the stator laminated core (Fig. 4).

The second step of tests consists to put the line and the twisted pair inside the stator (Fig. 3). In this case the magnetic probe is placed in the cooling gap using the window made in the frame.

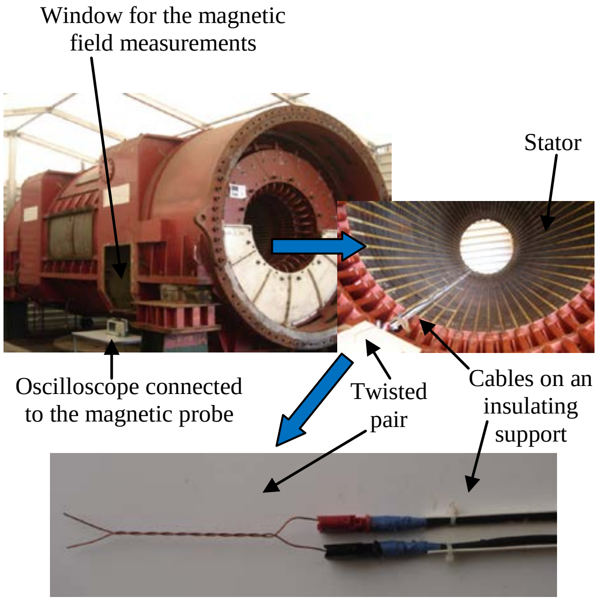

Fig. 3. An instrumented 125 MW stator available in LSEE.

To validate the proposed method of PD detection by magnetic field measurement, it is imperative to perform at the same time another conventional method. However, previous tests allowed the identification of partial discharge attendance by voltage measurements [17-18]. Therefore, voltage measurement corresponding to the propagation of the PD pulse along the cable (Fig. 4) is opted for this test. This signal goes through a high-pass filter (fc=100 kHz), eliminating 50 Hz component. The oscilloscope synchronized on the PD voltage records the voltage and the signal of the magnetic sensor.

The experimental arrangement is illustrated on Fig. 4. The AC voltage supply is placed at the input side of the cables. It includes a low-pass filter with a capacitor (5nF) considered as a low impedance voltage source for the high frequency phenomena in the line.

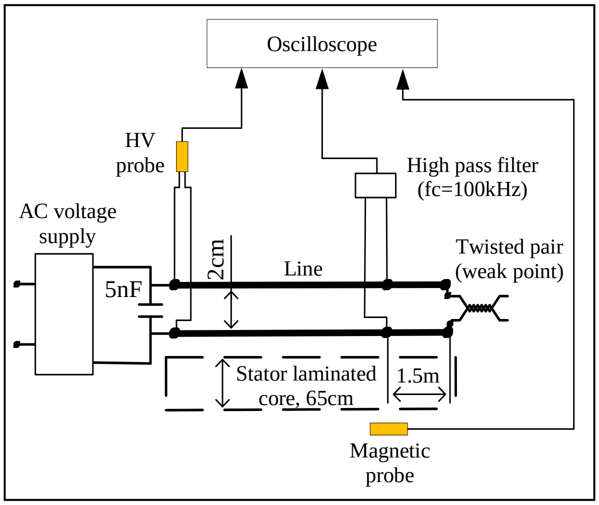

Fig. 4. Experimental system.

In order to initiate partial discharge in the circuit, the applied voltage must exceed the partial discharge inception voltage (PDIV) of the twisted pair (the weak point). This value has been measured with the twisted pair alone. Figure 5 illustrates the measurement of PDIV (> 700 V - 50 Hz) and its corresponding impulse current. There is a succession of short current pulses (mA, ns), which is a classical form of PD attendance [3, 13-14].

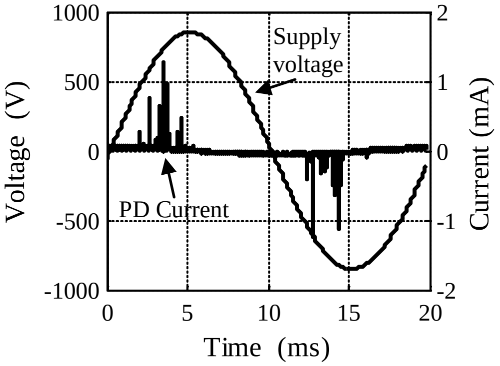

Fig. 5. Partial discharge current (AC-50 Hz).

For the field measurement in the second step of tests, the probe is placed in the cooling gap, between the external face of the stator laminated core and the frame. So the sensor is installed at 65 cm from the cables, which corresponds to the thickness of the stator laminated core.

The detection of such a low level flux density is difficult but not impossible when the sensor is suited to the problem. The sensor is a 4 turns flat coil printed on a PCB, its cross section of 22,5 cm^2. According to Faraday's law, the induced voltage measured by the coil is determined by the time derivative of the flux density. For this application, the induced voltages are in the range of millivolts; therefore amplification is necessary. The global amplification (G=100) is obtained using two low noise amplifiers AD8099. The bandwidth is 550 MHz, so the differences in pulse shape in the nanosecond range are measurable. The PD probe is connected to the oscilloscope via 50 Ω adapted coaxial cables.

B. Experimental results and interpretation

According to the testing protocol previously described, the first measurement is performed outside the stator. The propagation of partial discharge is verified. Figure 6 shows voltage measurement on the cable, in response to a PD pulse.

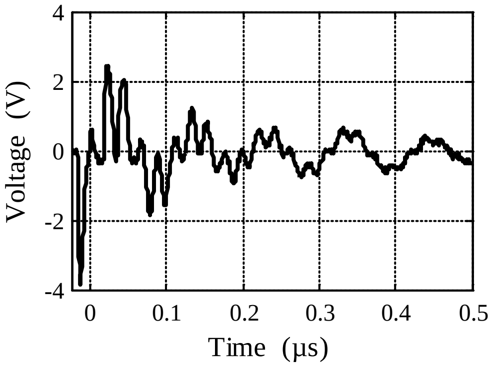

Fig. 6. Voltage pulse measurement on the cable.

The partial discharge is also detected by the magnetic sensor. The induced voltage measured by the probe is used to calculate the magnetic flux density from Faraday's law, by taking into account the amplifier gain (G=100). Figure 7 illustrates the flux density corresponding to the partial discharge.

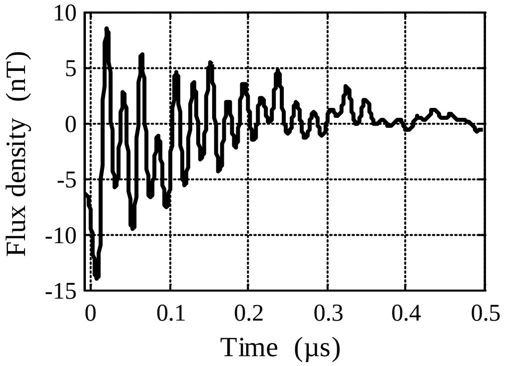

Fig. 7. Flux density due to the partial discharge measured outside the electrical machine.

Note on Fig. 6, that partial discharges (PD) excite resonances found also on the magnetic measurement (Fig. 7). Thereafter, the same measurements are performed by introducing experimental setup (line and twisted pair) inside the stator. The measurement of PD voltage pulse on the line is given on Fig. 8 and the corresponding magnetic field, measured in the cooling gap, is presented in Fig. 9.

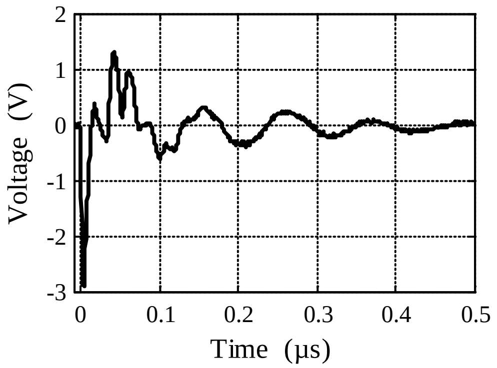

Fig. 8. Voltage measurement inside the stator.

From magnetic field measurements, it can be seen that the magnitude of the flux densities are the same range (Figs. 7 and 9). These results show that the stator laminated core is almost transparent for transient caused by partial discharge in the line equivalent to stator bars. Let us note that the damping is not the same. That can be interpreted by the induced currents in the stator bars, which are made of massive copper. The two measurements are made in the same experimental conditions, PD activity is similar but considering the stochastic nature of PD, it is impossible to have exactly the same PD pulse.

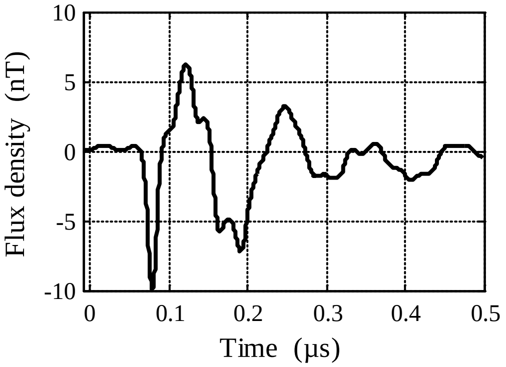

Fig. 9. Flux density due to the partial discharge measured in the cooling gap between the stator core and the frame.

From the measured flux density, the PD current can be estimated, considering a transparent core. This allows calculating the current as done before, considering air between the measurement point and the cable. It is shown in the figure below.

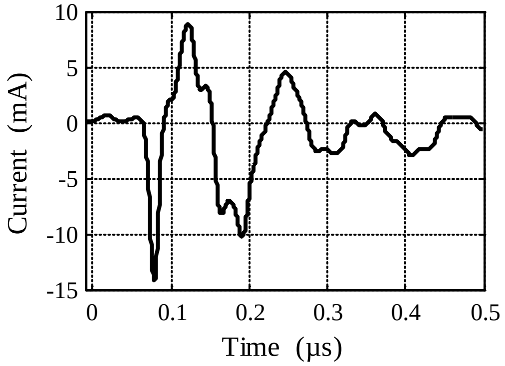

Fig. 10. Partial discharge current in the cable.

V. RESULTS INTERPRETATION WITH A SIMULATION TOOL

The interpretation of the measurement can be detailed using a model of the line simulated by PSpice. The equivalent circuit of the line is connected, at one side, to a current generator which simulate the partial discharge and, at the other side, to the real circuit of capacitor of the power supply filter.

The equivalent circuit of the cable is composed of five sections; their length is much shorter than the wave length at the considered frequency. The parameters of each section are determined using classical analytic formulae of capacitance and inductance and verified by measurement on a cable sample. The resistances corresponding to losses are also obtained using an impedance analyzer.

The voltage source is modeled by the equivalent circuits of the output filter capacitor (5 nF), which parameters are measured with impedance analyzer. The PD is assumed to be a square current pulse with duration of 1 ns and amplitude of 10 mA, so a charge of 10 pC.

Firstly, the Pspice model is used for frequency analysis (Fig. 11). This allows finding the first resonance frequency at 10 MHz which correspond to the oscillations frequencies observed on the measurement results (Figs. 6-10).

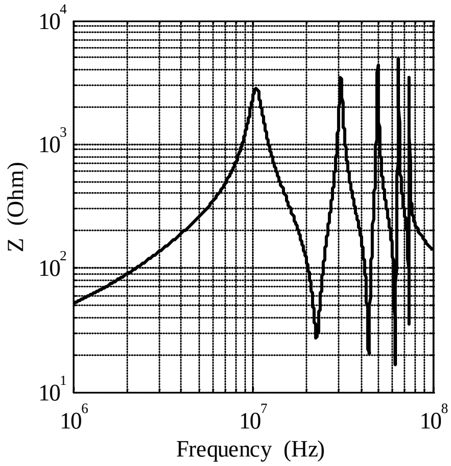

Fig. 11. Frequency analysis of the equivalent impedance of the cable.

Secondly, PSpice model is used to display the current and voltage in different point of the equivalent circuit.

Figure 12 illustrates the PD current calculated at the same point on the cable as in measurements (Fig. 10). It shows a correlation between the results in terms of resonance frequencies and the duration of the following transient state. Since it is difficult to reproduce the same partial discharge pulse during tests, the current amplitudes on Figs. 10 and 12 are different.

These simulation results confirm that the measured field is characteristic of the transient response of the equivalent line excited by a partial discharge current pulse.

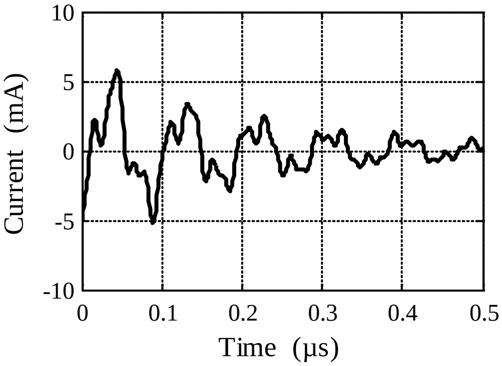

Fig. 12. PD current calculated from the equivalent model.

VI. CONCLUSION

This paper presents a prospective method for partial discharge detection in large ac machine. It shows that it is possible to measure and localize partial discharges in the stator bars by introducing a specific magnetic sensor in the cooling gap between the magnetic core and the machine frame.

The design of the sensor must be performed knowing the main resonance frequency of the stator bars, which depends on the geometry of the copper bars and the permittivity of the insulation between bars.

To be effective the low noise amplifier must be located near the sensor, therefore in the cooling gap. This circuit can monitor continuously PD, with a minimum amount of electronic components, which implicates very low space consumption.

With the proposed method, as it is possible to evaluate the partial discharge current, it will be possible to find a good quantification of the PD charge. This can help to evaluate the critical limits of degradation bars insulation.

Finally, it would be interesting to place more sensors around the stator in the cooling gap. This will allow greater efficiency of this PD detection method. These sensors must be small, cheap and autonomous. Due to the advances in analog electronics and wireless transmission systems, it is possible to develop energy self-sufficient sensors, powered by the leakage flux at the network frequency, on condition to transmit information for short times and at defined period.

ACKNOWLEDGMENT

The authors are grateful and would like to thank Emmanuel MATEO for building the high performance of the sensor at the Laboratoire Systèmes Electrotechniques et Environnement (LSEE). The authors would like to thank EDF, MEDEE, the Nord-Pas de Calais Region, the Ministère de l'Enseignement Supérieur et de la Recherche and the European Regional Development Fund (FEDER), which make available the 125 MW generator for research at LSEE.

REFERENCES

[1] G. C. Stone, E. A. Boulter, I. Culbert, and H. Dhirani, *Electrical Insulation for Rotating Machines - Design, Evaluation, Aging, Testing and Repair*. John Wiley and Sons-IEEE Press, 2004.

[2] IEC 60270, "High-Voltage Test Techniques. Partial Discharge Measurements," ed, 2001.

[3] G. C. Stone, "Advancements During the Past Quarter Century in On-line Monitoring of Motor and Generator Winding Insulation," *IEEE Trans. on Dielec. and Electr. Insul.*, vol. 9, pp. 746-751, 2002.

[4] R. M. Tallam, S. B. Lee, G. C. Stone, G. B. Kliman, J. Yoo, T. G. Habetler, and R. G. Harley, "A Survey of Methods for Detection of Stator Related Faults in Induction Machines," *IEEE Trans. on Indus. Applic.*, vol. 43, pp. 920-933, 2007.

[5] M. Belec, C. Hudon, C. Guddemi, and D. N. Nguyen, "A Case Study of Condition Based Maintenance of a 202-MVA Hydro-Generator," *Int. Conf. Condit. Monit. and Diagn.*, Beijing, China, pp. 163-166, Apr. 2008.

[6] J. K. Nelson and S. Azizi-Ghannad, "Measures and Technologies to Enhance the Insulation Condition Monitoring of Large Electrical Machines," *IEEE Trans. on Dielec. and Electr. Insul.*, vol. 11, pp. 102-112, 2004.

[7] J. Pavo, "Optimisation of the Shape of the Ferromagnetic Core of Fluxset Type Magnetic Field Sensors," *Applied Computational Electromagnetic Society (ACES) Journal*, vol. 12, no. 2, pp. 32-37, 1997.

[8] V. C. Silva and A. Foggia, "A 3d Finite-Element Computation of Stator End-Winding Leakage Inductance and Forces at Steady State Operating Conditions in Large Hydrogenerators," *Applied Computational Electromagnetic Society (ACES) Journal*, vol. 12, no. 2, pp. 90-96, 1997.

[9] J. H. Alwash and L. J. Qaseer, "Three-Dimension Finite Element Analysis of a Helical Motion Induction Motor," *Applied Computational Electromagnetic Society (ACES) Journal*, vol. 25, no. 8, pp. 703-712, 2010.

[10] E. Afjei and H. Torkaman, "Finite Element Analysis of SRG Under Fault Condition Oriented Towards Diagnosis of Eccentricity Fault," *Applied Computational Electromagnetic Society (ACES) Journal*, vol. 26, no. 1, pp. 8-16, 2011.

[11] O. A. Mohammed, S. Ganu, N. Abed, S. Liu, and Z. Liu, "High Frequency Phase Variable Model of Electric Machines from Electromagnetic Field Computation," *Applied Computational Electromagnetic Society (ACES) Journal*, vol. 22, no. 1, pp. 164-171, 2007.

[12] IEC/TS 60034-18-42, "Rotating Electrical Machines. Part 18-42: Qualification and Acceptance Tests for Partial Discharge Resistant Electrical Insulation Systems (Type II) used in Rotating Electrical Machines Fed from Voltage Converters," ed, 2008.

[13] R. Bartnikas, "Partial Discharges. Their Mechanism, Detection and Measurement," *IEEE Trans. on Dielec. and Electr. Insul.*, vol. 9, pp. 763-808, 2002.

[14] C. Kwan, *Dielectric Phenomena in Solids*, Elsevier Academic Press ed., 2004.

[15] S. Duchesne, E. Napieralska-Juszczak, and D. Roger, "Eddy Current Influence on Electromagnetic Emissions of Laminated Cores," *COMPEL*, vol. 26, pp. 986-1004, 2007.

[16] S. Duchesne, E. Napieralska-Juszczak, and D. Roger, "Eddy Current Influence on Electromagnetic Emissions of Laminated Cores," *COMPEL*, vol. 26, Issue 4, pp. 986-1004, 2007.

[17] S. Savin, S. Ait-Amar, D. Roger, and G. Vélu, "Aging Effects on the AC Motor Windings: A Correlation Between the Variation of Turn-to-Turn Capacitance and the PDIV," *2011 IEEE CEIDP*, Cancun, Mexico, pp. 64-67, October 2011.

[18]S. Ait-Amar and D. Roger, "Prospective Method for Partial Discharge Detection in Large AC Machines using Magnetic Sensors in Low Electric Field Zones," *IET 8th Intern. Conf. on Comput. in Electromagn. (CEM 2011)* Wroclaw, Poland, pp. 70-71, April 2011.

Serghei Savin was born in Orhei, Moldova in 1985. He received the M.S. degree in Electrical Engineering at Technical University of Moldova in 2009. He is now a Ph.D. student at Artois University in France. His research interests are in partial discharge detection and insulation system of electrical machines.

Sonia Ait-Amar was born in 1971. She received the diploma of Electrical Engineering and Doctor in Electrical Engineering from the University of Bejaia in 1994 and 1997, respectively. Thereafter, she taught at the University of Bejaia and pursued her research in electrical discharges. In 2003, she joined ABB France as a researcher. She received the Ph.D. degree in Plasma Physics from Paris Sud 11 University in 2006. She is Associate Professor at the University of Artois since September 2008. Her research interests are insulation aging of electrical machines and the development of new methods of predictive maintenance based on partial discharges monitoring.

Daniel Roger was born in Bouvines, France, in 1955. After a 2-year industrial experience in electronics, he was engaged as a teacher in a technical school. He obtained the French Agregation in 1989, the Ph.D. degree in Electrical Engineering at the University of Lille in 1993 and a D.Sc. degree in 2003 at the University of Artois. Since 2004, he is Professor at the University of Artois where he teaches electromagnetism and power electronics. His research interests, within the Laboratoire Systèmes Electrotechniques et Environnement (LSEE), are electromagnetic emissions of electrical systems, design and diagnosis of electrical machines and their electrical insulation system.

Gabriel Vélu was born in Béthune, France in 1969. He received the Ph.D. degree in Génie des Procédés from the Université de Valenciennes et du Hainaut Cambrésis, France, in 1998. He was joining the Université du Littoral-Côte d’Opale, France in 1999. He was a member of the Laboratoire d’Etudes des Matériaux et des Composants pour L’Electronique. His research interests included ferroelectrics thin films depositions and their tunable applications in microwave field. Since 2011, he is Professor at the Laboratory LSSE at the University of Artois, France, where he is developing a new concept of electrical machine for high temperature and high power density.

Evaluation of High Frequency Electromagnetic Behavior of Planar Inductor Designs for Resonant Circuits in Switching Power Converters

A. Nejadpak, M. R. Barzegaran, and O. A. Mohammed

Energy Systems Research Laboratory, Department of Electrical and computer Engineering
Florida International University, Miami, FL, 33174, USA
mohammed@fiu.edu

Abstract **—** In this paper, a planar inductor based resonant circuit is designed for zero-current switching (ZCS) buck converter. In order to evaluate the actual behavior of the converter at the design stage, a numerical model of the inductor was created and implemented using the finite element (FE) analysis. Using the numerical model, a high frequency physics based circuit model was obtained for the converter's resonant circuit. The acquired physics based circuit model was used to approximate the electrical behavior of the resonant circuit. The operating condition of the half-wave ZCS buck converter was verified both numerically and experimentally. It was shown that by using the proposed high frequency model, it is possible to evaluate realistic waveforms of voltages and currents including the effects of parasitic elements. This is an essential step for studying conducted electromagnetic field emissions in power converters for the evaluation of their EMI interactions for EMC compliant designs.

Index Terms **—** EMI, EMC, finite element analysis, high frequency modeling, planar inductor, quasi-resonant converters.

I. INTRODUCTION

Soft-switching converters are becoming more popular as they have lower loss and noise characteristics as compared to pulse width modulation (PWM) converters. In these types of converters, the resonance circuit is a major contributor to the creation of EMI. It can cause unexpected current noise flow in the common mode path [1].

Generally, in order to control the conducted emissions (CE) noise in the soft-switching converters, the issue of parasitic elements must be considered during the design stage. These parasitics are circuit elements (resistance, inductance, or capacitance) that are possessed by electrical components, but are not desirable for them to have it.

So far, various algorithms were introduced to eliminate or minimize the effects of these unwanted elements [2-4]. Previously, methods based on the parallel-plate waveguide and FEM analysis was introduced to solve the PCB unwanted coupling problems and reduce the EMI effects of the converters [5-8].

All components and interconnections contain unintentional (parasitic) circuit elements which often a combination of them can make a change in the operating condition of the whole power converter. This makes the EMI issues more complicated. Furthermore, the switching action causes various parasitic elements in the converter and result in conducted and radiated energy at unpredictable frequencies. In practice, these parasitic oscillation frequencies are most difficult to filter out. They often cause the most interference with signal processing circuitry.

Therefore, an understanding of the magnitude of these parasitic elements and the characteristics of the components over a range of frequencies will ensure the correct choice of their application. Also, it is important for investigation of the effects of switching-frequency control on EMI generation.

The operating principle of the Quasi-resonant converters is described in [9]. These converters are

Submitted On: June 9, 2011
Accepted On: September 25, 2011

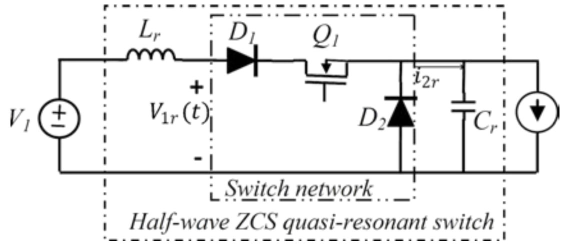

Fig. 1. Half wave zero current switching buck converter's circuit model.

obtained by adding the resonant elements L_r and c_r to the PWM switching converters. Figure 1 shows the simplified circuit model for ZCS-Buck converter. The parasitic elements in the configuration of the resonant components can affect the operating condition of the whole converter. In order to have a more precise study on the converter behavior, a distributed model should be obtained for each of the elements.

In this paper, a planar inductor based resonant circuit is designed for the converter's resonant inductor (shown by L_r in Fig. 1). This design can meet the packaging constraints in power electronic converters in addition to the required EMI compliance levels. Design and characteristic optimization of the planar inductor is studied in references [10-13]. The electromagnetic radiation of a PCB planar inductor is discussed in [14, 15]. As an example, based on the procedure in reference [9], the inductance value is selected to be $L_r = 1\mu\text{H}$, and the resonant capacitor is selected to be $C_r = 400nf$. With this selection, the resonant frequency will be $f_0 = \frac{1}{2\pi\sqrt{L_r C_r}} = 251.65\ \text{kHz}$.

Subsequently, in order to find the parameters of the converter, a finite element analysis is performed on the resonant part of the converter. After obtaining the high frequency physics based model of the resonant circuit, the resonant behavior of the proposed planar inductor based resonant circuit is compared with the ideal resonant circuit. The FE analysis is used to study the electromagnetic behavior of the proposed resonant circuits in Section II of this paper. As a result, a high frequency model is obtained for the resonant circuit under a wide range of switching frequencies. Finally, the resonant circuit design was optimized in order to compensate the destructive effects of parasitic elements in the operation of the converter. The results were verified through simulations and experimentation.

II. DISTRIBUTED-PARAMETER FREQUENCY DEPENDENT MODELING

Under PWM operating conditions, the inductor's resistance, inductance, and capacitance behave differently from the low frequency operation. The windings have skin and proximity effects, which cause the resistance to be much higher than the low frequency value. The inductance value decreases with the increase in the operating frequency, while the small capacitance effect comes in the picture at high frequencies. Under such PWM operation, the inductor winding's capacitance is distributed between several parts of the winding (turn to turn and turn to ground). Hence, to obtain accurate values of the resistances, inductances (self and mutual), and capacitances (self and mutual), a detailed numerical model for the inductor should be used. Also, this strategy is used for the capacitor of the converter since, in higher frequencies, the self and mutual inductances as well as the self and mutual capacitances have effects in the frequency response analysis.

In reference [16], a method based on the vector fitting algorithm was proposed for modeling the physics-based representation of transformers. This is also applicable to the inductor design. The method used in this study is based on the lumped-parameter model presented in [17, 18]. This method is used to obtain the s-domain model of a spiral winding planar inductor, which can be used to find the frequency response of the inductor. The proposed model includes the windings' resistances, self inductances, ground capacitances, the inter-turn capacitances within each winding and the mutual inductive and capacitive couplings between the two windings.

A. Physics based modeling using FEM

A three dimensional finite element study was performed on the resonant circuit components, in order to calculate the parasitic elements of these components, which can affect the operating condition of the converter.

The electromagnetic field inside the inductor and capacitor is governed by the following set of nonlinear partial differential equations [17]:

$$\vec{\nabla} \times \left((v) \vec{\nabla} \times \vec{A} \right) = \vec{J}, \qquad (1)$$

$$\nabla . \sigma \left(\frac{\partial \vec{A}}{\partial t} + \nabla V \right) = 0, \qquad (2)$$

where $\vec{A}$ is the magnetic vector potential, $\vec{J}$ is the total current density, v is the magnetic reluctivity, V is the electric scalar potential, and σ is the electric conductivity. By solving these equations, the resistance and inductance of the inductor are calculated as a function of frequency.

Also, the electrostatic problem is solved for the calculation of capacitances matrix, as capacitances are a function of geometry rather than frequency. An electrostatic analysis is assumed to be a linear analysis, which means that the electric field is proportional to the applied voltage. The analysis determines the electric scalar potential distribution caused by the applied voltage. The following Maxwell equation is solved during electrostatic analysis.

$$\nabla . (\varepsilon \nabla V) = -\rho, \qquad (3)$$

where ρ is surface charge density, ε is permittivity, V is electric scalar potential. By coupling electric and magnetic analyses, electromagnetic analysis for frequency response analysis based on (6) are applied in this simulation.

Typically, the quasi-static electromagnetic analysis is used as analysis approach in these cases, but this method has one problem. The changing electric displacement field over time is considered as zero (∂D/∂t=0). This assumption can be used for low frequency analysis. However, for higher frequency analysis this assumption affects the result [19, 20]. Therefore, a new approach was used in this research in which ∂D/∂t is considered.

To derive the time harmonic equation, this physics interface solves magnetic and electric interface. The analysis is started with Maxwell-Ampere's law including the displacement current. This does not involve any extra computational cost in the frequency domain. Firstly, a time-harmonic field is assumed as (4).

$$\nabla \times \mathbf{H} = \mathbf{J} = \sigma(\mathbf{E} + v \times \mathbf{B}) + j\omega\mathbf{D} + \mathbf{J}^e. \qquad (4)$$

Using the definitions of the fields $\mathbf{B} = \nabla \times \mathbf{A}$ and $\mathbf{E} = -\nabla V - j\omega\mathbf{A}$ and combine them with the constitutive relationships $\mathbf{B} = \mu_0(\mathbf{H} + \mathbf{M})$ and $\boldsymbol{D} = \varepsilon_0 \mathbf{E}$**,** the Ampere's law can be rewritten as (5).

$$(j\omega\sigma - \omega^2\varepsilon_0)\mathbf{A} + \nabla \times (\mu_0^{-1}\nabla \times \mathbf{A} - \mathbf{M}) - \sigma\boldsymbol{v} \times (\nabla \times \mathbf{A}) + (\sigma + j\omega\varepsilon_0)\nabla V = \mathbf{J}^e. \qquad (5)$$

The equation of continuity is again obtained by taking the divergence of Ampere's law. It is the equation solved for the electric potential. Thus, the following equations for V and **A** are achieved

$$-\nabla . \left((j\omega\sigma - \omega^2\varepsilon_0)\mathbf{A} - \sigma\boldsymbol{v} \times (\nabla \times \mathbf{A}) + (\sigma + j\omega\varepsilon_0)\nabla V - (\mathbf{J}^e + j\omega\mathbf{P}) \right) = 0. \qquad (6)$$

A particular gauge can be obtained with reducing the system of equation by choosing $\Psi = -jV/\omega$ in the gauge transformation. So modified magnetic vector potential is obtained.

$$\tilde{\mathbf{A}} = \mathbf{A} - \frac{j}{\omega}\nabla V. \qquad (7)$$

Working with $\tilde{\mathbf{A}}$ is often the best option when it is possible to specify all source currents as external currents $\mathbf{J}^e$ or as surface currents on boundaries.

$$(j\omega\sigma - \omega^2\varepsilon_0)\tilde{\mathbf{A}} + \nabla \times \left(\mu_0^{-1}\nabla \times \tilde{\mathbf{A}} - \mathbf{M}\right) - \sigma\boldsymbol{v} \times \left(\nabla \times \tilde{\mathbf{A}}\right) + (\sigma + j\omega\varepsilon_0)\nabla V = \mathbf{J}^e + j\omega\mathbf{P}, \qquad (8)$$

where A is magnetic potential, J^e is external current density, M is magnetization, and $\boldsymbol{v}$ is the motion speed which here, it is equal to zero.

The equation (8) is a modified version of a classic quasi-static equation (5), which is implemented in FE softwares [21]. Further modification in this study is applied by linking MATLAB software with FE software. This can be done by defining a variable in MATLAB codes as **D** and making a link to the FE software, then considering this **D** (electric displacement field) instead of the default D. This new defined electric displacement field is based on the electric field obtained from the solution of software. The other element ($\tilde{\mathbf{A}}$) is defined in the same way.

Another necessity of this type of analysis is the need of simultaneous estimation of capacitance and inductance that the former one can be calculated by electrostatic analysis and the latter one by magnetostatic analysis. This type of interface can be used for 3D, 2D in-plane, and 2D axisymmetric models. Note that the magnetic and electric currents physics interface supports the stationary and frequency domain study types better than transient domain study.

Figure 2 shows the planar spiral inductor and capacitor models used in the power converter. To

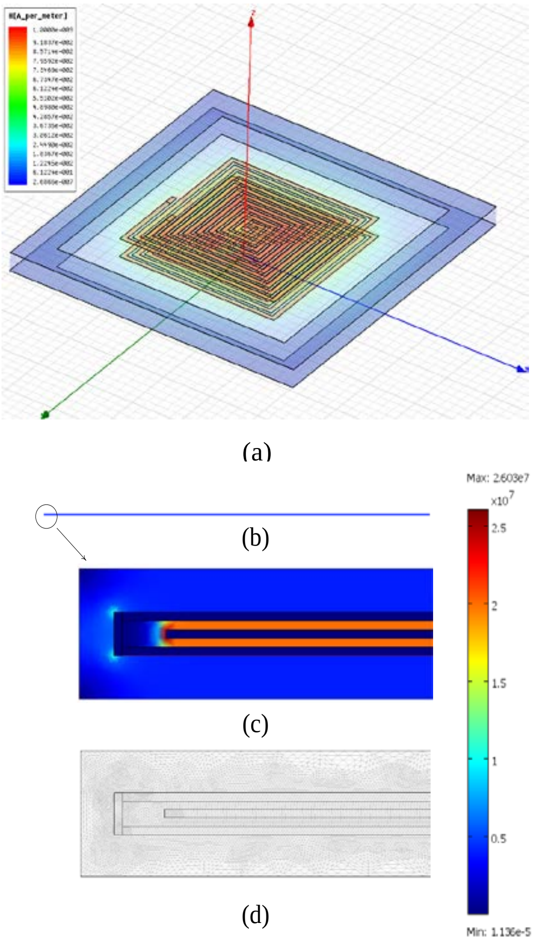

(a)

(b)

(c)

(d)

Fig. 2. Field spectrum from the finite element analysis for the calculation of high frequency model of this component. (a) Magnetic field intensity of spiral planar inductor, (b) capacitor, (c) electric field in small part of the capacitor, (d) mesh in capacitor.

find a numerical solution for this problem, coupling of the FE and a circuit based analysis is utilized. The amount of energy, magnetic and electric field are estimated from the FE model. The results are then imported to the circuit-based software (Spice), in order to evaluate the performance of the whole circuit.

After solving the FE model, the inductance, capacitance, and resistive matrices were obtained via calculation of the energy matrix in the FE model. The magnetic energy is calculated by:

$$W = \frac{1}{2}\oiiint_V \mu \cdot Re(\boldsymbol{H}_1 \cdot \boldsymbol{H}_1^*)\, dv + \frac{1}{2}\oiiint_V \mu \cdot Re(\boldsymbol{H}_2 \cdot \boldsymbol{H}_2^*)\, dv + \frac{1}{2}\oiiint_V \mu \cdot Re(\boldsymbol{H}_1 \cdot \boldsymbol{H}_2^*)\, dv, \quad (9)$$

where $\boldsymbol{H}_i, i = 1{,}2$ is the magnetic field intensity inside the model and μ is the permeability of the model.

Following the calculation of the magnetic energy in the FE model, equation (9), all self and mutual inductances were estimated based on the magnetic energy value, [22, 2]. Also explanation about deriving capacitances and resistances is mentioned in the same references.

B. Numerical discussion

As it was discussed, a numerical technique based on the adaptive MEI-FEM (magnetic-electric interface finite element method) is used. This method has much more accurate result as compared to quasi-static electromagnetic finite element method, electrostatic finite element method, and magnetostatic finite element method. All experiments are performed on a x5677 dual core 3.47 GHz CPU and 192GB RAM. The iteration process is terminated when the normalized backward error (tolerance) is reduced by 10^{-3}.

To implement the MEI-FEM, the adaptive grouping method is used to reduce the memory consumption and captures the fine details of the structure. The simulation time for the analysis of the inductor with five million degrees of freedom and 10^{-3} percent tolerance of energy was 3 hours. Also, simulation time for the analysis of the capacitor with three million degrees of freedom, Fig. 2(d), with $1e^{-7}$ percent tolerance of energy was about 2 hours. Figure 3 shows the energy tolerance versus the number of degrees of freedom.

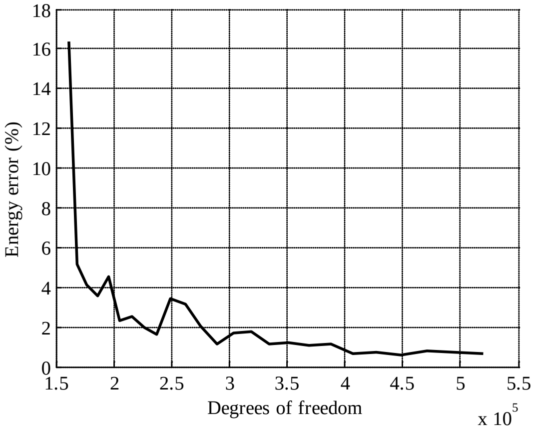

Fig. 3. Energy tolerance versus degrees of freedom.

The analysis method which is used in this analysis is the generalized minimal residual method (usually abbreviated GMRES) with successive over-relaxation (SOR) as pre and post smothers. GMRES is an iterative method for the numerical solution of a system of linear equations [23]. In numerical linear algebra, the method of SOR is a variant of the Gauss–Seidel method for solving a linear system of equations, resulting in faster convergence. A similar method can be used for any slowly converging iterative process. The SOR method uses a more accurate approximation of the matrix, which leads to fewer iterations but slightly more work per iteration than in the Jacobi method.

Since the geometry of the elements are non-uniform (the length of some elements are much bigger than the width of them). Geometric multi-grid method is chosen as the pre-conditioner and F-cycle as multi-grid cycle. Also, the parallel sparse direct linear solver (PARDISO) method with 1e^{-8} pivoting perturbation is chosen as the coarse solver.

C. Development of lumped-parameter model

The influence of the capacitive reactance is increased by increasing the switching frequency. Therefore, very small capacitive reactances can affect the input transfer function in higher frequencies. Besides, mutual inductances between elements at far distances are more significant in the transfer function in high frequencies. So, a model which considers all these reactances is essential. The distributed-section model considers almost all tiny capacitive reactances and mutual inductances, so it is eligible for high frequency analysis.

Following the calculation of all required parameters for the distributed model, these parameters are located in the model, then the model evaluation procedure starts. As in the lumped parameter model, the evaluation procedure from the distributed parameter nature of the problem at hand, we start at a location x and moving an infinitesimal distance Δx toward the lower end of the winding, the potential difference ΔV is calculated as:

$$\begin{bmatrix}\Delta V_1(x,s)\\ \Delta V_2(x,s)\end{bmatrix} = \begin{bmatrix}Z_1(s)\Delta x & Z_m(s)\Delta x\\ Z_m(s)\Delta x & Z_2(s)\Delta x\end{bmatrix}\begin{bmatrix}\hat{I}_1(x,s)\\ \hat{I}_2(x,s)\end{bmatrix}, \qquad (10)$$

where $\hat{I}_1(x,s)$ and $\hat{I}_2(x,s)$ are the current following in Z_1 and Z_2, respectively. The indices 1 and 2, indicates the first and the second layer of the inductor's and capacitor's models. A detailed description of this method is presented in reference [17]. By transferring the modal domain into a phase domain, the voltages of the top terminal in two layers are calculated as:

$$\begin{bmatrix}V_{s1}(s)\\ V_{s2}(s)\end{bmatrix} = \begin{bmatrix}M_{11}(s) & M_{12}(s)\\ M_{21}(s) & M_{22}(s)\end{bmatrix}\begin{bmatrix}I_{s1}(s)\\ I_{s2}(s)\end{bmatrix}, \qquad (11)$$

where $M_{ij}(s)$ are elements of the impedance matrix in s-domain.

To determine the frequency characteristics of the inductor we set $s= j\omega$ in the related equations. The input impedance is given by:

$$Z_{in}(j\omega) = \frac{V_{s1}(j\omega)}{I_{s1}(j\omega)}. \qquad (12)$$

Using the above equations, input impedance on the component is calculated as the following:

$$Z_{in}(j\omega) = M_{11}(j\omega). \qquad (13)$$

The rational function given by (13) can be represented by an equivalent electrical network as shown in Fig. 4. Note that, the circuit model in Fig. 4 is not unique and can be shown in various configurations. This network reflects the frequency dependence of the inductor resistance, inductance and capacitance. Using $Z_{in}(j\omega)$, the natural frequencies are determined.

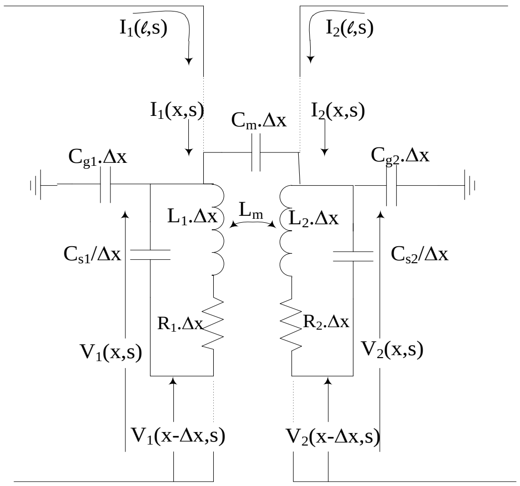

Fig. 4. Infinitesimal section of a two-layer winding of planar inductor.

The distributed model parameters of the designed inductor, from the finite element analysis were; R_1= 0.2713 Ω, R_2=0.2713 Ω, L_1=0.557 µH, L_2=0.557 µH, L_m=0.307 µH, C_{s1}=8 pF, C_{s2}=8 pF, C_{g1}=0.33 pF, C_{g2}=0.33 pF, C_m=6.7 pF. Also, the distributed model parameters of the capacitor were; $R_{c1,2,3}$= 0.006725 Ω, R_{cm}=10 kΩ, $L_{c1,2,3}$=5 pH, $C_{s1,2,3}$= 0.49 pF, $C_{g1,2,3}$=4.42 pF, C_m=177 nF. As mentioned earlier, the indices 1 and 2 of the inductor parameters stand for the first and the second layers of the inductor, as shown in Fig. 2(b). Note that the neutral-end terminal point of the first layer is connected to the line-end terminal of the second layer.

An advantage of the distributed-parameter model is to reveal the high frequency behavior of the model. Therefore, using only simplified modeling of the resonant stage of HW ZCS-Buck converter doesn't show all the resonances and only shows the basic resonance as depicted in Fig. 5(a).

The embedded distributed model which is shown in Fig. 4 should have at least 5 sections to have reasonable result. We considered 10 sections in this study to have better and more accurate results. As mentioned in [17], the result will be more accurate with more number of sections but from specific number of section like 10 the results will not change significantly.

Utilizing the distributed parameter model developed in this paper, as shown in Fig. 5(b), a realistic picture emerges. The number of resonances becomes more practical and representative of the real device than the one given in Fig. 5(a). Accounting for parasitic resonances in higher frequencies will enable a realistic inclusion of EMC issues in the design stage. Through the optimization procedure [24], the size and geometry of the spiral planar inductor is changed in a way to minimize the effects of the parasitic parameters on the operating condition of the converter. The proposed algorithm is summarized as follows:

- Step 1: Design the planar inductor in the FE software.
- Step 2: Calculate the magnetic and electric fields based on equations (4)-(8).
- Step 3: Calculate resistances, inductances and capacitances based on equation (9).
- Step 4: Substituting the obtained parameters into the circuit shown in Fig. 4.

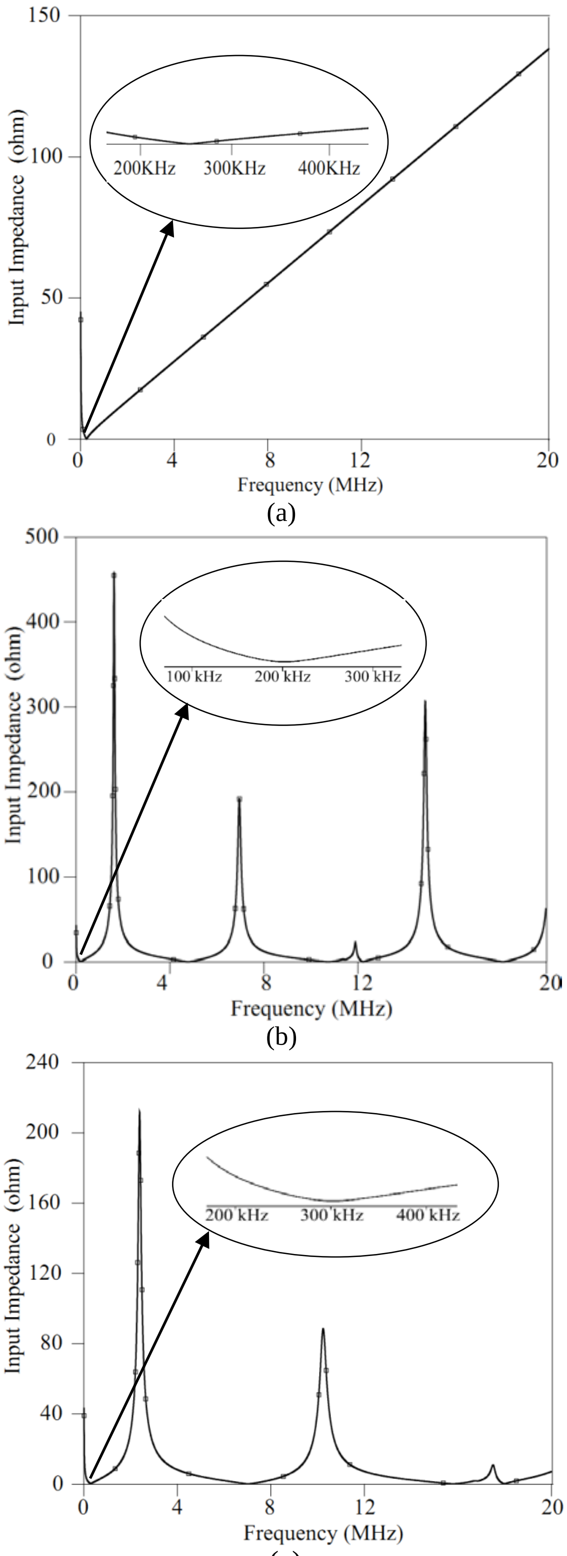

(a)

(b)

(c)

Fig. 5. Frequency response analysis of the ZCS buck converter. (a) Simple model, (b) distributed-parameter frequency model, (c) optimized distributed-parameter frequency model.

III. RESONANT CIRCUIT DESIGN OPTIMIZATION

As shown in Fig. 5, the first resonance frequency in Fig. 5(b) is much lower than the expected resonance frequency (the first resonance frequency shown in Fig. 5(a)). This phenomenon may deteriorate the operation of the converter. Because the resonance part of the converter is designed to resonate in 250 kHz (in this example) but in practice, it's resonating at lower frequencies.

In order to solve this problem, an optimization procedure is utilized in the design of the planar inductor. The main objective in the procedure of the optimization is to set the resonance frequency to the desired value (i.e 250 KHz), while reducing the amplitude of higher order harmonics. To achieve this goal, through the optimization process the planar inductor trace thickness and voltage clearance is changed as well as the number of turns. Therefore, a multi-objective function is formed as a combination of each of these single objectives. The first part of this multi-objective function is calculated from a transient non-linear FE analysis to calculate the value of the inductor. Moreover, the second part of this multi-objective function is calculated from the circuit simulation of the resonant circuit which is implemented in the Pspice environment. A classic genetic algorithm multi-objective optimization scheme is utilized to do the optimization task automatically. The variable of the genetic algorithm are indeed the inductance value of the planar inductor and magnitude of the harmonics in the resonant circuit output.

Figure 6 depicts the flowchart of the parameter optimizing procedure using GA. GA is a population based global search procedure which is inspired by natural selection and genetics law [25]. Parameters for optimization are number of turns in each layer (N) and inductor's trace dimensions. The GA evolves the given population of individuals.

The objective function is as follows:

$$Objective\ function = \alpha_1.|\Delta f|^2+\alpha_2.|Z_{in}(s)|^2$$

where, $\alpha_{1,2}$=Weights signifying the importance of the objective function (taken as 1 in our case), Δf: frequency of the main resonance (resonant circuit first natural frequency) and $Z_{in}(s)$: input impedance of the resonant circuit. The main purpose of GA is to find the minimum for objective function.

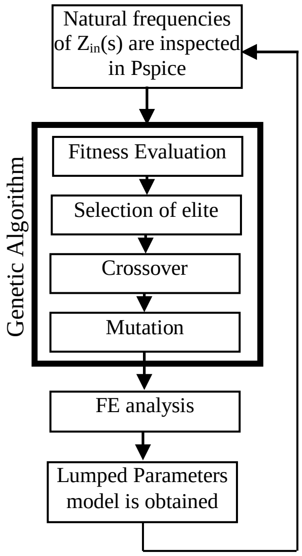

Fig. 6. The optimization process.

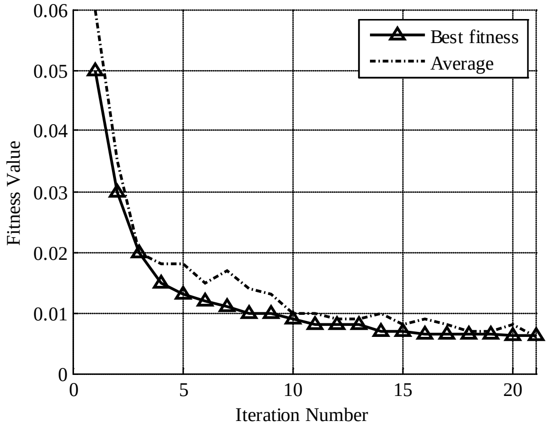

Fig. 7. Iteration accomplished by GA to minimize the objective function.

The fitness function computes the error of the simulated and specified reference signal at each time point. The errors are then squared and added together to give a single scalar objective value.

The fitness values shown in Fig. 7, illustrate that after about 10 number of iteration the error reaches to an acceptable value. Table 1 shows the results of the GA-algorithm and it is compared to the conventional inductors. Note that the optimization procedure is mainly applied on the design of the planar inductor and the resonance capacitor is not considered in the design optimization.

Table 1: Optimal values for designed inductor resulted from GA

Planar inductor design	L (μH)	Trace width (mil)	Number of turns
Un-optimized	1	40	8
Optimized	0.76	29.75	6

Figure 5(c) shows the frequency spectrum of the optimized resonant circuit. In Fig. 5(c), compared to Fig. 5(b), the unwanted higher frequency resonances are reduced. Also, the main resonance frequency is set to its desired value. (i.e. 250 KHz)

IV. RESULTS AND DISCUSSION

Figure 8 shows the experimental setup used to test and verify the results. In this setup, to inspect and record the results, a 600 MHz, 10 Gsample/s oscilloscope was used. The bandwidth for both the voltage and current probes were 100 MHz. The converter should operate in the zero-current switching condition. Therefore, the switching frequency and duty cycle is set by the digital function generator.

Figure 9 shows the effects of high-frequency operating conditions on the zero current switching (ZCS) of the MOSFET in the converter circuit. In this configuration, it was expected to increase the output voltage of the converter by increasing the operating frequency of the MOSFET, while keeping the ZCS sequence as shown in the ideal case (without considering all parasitic elements) shown in Fig. 9(a). The simulation results show that the ZCS behavior of the converter is completely lost as a result of using the high-frequency circuit model for the resonance circuit as shown in Fig. 9(b). The parameters in these circuits were evaluated from the FE implementation described in the previous section.

To keep the desired performance of the converter, the switching frequency of the converter should be kept below the value shown in Fig. 7(b). In an actual case (distributed-parameter frequency model), it can be observed from Fig. 7(b) that the next resonant frequencies, happen at the frequencies starting from 4.5 MHz and above. Figure 10 shows a comparison between two different designs of the resonant circuit. Figure 10(a) shows the FFT analysis of the primary design of the resonant circuit and Fig. 10(b) shows the FFT of the optimized resonant circuit output signal. It is noticed that, by design optimization the number and amplitude of harmonics is reduced.

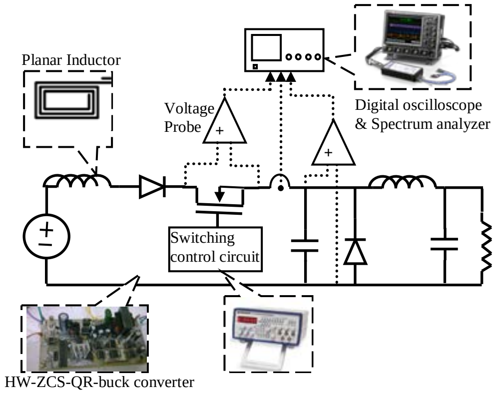

Fig. 8. Schematic of the converter's experimental setup.

To verify the simulation results in Fig. 9, an experimental test was carried out. Figure 11 shows the measured voltage and current of the MOSFET, which is located in series with the resonance inductor (see Fig. 1). As it is illustrated in Fig. 11(a), in the primary design (un-optimized) of the resonance-circuit, by increasing, the switching frequency above a certain value the unwanted resonances will appear. These resonances can harm the proper zero-current switching operation of the converter.

Figure 11(b) shows the switch's voltage and current, in the circuit with the optimized resonance circuit. As it is illustrated in this figure, the converter is operating in zero-current switching condition as it was expected.

In Fig. 11(a), some distortions are observed in the switch's voltage waveform. These distortions are mainly because of the parasitic elements of the circuit and poor layout of the PCB, which are not considered in this study.

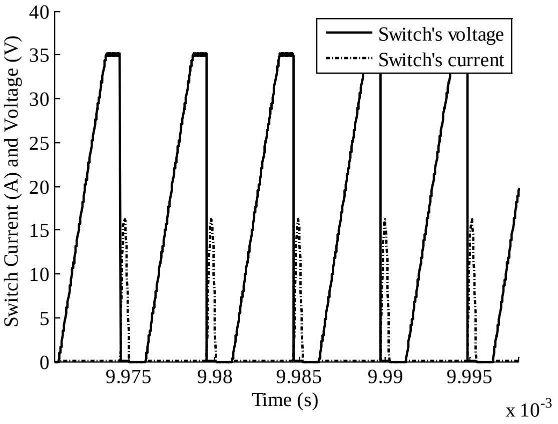

(a)

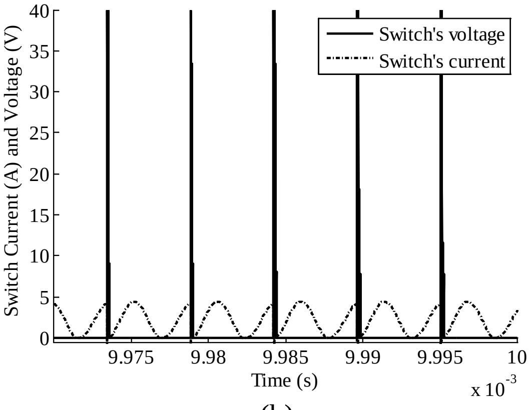

(b)

Fig. 9. Voltage and current of the switches in ZCS-Buck converter, (a) ideal case, (b) actual case.

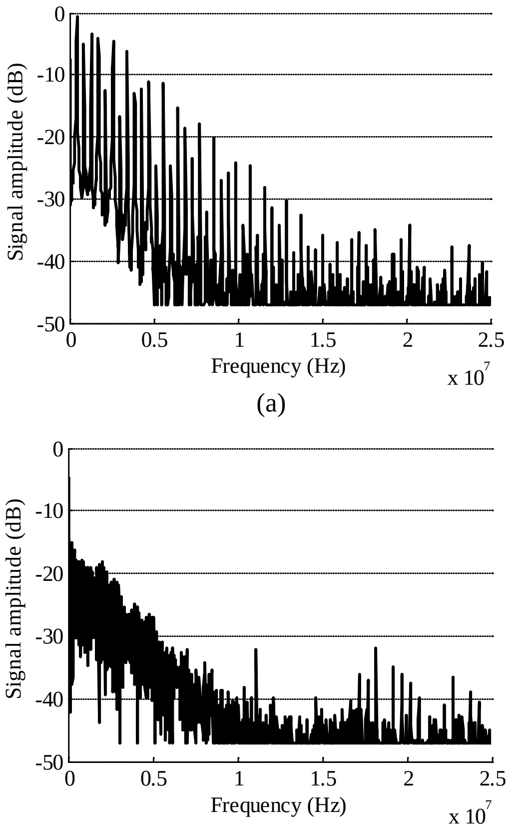

(a)

(b)

Fig. 10. FFT spectrum of the resonant circuit. a)Initial design, b) modified design.

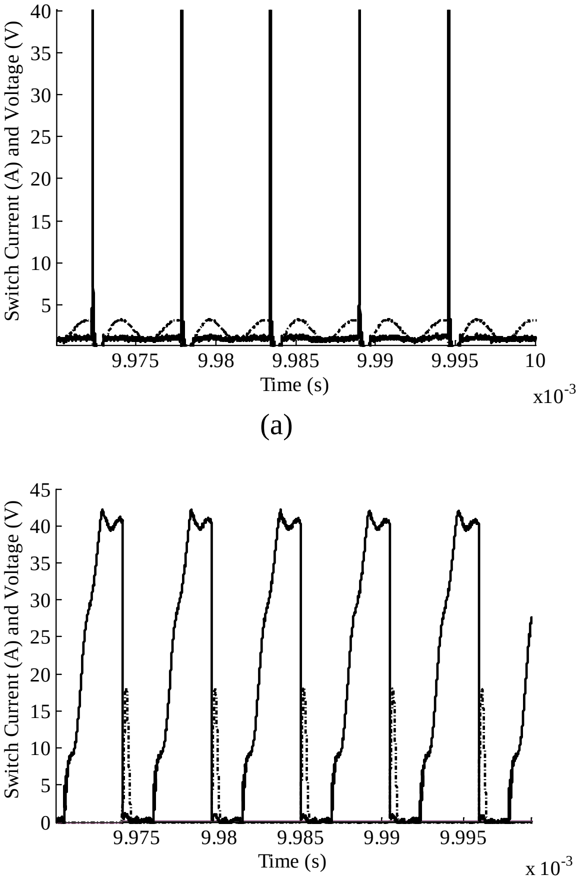

(a)

(b)

Fig. 11. Measured voltage and current of the switches in ZCS-Buck converter, (a) primary designed circuit, (b) optimized circuit.

V. CONCLUSIONS

In this paper, a method for high frequency model of the converter’s components is presented using coupled circuit/electromagnetic FE computations. The FE analysis was performed to obtain the frequency behavioral model of the converter. The natural frequencies computed from the proposed s-domain model, was used to analyze the circuit's electrical behavior and operation. The results show that the s-domain model of the converter has the ability to reveal the behavior of parasitic elements as well as higher resonances which has critical impact in studying EMI problems. This model can also be implemented for other types of converters making it practical for the evaluation on EMI/EMC issues in the design and development stages. The power converter discussed in this paper is not a representative of all power converter designs. But can show the value of considering the effects of parasitic components on operation of the power converters, especially when their switching frequencies are increased. By considering the effects of parasitic components, one can modify the converter's circuit design in a way to reduce the effects of parasitic components and set the operating condition so that satisfies the converter's behavioral characteristics.

ACKNOWLEDGMENT

Part of this work was supported by a grant from the Office of Naval Research.

REFERENCES

[1] M. Kchikach, R. Lee, H. F. Weinner, Y. Zidani, Y. S. Yuan, and Z. M. Qian, "Study of the Resonance Phenomenon in Switching Mode Power Supply (SMPS)," *Power Electronics Specialists Conference, 2004. PESC 04. 2004 IEEE 35th Annual*, vol. 4, pp. 3016- 3020, 2004.

[2] S. V. Kulkarni, *Transformer Engineering: Design and Practice*, Marcel Dekker, Taylor & Francis Group, New York, May 2004.

[3] S. Hashino and T. Shimizu, "Characterization of Parasitic Impedance in a Power Electronics Circuit Board using TDR," *Power Electronics Conference (IPEC), 2010 International*, pp. 900-905, June 21-24, 2010.

[4] T.-H. Li, J. Wang, and H. S.-H. Chung, "Effect of Parasitic Elements in a Power Converter on the Switching Performance of a MOSFET-Snubber-Diode Configuration," *Applied Power Electronics Conference and Exposition (APEC), 2011 Twenty-Sixth Annual IEEE*, pp. 364-371, March 6-11, 2011.

[5] M. R. Abdul-Gaffoor, H. K. Smith, A. A. Kishk, and A. W. Glisson, "Simple and Efficient Full-Wave Modeling of Electromagnetic Coupling in Realistic RF Multilayer PCB Layouts," *Microwave Theory and Techniques, IEEE Transactions on* , vol. 50, no. 6, pp. 1445-1457, Jun. 2002.

[6] J.-G. Yook, L. P. B. Katehi, K. A. Sakallah, R. S. Martin, L. Huang, and T. A. Schreyer, "Application of System-Level EM Modeling to High-Speed Digital IC Packages and PCBs," *Microwave Theory and Techniques, IEEE Transactions on*, vol. 45, no. 10, pp. 1847-1856, Oct. 1997.

[7] W. Chen, X. Yang, and Z. Wang, "Application of Wavelets and Auto-Correlation-Function for Cancellation of High-Frequency EMI Noise," *Applied Computational Electromagnetic Society (ACES) Journal*, vol. 24, no. 3, pp. 332 - 336, June 2009.

[8] A. Bhargava, D. Pommerenke, K. W. Kam, F. Centola, and C. Lam, "DC-DC Buck Converter EMI Reduction Using PCB Layout Modification," *Electromagnetic Compatibility, IEEE Transactions on*, vol. 53, no. 3, pp. 806-813, Aug. 2011

[9] R. W. Erickson and D. Maksimovic, *Fundamentals of Power Electronics, Springer*, p. 912, 2nd ed., 2001.

[10] J. Yunas, N. A. Rahman, L. T. Chai, and B. Y. Majlis, "Study of Coreless Planar Inductor at High Operating Frequency," *Semiconductor Electronics, 2004. ICSE 2004. IEEE International Conference on,* p. 5, Dec. 7-9, 2004.

[11] J. Vanek, I. Szendiuch, and J. Hladik, "Optimization of Properties of Planar Spiral Inductors," *Electronics Technology, 30th International Spring Seminar on*, pp. 235-238, May 9-13, 2007.

[12] J.-J. Lee, Y.-K. Hong, S. Bae, J.-H. Park, J. Jalli, G. S. Abo, R. Syslo, B.-C. Choi, and G. W. Donohoe, "High-Quality Factor Ni-Zn Ferrite Planar Inductor," *Magnetics, IEEE Transactions on*, vol. 46, no. 6, pp. 2417-2420, June 2010.

[13] A. Eroglu, "Microstrip Inductor Design and Implementation," *Applied Computational Electromagnetic Society (ACES) Journal*, vol. 25, no. 9, pp. 794 - 800, September 2010.

[14] D. Hui, Z. Yisheng, and Z. Baishan, "Research on the Electromagnetic Radiation of a PCB Planar Inductor," *Microwave Conference Proceedings, 2005.* APMC 2005. Asia-Pacific Conference Proceedings, vol. 1, pp. 3, Dec. 4-7, 2005.

[15] Z. Jonsener, "A New Calculation for Designing Multilayer Planar Spiral Inductors," *Electronics Design Strategy, News*. EDN, July 29, 2010.

[16] N. Y. Abed and O. A. Mohammed, "Frequency Dependent Coupled Field-Circuit Modeling of Armored Power Cables using Finite Elements," *Electromagnetic Field Computation (CEFC), 2010 14th*

Biennial IEEE Conference on, pp.1-1, May 9-12, 2010.

[17] A. S. Alfuhaid, "Frequency Characteristics of Single-Phase Two-Winding Transformers using Distributed-Parameter Modeling," *Power Delivery*, *IEEE Transactions on*, vol. 16, no. 4, pp. 637-642, Oct. 2001.

[18] L. Satish and S. K. Sahoo, "An Effort to Understand What Factors Affect the Transfer Function of a Two-Winding Transformer," *Power Delivery, IEEE Transactions on* , vol. 20, no. 2, pp. 1430-1440, April 2005.

[19] N. N. Rao, *Elements of Engineering Electromagnetics*, Prentice Hall, 6th Edition, pp. 321-324, 2004.

[20] F. T. Ulaby, *Fundamental of Applied Eectromagnetics*, Prentice Hall, 5th Edition, pp. 321-324, 2006.

[21] M. R. Barzegaran, A. Nejadpak, and O. A. Mohammed, "High Frequency Electromagnetic Field Model for the Evaluation of Parasitic Elements in Power Converters," *27th Annual Review of Progress in Applied Computational Electromagnetics*, ACES March 27-31, pp. 623-629, 2011.

[22] C. R. Paul, "*INDUCTANCE Loop and Partial*," published by John Wiley and Sons, 2010.

[23] Y. Saad, *Iterative Methods for Sparse Linear Systems*, 2nd edition, Society for Industrial and Applied Mathematics, 2003.

[24] A. Nejadpak, M. R. Barzegaran, A. Sarikhani, and O. A. Mohammed, "Design of Planar Inductor Based Z-Source Inverter for Residential Alternate Energy Sources," *Applied Power Electronics Conference and Exposition* (APEC), 2011 Twenty-Sixth Annual IEEE, pp. 1698-1703, March 6-11, 2011.

[25] D. E. Goldberg, *Genetic Algorithms in Search, Optimization and Machine Learning*, Addison-Wesley Longman Publishing Co., Inc. Boston, MA, USA, 1989.

Arash Nejadpak (S'09) received his B.S. in Electrical Engineering in 2007 and his M.S. degree in Power Electronics and Electric Machines from Sharif University of Technology, Tehran, Iran in 2009. Currently, he has been a graduate research assistant working towards his Ph.D. degree in Electrical Engineering at Florida International University, Miami, Florida since January 2010. His current research interests include intelligent control of PM machines and development of physics based models and design optimization of power electronic conversion systems.

Mohammadreza Barzegaran (S'10) Obtained B.Sc. and M.Sc. Degrees in Power Engineering from University of Mazandaran (Babol Institute of Technology), Iran in 2007 and 2010, respectively. He is currently pursuing the Ph.D. degree in the department of electrical and computer engineering, Florida International University, Florida, USA. His research interests include studying electromagnetic compatibility in power components, life assessment of electrical power components, fault detection in electrical machines, and also computer-aid simulation of power components.

Osama A. Mohammed (S'79, M'83, SM'84, F'94): Professor Mohammed received his M.S. and Ph.D. degrees in Electrical Engineering from Virginia Polytechnic Institute and State University. He has many years of teaching, curriculum development, research and industrial consulting experience. He authored and co-authored more than 300 technical papers in the archival literature as well as in National and International Conference records in addition to additional numerous technical and project reports and monographs.

Professor Mohammed specializes in Electrical Energy Systems especially in areas related to alternate and renewable energy systems. He is also interested in design optimization of electromagnetic devices, Artificial Intelligence

Applications to Energy Systems as well as Electromagnetic Field Computations in Nonlinear Systems for these energy applications. He has current interest in Shipboard power systems and integrated motor drives. He is also interested in the application communication and sensor networks for the distributed control of power grids. Dr. Mohammed has been successful in obtaining a number of research contracts and grants from industries and Federal government agencies. He has a current active and funded research programs in several areas funded by the office of Naval Research and the US Department of Energy. Professor Mohammed is also interested in developing learning environments and educational techniques for Internet based delivery systems and virtual laboratories.

Professor Mohammed is a Fellow of IEEE and is a recipient of the 2010 IEEE PES Cyril Veinott Electromechanical Energy Conversion Award. Professor Mohammed is also a Fellow of the Applied Computational Electromagnetic Society. He is Editor of IEEE Transactions on Energy Conversion, IEEE Transactions on Magnetics-Conferences, as well as an Editor of COMPEL. He also received many awards for excellence in research, teaching and service to the profession and has chaired sessions and programs in numerous International Conferences in addition to delivering numerous invited lectures at scientific organizations in around the world.

Professor Mohammed serves as the International Steering Committee Chair for the IEEE International Electric Machines and Drives Conference (IEMDC) and the IEEE Biannual Conference on Electromagnetic Field Computation (CEFC). Professor Mohammed was the General Chair of the 2009 IEEE IEMDC conference held in Miami Florida, May 3-6 2009 and was the Editorial Board Chairman for the IEEE CEFC2010 held in Chicago, IL USA, May 9-12, 2010. He was also the General Chairman of the 1996 IEEE International Conference on Intelligent Systems Applications to Power Systems (ISAP'96). Dr. Mohammed has chaired the Electric Machinery Committee for IEEE PES was the Vice Chair and Technical Committee Program Chair for the IEEE PES Electric Machinery Committee for a number of years. He was a member of the IEEE/Power Engineering Society Governing Board (1992-1996) and was the Chairman of the IEEE Power Engineering Society Constitution and Bylaws committee. He also serves as chairman, officer or as an active member on several IEEE PES committees, sub-committees and technical working groups.

Improvement of Accuracy of Extraction of Radiation Patterns from FDTD Modelling of Axisymmetrical Antennas

M. Olszewska and W. Gwarek

Institute of Radioelectronics
Warsaw University of Technology, Warsaw, 00-665, Poland
M.Olszewska@ire.pw.edu.pl, W.Gwarek@ire.pw.edu.pl

Abstract **─** This paper presents a discussion on the accuracy of extraction of radiation patterns of BOR antennas from FDTD simulations. The effect of the "main beam shadow" causing errors in extracted back radiation is explained. The methods of its elimination are proposed.

Index Terms **─** Accuracy, BOR structures, electromagnetic simulations, FDTD method, validation.

I. INTRODUCTION

The FDTD method has proven very useful and accurate in many applications [1]. Mainly software implementations of the FDTD method on classical computer CPUs are known, but recently also hardware accelerated versions are gaining in importance [2]. One of the possible variations of the FDTD method is its version applicable to axisymmetrical problems, denoted also as body of revolution (BOR) problems [3 - 5]. In BOR FDTD, the angular variation of fields is assumed to be known and the general 3D problem is reduced to a computational Vector 2D (or V2D) problem [4]. Reduction of the physical 3D problem to a computational V2D problem results in a drastic reduction (typically by almost two orders of magnitude) of the computing time and memory, without loss of accuracy. Alternatively, we can obtain much better accuracy with a reasonable computing time. Very high accuracy of the simulation results obtained with the BOR FDTD, applied to one or two-reflector antennas, fed by corrugated horns, has been confirmed by experiments. There is however one aspect, which causes our concern. We have found that in antennas with large reflectors (and thus having a large directive gain) the back radiation obtained in simulation is significantly higher than the measured one. Thus, we have launched an investigation to find the reasons for that discrepancy. In this paper, we propose an approach leading to more precise results of the simulation of back radiation.

II. PROPOSED APPROACH EXPLAINED ON AN EXAMPLE OF A DOUBLE REFLECTOR ANTENNA

Consider a double reflector antenna with an operating band from 5.2 GHz to 5.8 GHz, shown in Fig. 1. The radiation pattern obtained for this antenna in BOR FDTD simulations is shown in Fig. 2(a) and (b) (continuous line). It can be seen that the calculated back radiation is about 40 dB lower than the main beam. Having compared the results of simulation and measurements for many similar cases, we suspect that the results might not be accurate. Thus we will investigate in detail possible causes of errors.

A. Method of extraction of the radiation pattern

First of all, we will concentrate on the method of extraction of the radiation pattern. For that purpose, the near-field to far-field transformation, which has been widely studied for the FDTD method [6,7], is performed. It is based on extraction of fields at the so called near-to-far (NTF) surface (also called sometimes a Huygens surface). At that closed surface, the H and E fields (tangential to the "walls" forming the surface) are extracted from the FDTD simulation and used for

Submitted On: May 30, 2011
Accepted On: October 23, 2011

projection of the fields to the far zone. In the case of BOR (V2D) simulations, the NTF walls are reduced to lines and in Fig. 1 we can see them presented as dashed lines. The antenna shown in Fig. 1 radiates predominantly to the right. Thus, the accuracy of extraction of the fields detected at the right NTF line is crucial. However, it is well known that the FDTD analysis provides values of E and H fields at different points of space. Thus, at the right NTF line we can have the accurate value of only one of them. Let us assume that the E-field is extracted exactly at the NTF line, as schematically presented in Fig. 3. Thus, the H-field must be obtained by averaging of the fields extracted half of the FDTD cell to the left and right. Let us try to estimate an error caused by such an averaging.

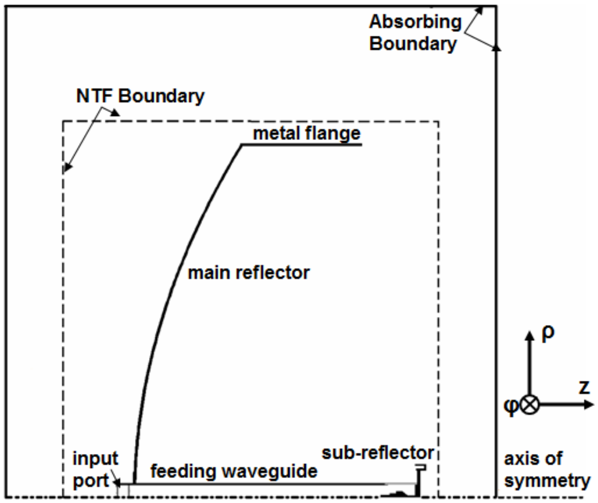

Fig. 1. A sketch presenting the type of simulation scenarios as appearing in a BOR FDTD software. Half of the long section of the structure is considered and meshed.

We assume that the angular E_φ field captured in the FDTD cell centre is equal to:

$$E_\varphi = E_{\varphi 0}\cos(\omega t - \beta z). \qquad (1)$$

The magnetic field, which significantly changes along the direction of the wave propagation, has to be calculated as an average of two values captured at both sides of the cell. Assuming that in the axial z-direction wavelength is λ_z and the FDTD cell size is a, a phase shift corresponding to wave propagation over a distance equal to half of the FDTD cell is:

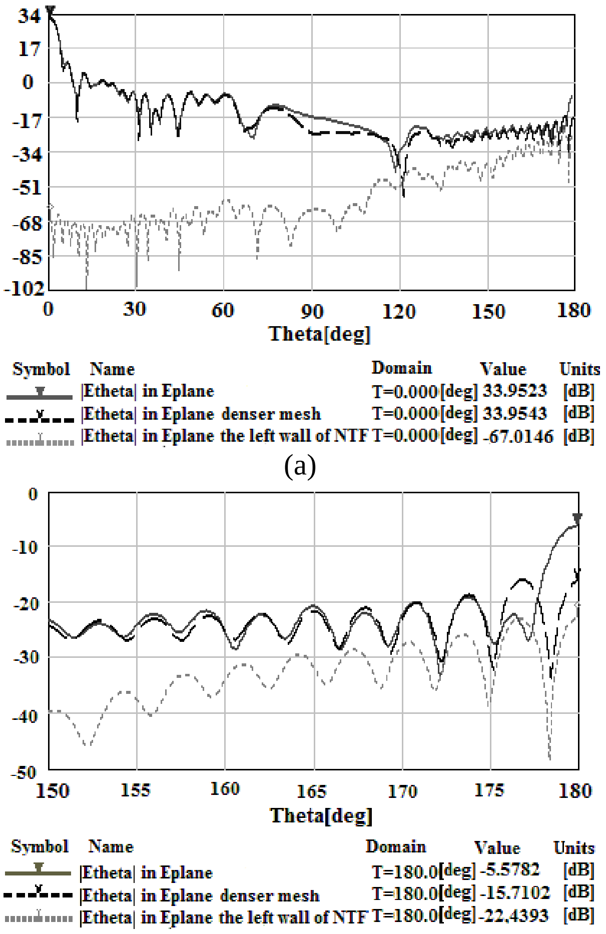

(a)

(b)

Fig. 2. Simulated radiation patterns for E_θ polarisation presented in the entire angle range (a) and in the range 150° - 180° (b); a typical scenario (continuous line), denser mesh in the right NTF boundary region (dashed line), integration only on the back NTF surface (dotted line).

$$\phi = \frac{360°}{\lambda_z}\frac{a}{2}. \qquad (2)$$

For a pure travelling wave with the wave impedance equal to Z_0, we thus obtain the H_ρ field averaged at the cell centre as:

$$H_\rho = -\frac{E_{\varphi 0}}{2Z_0}\left[\cos(\omega t - \beta z - \phi) + \cos(\omega t - \beta z + \phi)\right] = -\frac{E_{\varphi 0}}{Z_0}\cos(\omega t - \beta z)\cos(\phi). \qquad (3)$$

The H field estimation error can be expressed as:

$$\delta_H = \cos\phi. \qquad (4)$$

In the considered scenario, the cell size is about 3 mm, which means that the half-cell, at 5.2 GHz corresponds to 9.4° of the phase shift. This modifies the amplitude of the magnetic field by about 1.34%. Since δ_H further corresponds to a modification of the wave impedance, we get:

$$Z_0' = \frac{E_\phi}{H_\rho} = 1.0134 Z_0 . \qquad (5)$$

When the wave impedance deviates from Z_0, it means that the software detects a partially standing wave. The detected standing wave ratio VSWR is equal to that deviation:

$$\frac{Z_0'}{Z_0} = SWR = \frac{1+|\Gamma|}{1-|\Gamma|} \cong 1 + 2|\Gamma| , \qquad (6)$$

where Γ is a hypothetical reflection coefficient detected at the NTF surface. In the considered case, we get the corresponding reflection coefficient equal to 0.0067. That way the NTF surface produces in the back direction a “shadow” of the main beam. The “shadow” appears at the level of about -43 dB.

According to the above discussion, it is concluded that, in the considered example, the calculation of the back radiation at the levels of 40 dB or less below the main beam is unreliable and can be explicable as a numerical error. It should be mentioned that an imperfect absorbing boundary at the right of the computational domain may also cause some standing wave effects contributing to the “main beam shadow” effect.

B. Methods of eliminating the main beam shadow

To verify the above hypotheses, additional simulations with denser meshing (cell size about 1.5 mm) close to the right NTF boundary and the right absorbing boundary region are performed. The results are shown in Figs. 2(a) and (b) (dashed curves). The calculated back radiation is about 10 dB lower than in the original scenario, which confirms our hypotheses and improves the accuracy of backward radiation extraction. However, in practical calculations the remaining level of errors may still be unacceptable. Moreover, the software user may find it difficult to distinguish the physical result from the parasitic one. Can that error be eliminated at its source? In principle, the effect of H-field averaging could be eliminated, dividing the H-field value as in equation (3) by a correction factor defined by equations (2) and (4). However, this is impractical in a general case, since the direction of wave propagation at the NTF surface needed for calculating λ_z in equation (2) is unknown. Furthermore, such a correction would not suppress standing wave errors due to numerical reflections from absorbing boundaries.

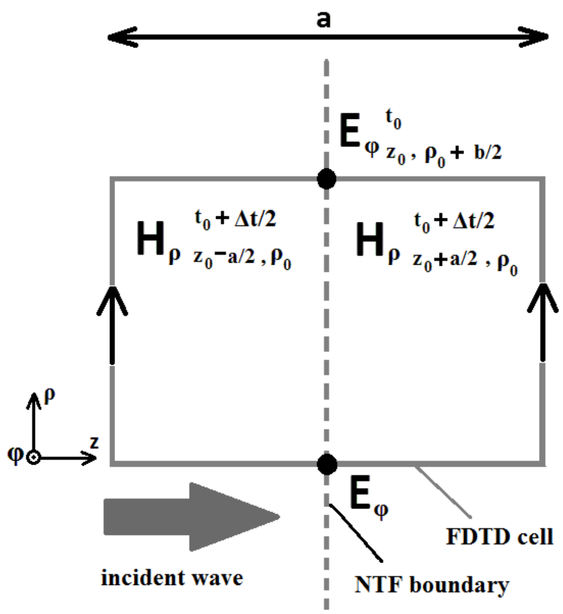

Fig. 3. Scheme of the extraction of the fields at NTF boundary.

In this work, we propose an alternative method of eliminating the “main beam shadow”. The method consists of comparing the radiation patterns calculated using all three NTF lines with the radiation patterns calculated using only the contribution of the left NTF line. The results obtained in the one-line simulation are presented by dotted curves in Figs. 2(a) and (b). The obtained radiation pattern is naturally wrong for angles within the main forward beam, but it is correct for 180°. It indicates the back radiation of about 56 dB down from the main beam. The results of all the performed simulations are summarized in Table 1.

C. Periodic behaviour of the back radiation pattern

In Fig. 2(b), we can see that the back radiation close to 180° is composed of periodic minima and maxima. The question to be asked is, whether this is a numerical effect or a physical one. While analyzing the field distribution of the considered antenna, we have concluded that the main source of the back radiation is the outer edge of the parabolic main reflector. We can therefore say that the source has a shape of a circle of diameter equal to 900 mm.

Consider a loop antenna, approximating such a backward radiation source. At its opposite sides we would have two maxima of the current. In the Cartesian coordinate system, the current will have the same directions at those points, as it is shown schematically in Fig. 4.

Table 1: Values of the back radiation obtained for the considered scenarios

Scenario	**Back radiation level (with respect to the main beam)**
Typical	-40 dB
Denser meshing around right NTF and absorbing boundary	-50 dB
Considering the contribution of only left NTF line	-56 dB

Thus, we are essentially considering a set of two dipoles excited in phase and separated by the distance of 900 mm. At f=5.2GHz the dipoles form the radiation pattern with a maximum at θ_{max}=180° and the first minimum at θ_{min} such that:

$$\theta_{min} = \text{arc sin}\left(\frac{\lambda}{2D}\right) = 1.8^\circ . \qquad (7)$$

Looking at the radiation patterns of Fig. 2(b), we find that the value from equation (7) corresponds to what we see. It can be concluded that the effect of ripples in the back radiation pattern is formally physical - and not numerical. However, “physical” does not mean “realistic” here. Our discussion has been based on an idealistic assumption that the external edge of the antenna is perfectly axisymmetrical. In the technological reality, the shape of the reflector edge is slightly perturbed and thus the sharp radiation ripples in back radiation do not appear. Thus, as a practically measurable level of the back radiation, we should take a kind of average of the pattern over a reasonable angle range. Having compared the results of simulation and measurements for the cases similar to the one considered here, we have concluded that the averaging angle should be about 3°.

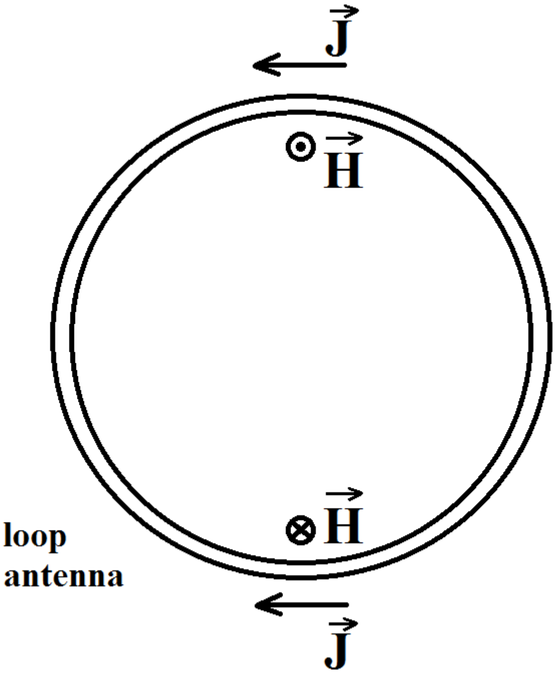

Fig. 4. Axial magnetic field and angular current in the loop antenna - a schematic view.

III. CONCLUSIONS

The paper has presented typical causes of errors in the extraction of back radiation of axisymmetrical antennas analyzed by the BOR (V2D) FDTD method. The effect of the “main beam shadow” has been investigated in detail and the approach for improving the accuracy of the analysis has been proposed.

The results presented in this paper have been obtained with working versions of our in-house V2D FDTD codes. Based on the resulting recommendations, a procedure for deleting user-selected walls of the Huygens surface from the near-to-far field transformation has been implemented in the QW-V2D software [8]. Its results coincide with those shown in the paper.

In future work, we shall validate our conclusions for general 3D (i.e., not necessarily axisymmetrical) high-directivity antennas and against commercial 3D FDTD packages, which are more abundant on the electromagnetic software market.

REFERENCES

[1] A. Taflove and S. C. Hagness, *Computational Electromagnetics - The Finite-Difference Time-Domain Method*, 3rd ed., Artech House, Norwood MA, 2005.

[2] P. F. Curt, J. P. Durbano, M. R. Bodnar, S. Shi, and M. S. Mirotznik, "Enhanced Functionality for Hardware-Based FDTD Accelerators", *Applied Computational Electromagnetic Society (ACES) Journal*, vol. 22, no. 1, pp.39-46, March 2007.

[3] M. Celuch and W. K. Gwarek, "Industrial Design of Axisymmetrical Devices using Customized Solver from RF to Optical Frequency Band," *IEEE Microwave Magazine*, vol. 9, no. 6, pp. 150-158, Dec. 2008.

[4] W. K. Gwarek, T. Morawski, and C. Mroczkowski, "Application of the FDTD Method to the Analysis of Circuits Described by the Two-Dimensional Vector Wave Equation," *IEEE Trans. Microwave Theory Tech.*, vol. MTT-41, no. 2, pp. 311–317, Feb. 1993.

[5] C. Mroczkowski and W. K. Gwarek, "Microwave Circuits Described by Two-Dimensional Vector Wave Equation and Their Analysis by FD-TD Method," in *Proc. 21st European Microwave Conf., Stuttgart*, pp. 199–204, Sept. 1991.

[6] J. A. Roden, S. L. Johns, and J. Sacchini, "An Improved Time-Domain Near-Field to Far-Field Transform in Two Dimensions," *Applied Computational Electromagnetic Society (ACES) Journal*, vol. 23, no. 1, pp. 1-4, March 2008.

[7] T. Martin and L. Pettersson, "FDTD Time-Domain Near- to Far-Zone Transformation above a Lossy Dielectric Half-Space," *Applied Computational Electromagnetic Society (ACES) Journal*, vol. 16, no.1, pp. 45 - 52, March 2001.

[8] www.qwed.eu

Marzena Olszewska received the B.Sc. and M.Sc. degree from the Warsaw University of Technology. She is a Ph.D. student at the Warsaw University of Technology, Institute of Radioelectronics. Her research activity deals with double reflector antennas of a small size.

She is employed in QWED company, the vendor of QuickWave software for electromagnetic design.

Wojciech K. Gwarek graduated in 1970 from the Faculty of Electronics, Warsaw University of Technology. He obtained the M.Sc. degree from M.I.T. (EE'74). After returning to Poland he continued his work at the Warsaw University of Technology from where he received his Ph.D. (1977) and habilitation (1988) and where he is currently a professor. His teaching activities include lectures on electromagnetic theory, microwave technology and electromagnetic compatibility.

Professor Gwarek is the author of more than 200 technical papers and a text book on electromagnetic theory used in Poland since 1977. For the last 30 years, he has been reviewing papers for many of the leading archive journals and served as a TPC member for many international conferences. In 2008 and 2010, he was a co-chair of the TPC of the MIKON International Conference on Microwaves Radar and Wireless Communication. In the years 2003-2005, he served as a Distinguished Microwave Lecturer of the IEEE. Since 2001, he is a Fellow Member of the IEEE. He is a worldwide recognized expert on industrial design of microwave equipment involving electromagnetic modeling. In 2011, he obtained the IEEE Microwave Pioneer Award for his contribution to the theory and applications of electromagnetic modeling.

Electromagnetic Point Source Reconstruction by Reversed-TLM Method

Alina Ungureanu, Tan-Phu Vuong, and Fabien Ndagijimana

IMEP-LAHC Laboratory, 3 Parvis Louis Neel, Grenoble, 38016, France
alina.ungureanu@minatec.inpg.fr, tan-phu.vuong@minatec.inpg.fr, fabien.ndagijimana@minatec.inpg.fr

Abstract **─** Classical methods for source synthesis are iterative, time consuming, and not always adapted to the desired problem. In this paper, we present a new method of electromagnetic source synthesis based on the time-reversal technique. This approach employs the *reversed*-TLM method and permits the reconstruction of a source distribution, from its electromagnetic far-field radiation. Point-like source reconstruction results show that by using this method, the "classical" half-wavelength resolution limit is overcome.

Index Terms **─** Electromagnetic simulation, inverse problem, source synthesis, TLM method.

I. INTRODUCTION

Traditional methods for radiating electromagnetic (EM) structure design typically begin by defining the architecture of the source distribution. An iterative procedure is then developed to ensure that the design process converges to an optimal solution [1-3]. Even if performance of such techniques in the frequency domain (FD) is good, convergent procedure is not efficient in the time domain (TD). Time reversal (TR) comes as a natural method for EM structure design. This technique was first applied in acoustics [4-6], and more recently in electromagnetics [7-9], answering some important questions, like those related to inverse problem solution non-uniqueness [10], and resolution limitations [11, 12].

Our purpose is to use this TR wave theory and to introduce an innovative TD based algorithm adapted to EM source synthesis. The numerical method that we use is the *reversed*-TLM (transmission-line matrix method), based on symmetrical condensed nodes (SCN) [13].

This paper is basically focused on EM point source reconstruction, using the radiating field outside the region containing the sources. Theoretical concepts as "time reversal mirrors" (TRM) [6] and "time reversal cavity" (TRC) [8] are used. Inverse source problems (ISP) have been already studied, analytically, in FD [14, 15] and in TD [16]. TLM method has been previously used for solving numerous EM problems, which cover various domains of applications. The basics of the time-reversed TLM process have been introduced in [17]. This technique has been applied previously in ISP [18], microwave filter synthesis [19-21], and inverse diffraction applications [22, 23].

In inverse diffraction problems [23], the object to be reconstructed is illuminated by a plane wave excitation. Two direct simulations are performed: a first one with the object and a second one without the object. The EM field history is recorded, in both cases, on the TRC surface. The difference between the outputs of the two simulations, i.e. the diffracted field, is injected in the reversed simulation. In our case, there is no plane wave excitation. Besides, only one direct TLM simulation is performed. Our goal is to find the information to be added at the beginning of the TR approach, in order to find the initial source distribution, by a reversed TLM simulation only. In this way, the knowledge of amplitudes and phases of the radiating field and the knowledge of the excitation would be sufficient to find primary or secondary sources.

Our method is first applied to lumped wide band sources, in the frequency range [26GHz - 34GHz], placed in a lossless, homogeneous, and non-dispersive 3D free-space. Results show that the well-known spatial resolution limitation of the

Submitted On: May 30, 2011
Accepted On: October 8, 2011

reconstruction is solved. A sub-wavelength resolution is achieved.

II. RETRO-PROPAGATION BY REVERSED-TLM METHOD

Theory of wave propagation TR is based on the invariance property of the scalar wave equation (1) under TR transformation, in a lossless space:

$$\left(\nabla^2 - \frac{1}{c^2}\frac{\partial^2}{\partial t^2}\right)\psi(\vec{r},\vec{r}_0,t) = 0, \qquad (1)$$

where $\psi(\vec{r},\vec{r}_0,t)$ is the scalar radiated field, $\vec{r}$ is the distance-vector between the source and the observation point, $\vec{r}_0$ is the source position, t is the time and c is the speed of light.

This equation is a differential one, containing only a second order derivative with respect to time. Therefore, if $\psi(\vec{r},\vec{r}_0,t)$ is a solution of this equation, then $\psi(\vec{r},\vec{r}_0,-t)$ is also a solution [24], [25]. In other words, scalar wave equation remains invariant under TR transformation. This property is valid only for a non-absorbing medium.

It can be shown that Maxwell's equations are also symmetrical under TR [25]. So, if $\vec{E}(\vec{r},t)$ and $\vec{H}(\vec{r},t)$ are solutions of Maxwell's equations, then $\vec{E}(\vec{r},-t)$ and $-\vec{H}(\vec{r},-t)$ are solutions of the same set of equations. Following Huygens's principle, the knowledge of the radiated field on a closed surface surrounding the sources is sufficient to recreate the field inside the entire volume.

We use the 3D *reversed*-TLM method, with SCN nodes, to numerically simulate EM wave retro-propagation in TD. The propagation space is represented by a mesh of interconnected transmission lines [13].

Reversed-TLM simulation is identical to the direct one due to the scattering node matrix uniqueness property ($[S]^{-1}[S] = I$) [17]. Thus, an EM radiation process can be theoretically time-reversed without any change. The unique difference is that initial conditions change.

III. RECONSTRUCTION PROCEDURE

Our new algorithm based on 3D wave retro-propagation, permits the reconstruction of an unknown source distribution from its radiated field. So, despite the fact that the solution to inverse problems is not unique, we are proving the feasibility of this method under some circumstances. Thus, some *a priori* information about the solution of the initial inverse problem is added. The knowledge of the transmitted waveform transforms the initial ill-posed problem in a well-posed one, with a unique solution.

We developed a *two-step* method to determine the position and the dimensions of the sources from measured- or theoretically-computed radiated-field values. The two steps of the method are: the coarse reconstruction step and the resolution improvement one. We exploit this method as follows.

A. Coarse reconstruction step

From the sampled values of the desired far-field radiation, we reconstruct the excitation to apply in each point of the cubical TRC external surface. The six TRC faces are called TRMs (Fig. 1a). In order to create the proper wave re-composition during the TR process, the excitation of the TLM nodes, on the six TRMs, needs delay compensation. Hence, for a proper reconstruction of the excitation, we also need the delay information at each point of the TRMs. Reconstructed signals are injected in the TLM network, in each point of the TRM. Reversed-TLM method is then applied.

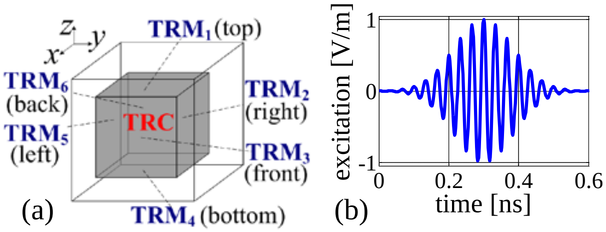

Fig. 1. (a) TRC 3D; (b) excitation signal: *f*(*t*).

Considering the new established boundary conditions on the TRMs, a time-reversed field (ψ_{TR}) retro-propagates in all the volume [4]. This field satisfies the Helmholtz equation without sources (2).

$$\left(\nabla^2 - \frac{1}{c^2}\frac{\partial^2}{\partial t^2}\right)\psi_{TR}(\vec{r},t) = 0. \qquad (2)$$

As a consequence, ψ_{TR} has the following form:

$$\begin{aligned}&\psi_{TR}(\vec{r},\vec{r}_0,t) = \\ &= G(\vec{r},\vec{r}_0,-t) * f(-t) - G(\vec{r},\vec{r}_0,t) * f(-t),\end{aligned} \qquad (3)$$

where $G(\vec{r},\vec{r}_0,t)$ is the Green's function, *f*(*t*) is the initial temporal excitation and "$*$" is the temporal convolution operator.

Thus, the TR operation generates a convergent wave focusing on the initial source position (Fig. 2a) and a divergent wave, which appears after the collapse (Fig. 2c). So, in the proximity of the initial source position there is a superposition of these two waves (Fig. 2b).

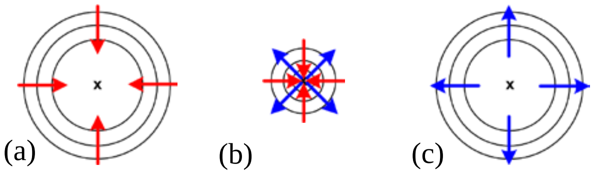

Fig. 2. Time-reversed waves' focalization; (a) convergent wave; (b) interference between convergent and divergent wave in the proximity of the source; (c) divergent wave.

Therefore, if we apply the *reversed*-TLM method based on this approach, TR field does not focus perfectly on the initial source position. Besides, even if both waves have a singularity in $\vec{r}_0$, the TR field has a finite nonzero value at this initial source position. Hence, there is no spatial discontinuity of the retro-propagated field. It has been shown [5] that the TR field has a well-known sinus cardinal form: $\psi_{\mathrm{TR}}(\vec{r},t) \approx \sin_{\mathrm{c}}(kR)$, (where $R = \|\vec{r}-\vec{r}_0\|$ and $k = 2\pi/\lambda$ is the propagation constant). This means that the TR field has a maximum value at the initial source position ($\vec{r}_0$) and a λ main lobe width.

So, this *first step* gives a coarse determination of the source distribution. The spatial resolution depends on the transmitted signal wavelength, via the well-known diffraction-limit. In order to determine the exact location and dimensions of the sources, a better reconstruction-resolution is required. Starting from the result of this *first step*, a *second step* is performed in order to improve the resolution.

B. Resolution improvement step

The key to the resolution issue [26], is mathematically found by time-reversing the Helmholtz equation with sources. The ideal TR field would be:

$$\psi_{\mathrm{TR}}^{\mathrm{ideal}}(\vec{r},\vec{r}_0,t) = \psi(\vec{r},\vec{r}_0,-t) = G(\vec{r},\vec{r}_0,-t) * f(-t). \qquad (4)$$

It appears that the TR field obtained after the coarse reconstruction step is composed of a convergent and a divergent wave. In order to correct this wave superposition effect, the divergent wave should be cancelled.

Let $\psi_{\mathrm{TRM}}(\vec{r},t)$ be the theoretically computed field on the TRMs. This field is injected, during the *first step*, in the TRMs, in order to find the sources. So, the solution to our issue is to excite, during the *second step*, the time-reversed initial excitation: $f(-t) \equiv f(T-t)$ ($T > \mathrm{supp}(f) + \tau$, where $\mathrm{supp}(f)$ is the support of *f*, $\tau = d_{\mathrm{TRM\text{-}source}}/c$ and $d_{\mathrm{TRM\text{-}source}}$ is the distance between the source distribution position and the TRMs position). $f(-t)$ is excited in the source probable positions, in the same time as $\psi_{\mathrm{TRM}}(\vec{r},t)$. To find these positions, we locate, after the *first step*, the maximums of the field amplitude. This time-reversed initial excitation acts like a sink that absorbs the convergent waves during the collapse and cancels the divergent wave.

IV. RESULTS

One of our objectives was to reconstruct EM point-like sources placed in a homogeneous, non-dispersive, and lossless free space. The approach is applied in its simplest form and environment because we want to study the phenomena without introducing any additional dispersion. This application allows a first validation of the proposed reconstruction procedure.

The TLM mesh was excited with a wideband signal, having a central frequency of 30GHz (Fig. 1b). The amplitude-phase distribution of the radiated field on the cubical TRC is used as initial information. A spatial step size of $\Delta l = 0.1\lambda = 1$mm is chosen for the TLM mesh.

It is important to emphasize that our objective is to realize the TR from a desired radiation pattern and not from real-time signals recorded after the direct approach. In order to get closer to this idea, we use as a starting point of our simulations, for each node of TRMs, only two values: maximum amplitude sample and its correspondent delay.

The described procedure is first applied in order to reconstruct a point-like source of 1mm in diameter, placed in the middle of the cubical TRC of (10x10x10)cm^3 (Fig. 3a). Reconstructed E_z field component amplitude is represented, in the plane containing the source, during the TR (Fig. 4a-d).

We observe that the divergent wave is cancelled after the second step (Fig. 4e-h), with *f*(-*t*) plotted in Fig. 3b. A λ/10 resolution of the reconstruction is obtained (Fig. 5).

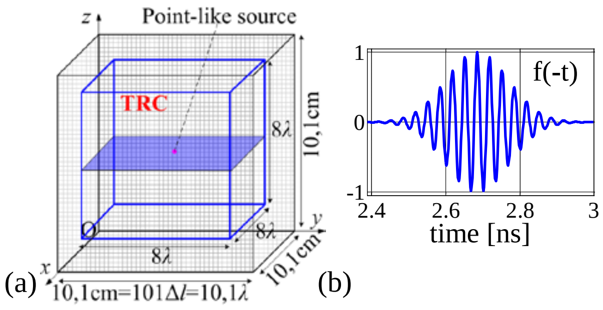

Fig. 3. (a) Point-like source; (b) the sink: *f*(-*t*).

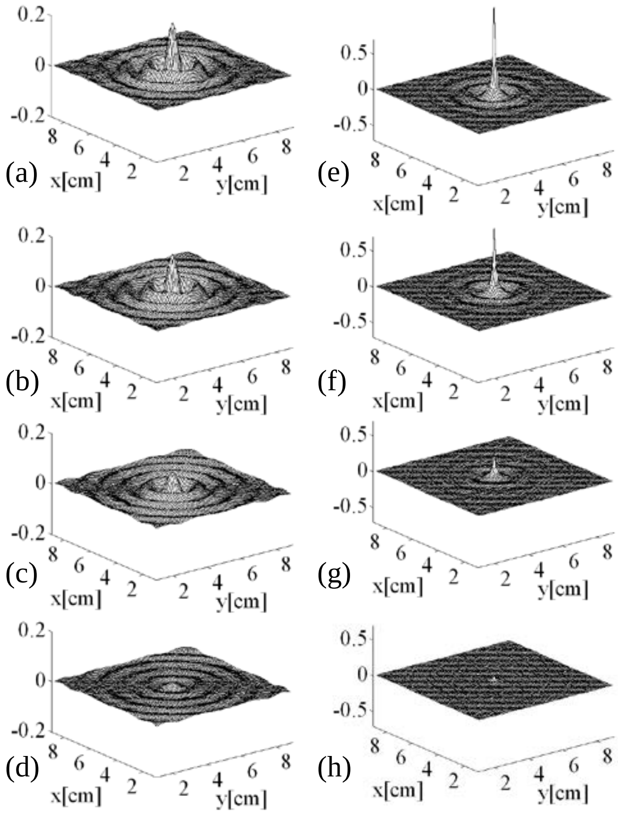

Fig. 4. (a)-(d) - reconstructed source after the *first step*; (e)-(h) - reconstructed source after the *second step*. Process was stopped at 0.366ns, 0.433ns, 0.5ns, 0.566ns.

The same procedure is then applied to reconstruct two identical point-like sources, each of 1mm in diameter and spaced 2λ between centres (Figs. 6a, b). Reconstructed E_z field component amplitude is represented in the plane containing the sources, after the TR (Figs. 7a, b). A good reconstruction resolution of the two sources is achieved in this case as well. The reconstruction of multiple point sources, with any phase delay, can be done from the knowledge of the amplitude- and phase- distribution on the TRCs external surface. The reconstruction of two point sources, excited by two signals in phase opposition, is represented in Fig. 8a.

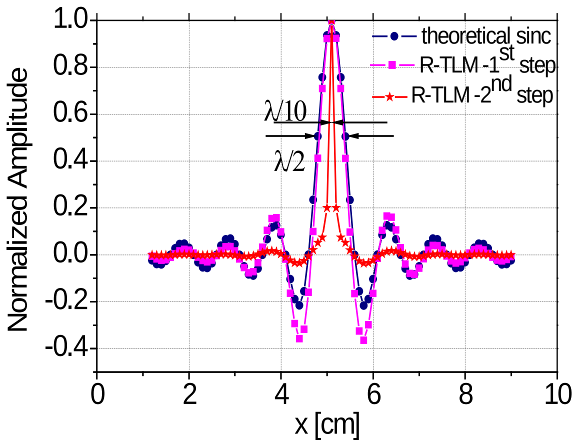

Fig. 5. Focal spot cross-section.

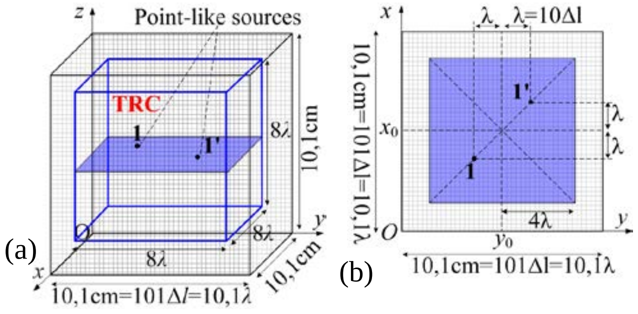

Fig. 6. Two point-like sources: (a) TRC 3D; (b) cross-section.

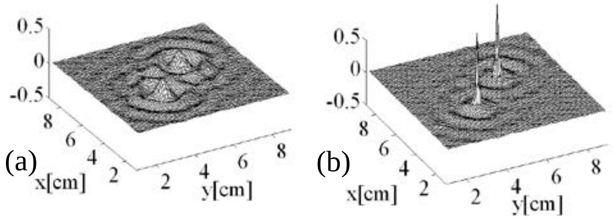

Fig. 7. Reconstructed sources: (a) after the *first step*; (b) after the *second step*.

Hence, we can reconstruct multiple point-like sources, provided that the distance between each of them is at least half the wavelength of the excitation. The reconstruction of a line-like source of 9mm in length is represented in Fig. 8b. The process leads to a widened asymmetrical focal spot. The field obtained after the TR shows an amplitude equalization problem at the initial source positions. The study of more complex sources is under development. Further on, this approach can be used to reconstruct other source distribution shapes or RF devices, e.g. antennas.

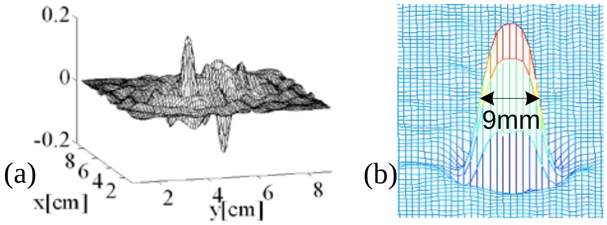

Fig. 8. Reconstruction result of: (a) two point sources in phase opposition; (b) a line-like source.

V. CONCLUSIONS

In this paper, we introduced a new method of EM source synthesis based on wave TR. This approach employs the *Reversed*-TLM method and permits the reconstruction of a source distribution, from its far field radiation.

We showed that it is indeed possible to reconstruct EM point-like sources from their radiated far field. Our proposed *two-step* method begins with a coarse reconstruction step, which gives the approximate positions and dimensions of the sources. The results of this *first step* depend on the excitation wavelength. A *second step* is thus performed in order to increase the resolution of the reconstruction.

Results show that after the resolution improvement step, the diffraction limit is exceeded. These encouraging results let us conclude that the Reversed-TLM method may provide a useful and important new tool for EM source synthesis.

REFERENCES

[1] C. Balanis, *Antenna Theory Analysis and Design*, 2nd ed, John Wiley & Sons, Inc., 1997.

[2] C. Baum, “The Complementary Roles of Analysis, Synthesis, Numerics, and Experiment in Electromagnetics,” *Applied Computational Electromagnetic Society (ACES) Journal*, vol. 20, no. 3, pp. 157-168, November 2005.

[3] R. Ghayoula, N. Fadlallah, A. Gharsallah, and M. Rammal, “Design, Modelling, and Synthesis of Radiation Pattern of Intelligent Antenna by Artificial Neural Networks,” *Applied Computational Electromagnetic Society (ACES) Journal*, vol. 23, no. 4, pp. 336-344, December 2008.

[4] M. Fink, C. Prada, F. Wu, and D. Cassereau, “Self Focusing in Inhomogeneous Media with Time Reversal Acoustic Mirrors,” *IEEE Ultrasonic Symposium*, Montréal, Québec, 1989.

[5] M. Fink, "Time-Reversal of Ultrasonic Fields 1. Basic Principles," *IEEE Trans. Ultrason. Ferroel. and Freq. Control*, vol. 39, pp. 555-566, 1992.

[6] M. Fink and C. Prada, "Acoustic Time-Reversal Mirrors," *Inverse Problems*, vol. 17, pp. R1-R38, 2001.

[7] G. Lerosey, A. Tourin, A. Derode, G. Montaldo, and M. Fink, “Time Reversal of Electromagnetic Waves,” *Physical Review Letters*, vol. 92, 2004.

[8] R. Carminati, R. Pierrat, J. de Rosny, and M. Fink, "Theory of the Time Reversal Cavity for Electromagnetic Fields," *Optics Letters*, vol. 32, pp. 3107-3109, 2007.

[9] J. de Rosny, G. Lerosey, and M. Fink, "Theory of Electromagnetic Time-Reversal Mirrors," *IEEE Trans. Ant. & Propag.*, vol. 58, pp. 3139-3149, 2010.

[10] N. Bleistein and J. K. Cohen, "Nonuniqueness in Inverse Source Problem in Acoustics and Electromagnetics," *Journal of Mathematical Physics*, vol. 18, pp. 194-201, 1977.

[11] G. Lerosey, J. de Rosny, A. Tourin, and M. Fink, "Focusing Beyond the Diffraction Limit with Far-Field Time Reversal," *Science*, vol. 315, pp. 1120-1122, 2007.

[12] M. Fink, J. de Rosny, G. Lerosey, and A. Tourin, "Time-Reversed Waves and Super-Resolution," *C. R. Physique*, vol. 10, pp. 447-463, 2009.

[13] P. B. Johns, “A Symmetrical Condensed Node for the TLM Method,” *IEEE Trans. Microwave Theory and Techniques*, vol. MTT-35, no. 4, pp. 370-377, 1987.

[14] E. A. Marengo and A. J. Devaney, “The Inverse Source Problem of Electromagnetics: Linear Inversion Formulation and Minimum Energy Solution,” *IEEE Trans. Ant. Propag.*, vol. 47, pp. 410-412, 1999.

[15] A. J. Devaney, E. A. Marengo, and M. Li, "Inverse Source Problem in Non-Homogeneous Background Media," *SIAM J. Appl. Math.*, vol. 67, pp. 1353-1378, 2007.

[16] E. A. Marengo and A. J. Devaney, "The Inverse Source Problem in the Time Domain," *IEEE AP-S Symp.*, vol. 1, pp. 694-697, 1998.

[17] R. Sorrentino, P. M. So, and W. J. R. Hoeffer, "Numerical Microwave Synthesis by Inversion of the TLM Process," *21st Euro Microwave Conf. Dig.*, Stuttgart, Germany, pp. 1273-1277, 1991.

[18] Y. Zhang, M. H. Bakr, and N. K. Nikolova, "An Efficient Algorithm for Solving Inverse Source Problems using Time Domain TLM," *IEEE Ant. & Propag. Soc. Int. Symp.*, 2010.

[19] L. de Menezes, "New Developments in the Inverse Scattering TLM (Transmission Line Matrix) Method," *Imoc 2001: Proc. of the 2001 Sbmo/Ieee Mtt-S Int. Microwave and Optoelectronics Conf.*, pp. 403-406, 2001.

[20] I. Scott, A. Vukovic, and P. Sewell, "Reducing the Computational Requirements of Time-Reversal Device Optimizations," *Int. Journal Num. Model.-Elec. Net. Devices & Fields*, vol. 23, pp. 458-469, Nov.-Dec. 2010.

[21] M. H. Bakr, P. P. M. So, and W. J. R. Hoefer, "The Generation of Optimal Microwave Topologies using Time-Domain Field Synthesis," *IEEE Trans. Micro. Theo. & Tech.*, vol. 50, pp. 2537-2544, 2002.

[22] M. Forest and W. J. R. Hoefer, "A Novel Synthesis Technique for Conducting Scatterers using TLM Time-Reversal," *IEEE Trans. Micro. Theo. & Tech.*, vol. 43, pp. 1371-1378, 1995.

[23] S. Barraud, J. L. Dubard, and D. Pompei, "3D-TLM Pattern Recognition in Free Space," *IEE Proc. Microwave Ant. and Propag.*, vol. 145, no.5, pp. 387-391, 1998.

[24] M. Fink, "Time-Reversed Acoustics," *Scientific American*, vol. 281, pp. 91-97, 1999.

[25] R. Snieder, "Time-Reversal Invariance and the Relation between Wave Chaos and Classical Chaos," *Imag. of Complex Med. with Acoustic & Seismic Waves*, vol. 84, pp. 1-15, 2002.

[26] J. de Rosny and M. Fink, "Overcoming the Diffraction Limit in Wave Physics using a Time-Reversal Mirror and a Novel Acoustic Sink," *Physical Review Letters*, vol. 89, 2002.

Alina Ungureanu obtained the Engineer degree and the Master degree, in Electronics and Telecommunications, from the Polytechnic University of Bucharest (UPB), Romania.

She is currently pursuing a PhD degree at Joseph Fourier University (UJF), Grenoble, France. The subject of her Ph.D. is "Radiating wideband source synthesis by Reversed-TLM method". Her research interests include computational electromagnetics with applications in antennas, microwaves and EMC.

Tan-Phu Vuong (senior member IEEE) received his Ph.D. degree in Microwaves from INP de Toulouse (France), in 1999.

From 2001 to 2008, he was an Associate Professor in microwave and wireless systems at the ESISAR high school of engineer of Grenoble INP. Since 2008, he is Professor at Phelma high school of engineer of Grenoble INP. His research interests include modelling of passive microwave and mm-wave integrated circuits. His current research interests include design of small antennas and printed antennas for mobile, RFID, design of passive and active mm-wave components.

Fabien Ndagijimana received his Ph.D. in Microwave and Optoelectronics, in 1990, at INP de Grenoble, France. He then joined the faculty of Electrical Engineering ENSERG as associate Professor where he teaches microwave techniques and EM modelling. Since 1997, he joined the Joseph Fourier University, where he is professor at IUT.

His research activity focuses on the characterization and EM modelling of microwave and devices, and their integration on Silicon & SOI technologies for wireless RF applications. The actual research activity includes integrated antennas for microwave and mm-wave applications, electrical characterization of associated material and substrates, and development of 3D EM simulation tools.

Combined Bowtie–Peano Antennas for Wideband Performance

Ioannis I. Papadopoulos-Kelidis, Antonios X. Lalas,
Nikolaos V. Kantartzis, and Theodoros D. Tsiboukis

Department of Electrical and Computer Engineering
Aristotle University of Thessaloniki, Thessaloniki, GR-54124, Greece
gianniskelidis@yahoo.gr, lant@faraday.ee.auth.gr, kant@auth.gr, tsibukis@auth.gr

Abstract **─** The concept of the folded bowtie wideband antennas is introduced in this paper. To this aim, the design procedure employs a Peano space-filling curve approach which leads to an entire family of combined bowtie-Peano antennas (BPA). The new structures efficiently blend the broadband performance of bowtie antennas with the compactness of Peano forms. In this context, two alternative devices are proposed and thoroughly investigated. Numerical results derived by means of a finite-difference time-domain (FDTD) technique clearly reveal the behavior and the merits of the novel radiators, signifying, also, the feasibility of bandwidth enhancement at specific resonances.

Index Terms **─** Bowtie antennas, FDTD methods, miniaturized antennas, Peano antennas.

I. INTRODUCTION

An issue of paramount significance in contemporary RF technology is the multi-parametric design of highly competent and reliable antennas. When embedded in wireless networks or advanced communication systems, these structures are expected to exhibit various benefits, like compactness combined with functionality in lower frequencies, irrespective of their physical size. The primary idea for the accomplishment of the prior features at a single antenna is to fold a dipole in such a manner that fits into a small area, yet preserving its resonances at the same frequency regions. From this viewpoint, space filling curves [1-5] can be utilized to meet these requirements and effectively tackle any shortcomings of the design process. Among them, Peano antennas [6-8] comprise a practical and proficient selection with respect to high compression ratio. In fact, their small electrical size associated with a satisfactory multi-band behaviour can easily justify their noteworthy contribution in diverse applications.

Of critical essence, as well, is the wideband performance of wireless RF apparatuses. A popular structure for broadband designs is the bowtie antenna [9-11]. Although, its overall operation resembles that of a dipole, this particular radiator attains a sufficiently enhanced bandwidth. On the other hand, careful research on this aspect has confirmed that Peano space-filling curves can lead to miniaturized configurations with acute, but narrowband, resonances [12-14]. As a consequence, it becomes apparent that the combination of the preceding concepts is likely to provide adequately wideband and noticeably compact devices, which meet all modern antenna functional standards.

It is the objective of this paper to elaborately examine the radiation characteristics of efficient bowtie structures folded in terms of the Peano space-filling curve. Two novel antennas are carefully designed in order to merge the desired attributes of the aforementioned designs. In the first case, a bowtie-shaped metallic path is introduced, while in the latter the outline of Peano's footprint is transformed into a bowtie shape. The performance of the combined bowtie-Peano antennas (BPA) is numerically studied via a finite-difference time-domain (FDTD) scheme and compared to that of a typical Peano antenna, considering the multiple resonances of both devices. Analysis proves that the proposed structures achieve notably improved bandwidths with very limited dimensions.

Submitted On: May 31, 2011
Accepted On: August 24, 2011

II. CONVENTIONAL PEANO ANTENNA

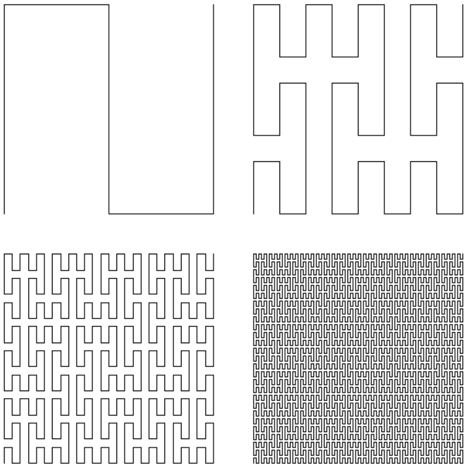

Fig. 1. Geometry of the Peano curves for the first four iteration orders.

Space filling curves constitute a mathematical conception for the compression of a straight line into a restricted area. A well-known representative is the Peano curve, shown in Fig. 1 for the first four iteration orders. Specifically, a Peano space filling curve is considered as a map from the unit interval $I = [0,1]$ to the unit area $Q = [0,1]^2$. Hence, each point of I, signified in the decimal system, is transformed into its ternary equivalent by

$$\left(0.t_1 t_2 \ldots\right)_3 = \left(t_1 3^{-1} + t_2 3^{-2} + \ldots\right)_{10}, \tag{1}$$

where the $t_j = 0,1,2$ denote ternary digits. Then, this number is mapped to a point of Q through the application of function

$$f_p\left(\left(0.t_1 t_2 t_3 \ldots\right)_3\right) = \begin{pmatrix} \left(0.t_1\left(k^{t_2} t_3\right)\left(k^{t_2+t_4} t_5\right)\ldots\right)_3 \\ \left(0.\left(k^{t_1} t_2\right)\left(k^{t_1+t_3} t_4\right)\ldots\right)_3 \end{pmatrix}, \tag{2}$$

along with operator k, defined as

$$kt_j = 2 - t_j, \tag{3}$$

with k^v the v-th iterative enforcement of k. Finally, all coordinates represented in the ternary system are transformed into their decimal counterparts.

Implementing the above algorithm and bearing in mind the fundamental properties of space compression, it is feasible to design specific antennas with a high level of compactness. The topology of the antenna studied, herein, is a top-loaded monopole, exploiting the 2nd order Peano curve to form a metallic path, as depicted in Fig. 2a. The whole structure is placed above a ground plane according to the arrangement of Fig. 2b. The device is excited via the probe of a coaxial cable connected to the center of the curve, while two cylindrical shorting posts connect the end-points of the antenna to the ground. In this framework, based on the gamma match excitation of dipoles [15], a matching network to a 50 Ω source is created, without the need of any external apparatus.

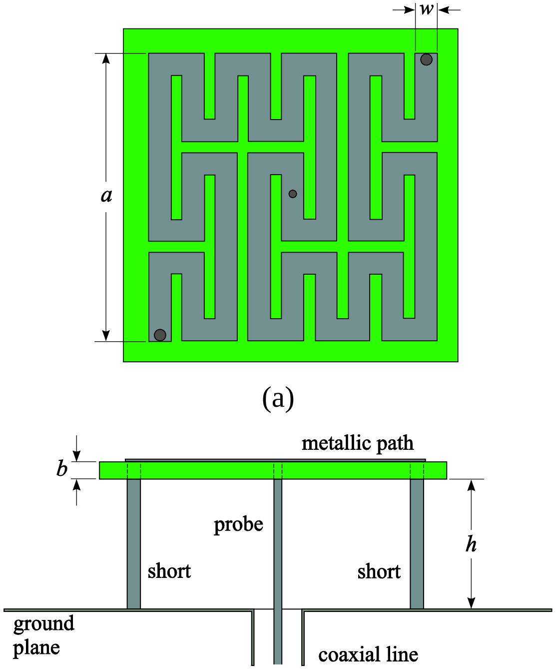

(a)

(b)

Fig. 2. Top-loaded monopole Peano antenna. (a) metallic path geometry and (b) side perspective.

The metallic path of the antenna is constrained on a 19.1 mm × 19.1 mm footprint, whereas path width w is, respectively, set to 1.49 mm and 2.11 mm for the two designs under investigation. A 1.5 mm thick substrate with a dielectric permittivity of 2.21 is selected to provide the appropriate mechanical support to the antenna. Moreover, the distance between the substrate and the ground plane is set to $h = 8.5$ mm, while the radius of the cylindrical shorting posts is $r = 0.5$ mm. For our simulations, a 3-D FDTD technique in conjunction with a 6-cell perfectly matched layer (PML) absorber for open-boundary termination [16], is developed.

In view of these structural data, a detailed parametric study is conducted regarding the substrate's height and the radius of the shorting posts. Actually, the role of these two parameters in the achievement of the correct matching and the desired behavior is deemed decisive. From the analysis, it is evident that, when *h* increases (Fig. 3a) or *r* decreases (Fig. 3b), a shift of the S_{11} parameter towards lower frequencies occurs. Also, to obtain a more general view of the antenna's operation, its surface current distribution at the frequency of 2.52 GHz is illustrated in Fig. 4, in which minimum values are observed near the center of the device.

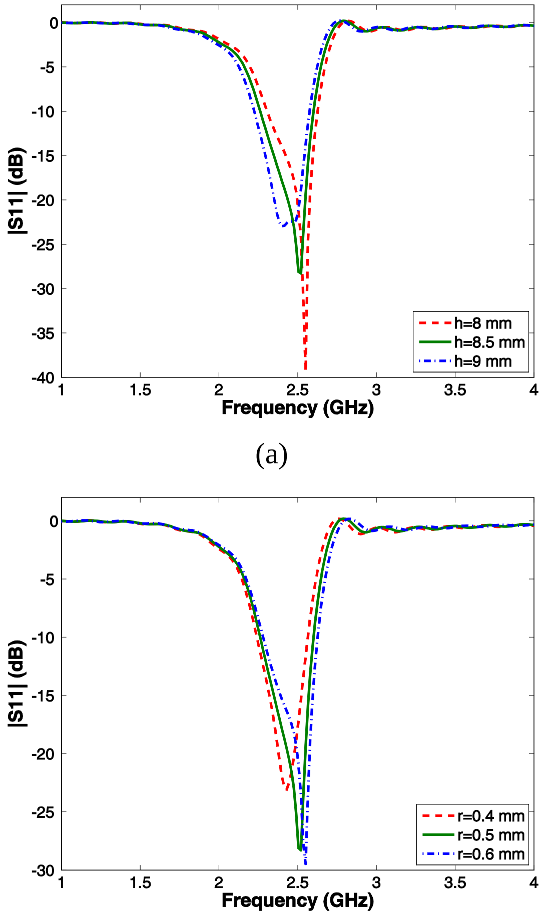

(a)

(b)

Fig. 3. Variation of the S_{11} parameter for different values of (a) the substrate's height and (b) the radius of the shorting posts.

III. COMBINED BPA CONFIGURATION

The broadband behavior of the bowtie antenna (Fig. 5a) can be exploited to circumvent the bandwidth restrictions of the conventional Peano structures. The proposed configuration according to the folded bowtie concept is shown in Fig. 5b, where modifications have been conducted only at the bowtie shaped metallic path. In this context, slope *s*, describing the tangent of the bowtie's angle, is introduced as an additional parameter to distinguish the new device from the conventional one. Here, *s* is set to 0.0035, while the width of the initial path is 1.49 mm. Therefore, the final value of *w* is 2.11 mm in order to enable comparisons with the aforementioned Peano designs.

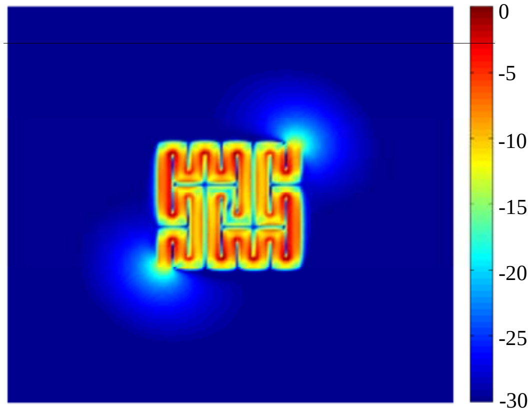

Fig. 4. Surface current distribution of the Peano antenna at the frequency of 2.52 GHz.

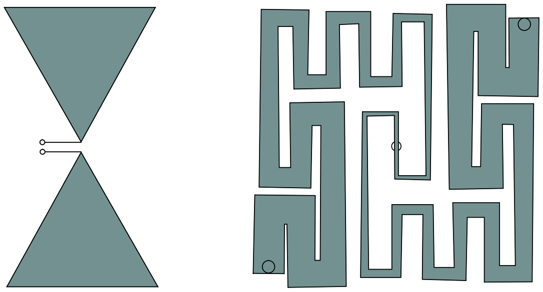

(a) (b)

Fig. 5. Geometry of (a) the bowtie antenna, and (b) the metallic path of the combined BPA.

To this goal, Fig. 6 performs a comparison between two conventional Peano designs and the combined BPA through the variation of the S_{11} parameter. Furthermore, the spectral features of the three radiating arrangements are summarized in Table 1. As deduced, in contrast to the Peano antenna with the smaller path width, the BPA presents a significantly enhanced bandwidth (7 times broader) at the resonant frequency of 10.26 GHz, whereas the fundamental resonance vanishes. In addition, a frequency shifting of roughly 1 GHz is observed for the BPA. On the other hand, when comparing the BPA with the other Peano antenna, an improved bandwidth (3 times broader) is discerned at the resonant frequency of 4.755 GHz along with a frequency shifting, while a new resonance at 10.26 GHz is revealed, achieving a bandwidth of 0.192 GHz. Thus, the novel BPA can offer an enhanced wideband performance, with the undesirable frequency shifting tackled by properly modifying its design parameters.

Proceeding with our study, the surface current distributions of the combined BPA at the extra resonances of 4.755 GHz and 10.26 GHz are shown in Fig. 7. Finally, Fig. 8 depicts the radiation patterns of all structures at certain resonant frequencies. It is apparent that minor deviations are introduced by the BPA arrangement. Nevertheless, its maximum gain is slightly decreased. Particularly, the BPA exhibits a gain of 4.4 dB at 4.755 GHz versus the 6.3 dB at 5.715 GHz of the conventional antennas (Fig. 8a). Also, a gain of 6.4 dB at 10.26 GHz in opposition to the 7.8 dB at 10.2 GHz is observed in Fig. 8b.

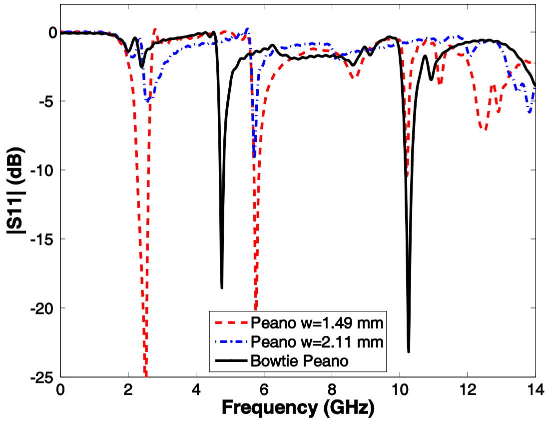

Fig. 6. Variation of the S_{11} parameter: Conventional Peano designs versus the proposed BPA.

Table 1: Bandwidth comparison (at -10 dB) of various Peano antennas for two resonances

Antenna	**Res.**	**Start (GHz)**	**End (GHz)**	**BW (GHz)**
Peano *w* = 1.49 mm	2nd	5.704	5.855	0.151
	3rd	10.192	10.220	0.028
Peano *w* = 2.11 mm	2nd	5.692	5.746	0.054
	3rd	–	–	–
Proposed BPA	2nd	4.690	4.838	0.148
	3rd	10.164	10.356	0.192

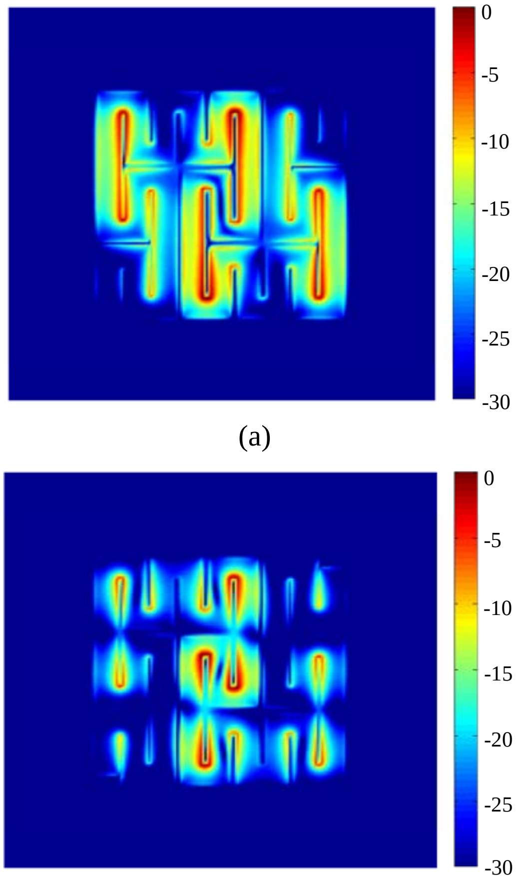

(a)

(b)

Fig. 7. Surface current distribution of the BPA configuration at (a) 4.755 GHz and (b) 10.26 GHz.

IV. ALTERNATIVE BPA DESIGN WITH A BOWTIE OUTLINE

In contrast to the radiating arrangement of the previous section, which is implemented by a bowtie shaped metallic path, the antenna designed, herein, presents a constant path width of w = 1.5 mm. However, the outline of its footprint is altered into a bowtie frame prescribed by an angle of 2φ ($\varphi = 22^{o}$), as illustrated in Fig. 9. The feed of the device remains the same, separating the structure into two sub-antennas, the end-points of which are denoted from the corners of the Peano curve at the shorting posts and the center of the coaxial probe. Note that angle 2φ introduces an asymmetry in the dimensions of the two sub-devices and hence the two parts of the metallic path have different lengths. In spite of angle 2φ and the consequent change of the footprint's shape, the area occupied is identical. So, a comparison with the conventional antenna of the same footprint can be readily performed.

Additionally, the height of the substrate measured from the ground plane is h = 16 mm, the substrate thickness is b = 1.5 mm, and its dielectric permittivity is 2.21 to achieve the proper matching.

To comprehend the role of the modification in the alternative BPA, Fig. 10 presents the impact of the substrate's height, the radius of the shorting posts, and the angle. Notice that matching as well as the desired performance is attained, while a shift towards lower frequencies is observed, as h increases or r decreases. Also, as φ decreases, the two distinct resonances get closer and tend to merge. Next, a comparison between the conventional Peano antenna and the alternative BPA design is attempted. Hence, Fig. 11 gives the variation of the S_{11} parameter and Table 2 summarizes the spectral characteristics of the resonant frequencies. From the results, the alternative BPA reveals a clear separation of the conventional Peano's first resonance into two adequately deep discrete regions. This can be mainly attributed to the asymmetry in the dimensions of the two sub-antennas. So, different path lengths lead to two distinct resonances. Also, the alternative BPA presents an enhanced bandwidth (6 and 4 times broader) at the resonant frequencies of 7.365 GHz and 8.04 GHz, respectively, in contrast to the typical Peano configuration. However, a reduced bandwidth is observed at the resonant frequencies of 1.575 GHz and 9.9 GHz. This minor discrepancy can be basically attributed to the asymmetry introduced by the alternative arrangement. Nevertheless, the majority of the resonances retain their enhanced performance. Hence, it is derived that the alternative BPA can attain an improved wideband behavior through the tuning of its design parameters.

Concerning the radiation performance of the alternative BPA, Fig. 12 displays its surface current distribution at the resonant frequency of 1.575GHz. Recalling the results of Table 2, a gain enhancement is deduced at all resonant frequencies. In addition, Fig. 13 compares the radiation patterns of a conventional Peano and the proposed an- tenna at specific resonant frequencies. Expressly, the alternative BPA attains a gain of 4.2 dB at 1.905 GHz versus the 3 dB at 1.86 GHz of the typical Peano device (Fig. 13a). Moreover, a gain of 10.2 dB at 8.04 GHz as opposed to the 7.8 dB at 8.265 GHz is detected in Fig. 13b. Finally, the shapes of the radiation patterns are not seriously modified despite the geometrical changes.

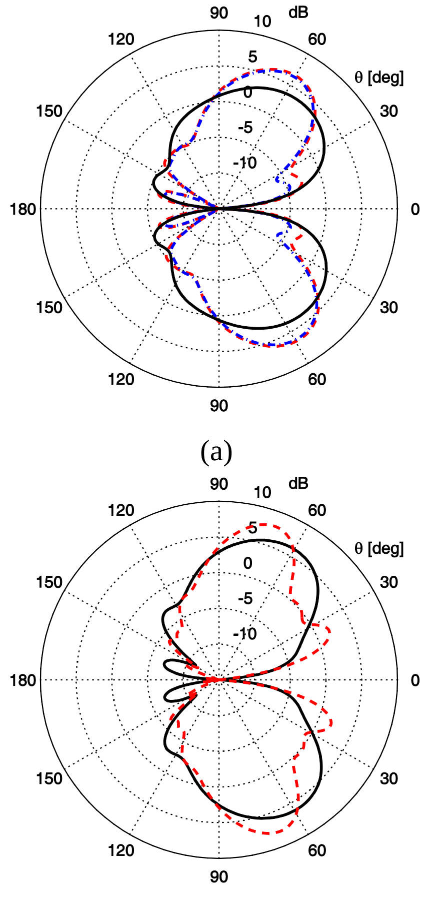

(a)

(b)

Fig. 8. Gain radiation patterns at φ = 135° of conventional Peano designs versus the combined BPA: (a) Resonances at 5.76 GHz, 5.715 GHz, 4.755 GHz (red: w = 1.49 mm, blue: w = 2.11 mm, black: BPA) and (b) resonances at 10.2 GHz, 10.26 GHz (red: w = 1.49 mm, black: BPA).

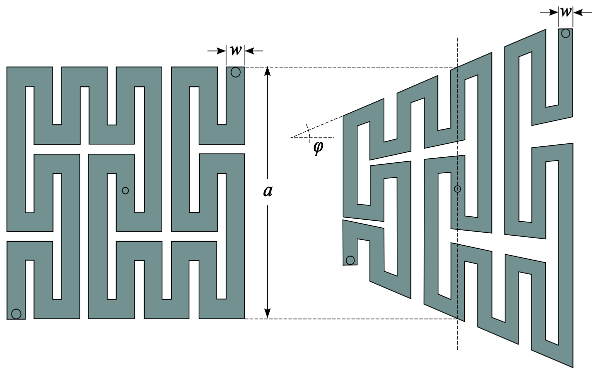

Fig. 9. Geometry of the alternative BPA design exploiting a bowtie outline.

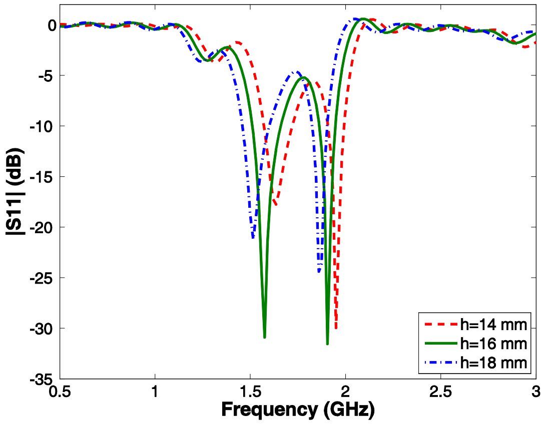

(a)

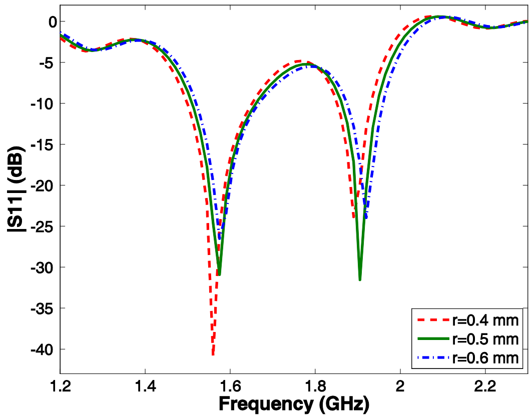

(b)

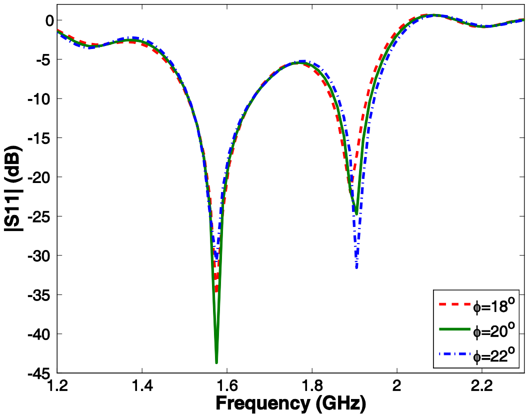

(c)

Fig. 10. Variation of the S_{11} parameter for different values of (a) the substrate's height, (b) the radius of the shorting posts, and (c) angle φ.

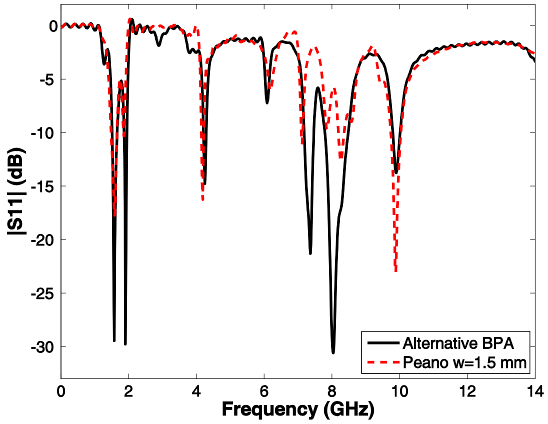

Fig. 11. Variation of the S_{11} parameter: Conventional Peano design versus the alternative BPA.

Table 2: Radiation and spectral comparison (at -10 dB) of the Peano antenna and the alternative BPA

Antenna	**Resonance**	**1st**	**2nd**	**3rd**	**4th**	**5th**	**6th**	**7th**
Peano *w* = 1.5 mm	Frequency (GHz)	1.590	1.860	4.185	6.180	7.125	8.265	9.885
	Gain (dB)	3.5	3.0	5.1	7.9	8.8	7.8	7.5
	Bandwidth (GHz)	0.175	0.017	0.070	–	0.046	0.171	0.299
Alternative BPA	Frequency (GHz)	1.575	1.905	4.245	6.090	7.365	8.040	9.900
	Gain (dB)	4.6	4.2	6.8	8.4	9.9	10.2	7.8
	Bandwidth (GHz)	0.150	0.080	0.081	–	0.285	0.690	0.218

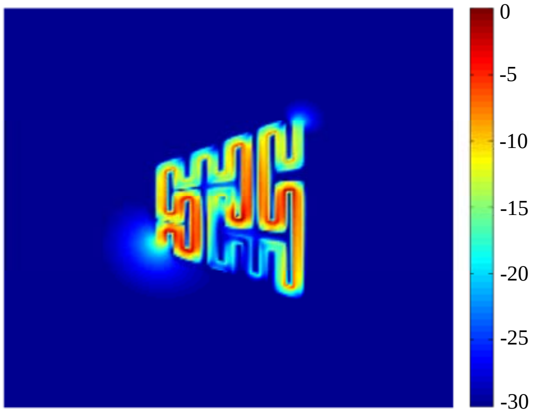

Fig. 12. Surface current distribution of the alternative BPA at 1.575 GHz.

V. CONCLUSION

A new family of combined bowtie-Peano antennas with highly compact dimensions has been presented and comprehensively explored in this paper. The overall analysis verified a considerably enhanced operational bandwidth at certain resonances. Furthermore, a slight reduction in gain levels unveils a trade-off between the gain and the broadband behavior of the combined BPA. Nonetheless for the alternative BPA, a gain improvement at each resonance has been achieved, indicating that the proposed devices could be successfully incorporated in an assortment of modern miniaturized microwave implementations.

ACKNOWLEDGMENT

This work was supported by the National Scolarships Foundation of Greece (IKY), under Grant No. 5282.

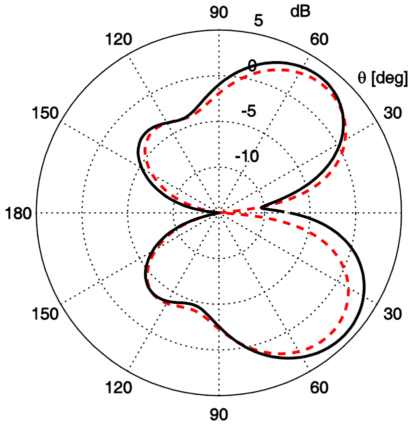

(a)

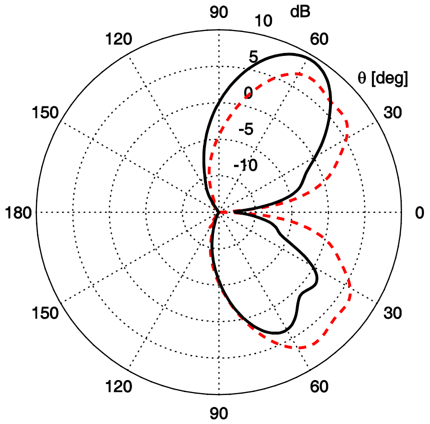

(b)

Fig. 13. Gain radiation patterns at $\varphi = 135^{o}$ of conventional Peano design versus the alternative BPA: (a) Resonances at 1.86 GHz, 1.905 GHz, (red: w = 1.5 mm, black: alternative BPA), and (b) resonances at 8.265 GHz, 8.04 GHz (red: w = 1.5 mm, black: alternative BPA).

REFERENCES

[1] H. Sagan, *Space-Filling Curves*, Springer-Verlag, 1993.

[2] J. Gonzalez-Arbesu, S. Blanch, and J. Romeu, “Are Space-Filling Curves Efficient Small Antennas?,” *IEEE Antennas Wireless Propag. Lett.*, vol. 2, pp. 147-150, 2003.

[3] R. Hasse, V. Demir, W. Hunsicker, D. Kajfez, and A. Elsherbeni, “Design and Analysis of Partitioned Square Loop Antennas,” *Applied Computational Electromagnetic Society (ACES) Journal*, vol. 23, no. 1, pp. 53-61, 2008.

[4] C. de J. van Coevorden, A. Bretones, M. Pantoja, S. Garcıa, and A. Monorchio, “A New Implementation of the Hybrid Taguchi GA: Application to the Design of a Miniaturized Log-Periodic Thin-Wire Antenna,” *Applied Computational Electromagnetic Society (ACES) Journal*, vol. 24, no. 1, pp. 21-31, 2009.

[5] T. Spence, D. Werner, and J. Carvajal, “Modular Broadband Phased-Arrays Based on a Nonuniform Distribution of Elements Along the Peano-Gosper Space-Filling Curve,” *IEEE Trans. Antennas Propag.*, vol. 58, no. 2, pp. 600-604, 2010.

[6] S. Best, “A Comparison of the Resonant Properties of Small Space-Filling Fractal Antennas,” *IEEE Antennas Wireless Propag. Lett.*, vol. 2, pp. 197-200, 2003.

[7] J. McVay, A. Hoorfar, and N. Engheta, “Peano High Impedance Surfaces,” *Radio Sci.*, vol. 40, pp. 1-9, 2005.

[8] H. Oraizi and S. Hedayati, “Miniaturized UWB Monopole Microstrip Antenna Design by the

Combination of Giusepe Peano and Sierpinski Carpet Fractals," *IEEE Antennas Wireless Propag. Lett.*, vol. 10, pp. 67-70, 2011.

[9] S.-H. Wi, J.-M. Kim, and J.-G. Yook, "Microstrip-Fed Bowtie-Shaped Meander Slot Antenna with Compact and Broadband Characteristics," *Microw. Opt. Technol. Lett.*, vol. 45, no. 1, pp. 88-90, 2005.

[10] J.-F. Li, B.-H. Sun, H.-J. Zhou, and Q.-Z. Liu, "Miniaturized Circularly-Polarized Antenna using Tapered Meander-Line Structure," *PIERS*, vol. 78, pp. 321-388, 2008.

[11] J. William and R. Nakkeeran, "A New UWB Slot Antenna with Rejection of WiMax and WLAN Bands," *Applied Computational Electromagnetic Society (ACES) Journal*, vol. 25, no. 9, pp. 787-793, 2010.

[12] E. El-Khouly, H. Ghali, and S. Khamis, "High Directivity Antenna using a Modified Peano Space-Filling Curve," *IEEE Antennas Wireless Propag. Lett.*, vol. 6, pp. 405-407, 2007.

[13] J. McVay, A. Hoorfar, and N. Engheta, "Space-Filling Curve Radio Frequency Identification Tags," *Applied Computational Electromagnetic Society (ACES) Journal*, vol. 25, no. 6, pp. 517-529, 2010.

[14] T. Terada, K. Ide, K. Iwata, and T. Fukusako, "Design of a Small, Low-Profile Print Antenna using a Peano Line," *Microw. Opt. Technol. Lett.*, vol. 51, no. 8, pp. 1833-1838, 2009.

[15] C. A. Balanis, *Modern Antenna Handbook*, Wiley-Blackwell, 2008.

[16] A. Taflove and S. Hagness, *Computational Electrodynamics: The Finite-Difference Time-Domain Method*, Artech House, 2005.

Ioannis I. Papadopoulos-Keli-dis received the Diploma degree in Electrical and Computer Engineering from the Aristotle University of Thessaloniki, Thessaloniki, Greece, in 2010. His research interests include computational electromagnetics and modern antenna design.

Antonios X. Lalas received the Diploma degree in Electrical and Computer Engineering from the Aristotle University of Thessaloniki, Thessaloniki, Greece, in 2006, where he is currently pursuing his Ph.D. degree. His research interests include computational electromagnetics and antenna design as well as the analysis and modeling of MEMS structures, with an emphasis on EBG and metamaterial applications.

Nikolaos V. Kantartzis received the Diploma and Ph.D. degrees from the Department of Electrical and Computer Engineering, Aristotle University of Thessaloniki, Greece, in 1994 and 1999, respectively. In 2001, he joined the same department, as a Postdoctoral Research Fellow, where, currently, he serves as an Assistant Professor. He has authored/co-authored 3 books, more than 55 refereed journal and over 70 conference papers. His main research interests include computational electromagnetics, contemporary antenna design, EMC modeling, higher-order time- and frequency-domain methods, metamaterials, and advanced microwave structures. Dr. Kantartzis is a member of diverse scientific societies and associations.

Theodoros D. Tsiboukis received the Diploma degree in Electrical and Mechanical Engineering from the National Technical University of Athens, Athens, Greece, in 1971, and the Doctor Eng. Degree from the Aristotle University of Thessaloniki (AUTH), Thessaloniki, Greece, in 1981. From 1981 to 1982, he was with the Electrical Engineering Department, University of Southampton, Southampton, U.K., as a Senior Research Fellow. Since 1982, he has been with the Department of Electrical and Computer Engineering, AUTH, where he is currently a Professor. He has served in numerous administrative positions and as a chairman of many conference organizing committees. He is the author of 8 books and over 250 refereed journal and conference papers. His research areas, primarily, focus on electromagnetic field analysis by energy methods, computational (frequency- and time-domain) electromagnetics, metamaterials and double-negative media, photonic crystals, inverse and EMC problems. Prof. Tsiboukis is a member of various societies, chambers, associations, and institutions, and has been the recipient of several awards and distinctions.

A Finite Difference Polar-Cartesian Grid Approach for Mode Computation in Rounded-End Waveguides

Alessandro Fanti and Giuseppe Mazzarella

Department of Electrical and Electronic Engineering
University of Cagliari, 09123, Piazza d'Armi, Cagliari, Italy
alessandro.fanti@diee.unica.it, mazzarella@diee.unica.it

***Abstract* —** A finite-difference technique to compute Eigenvalues and mode distribution of non standard waveguide (and aperture) is presented. It is based on a mixed mesh (Cartesian-polar) to avoid staircase discretization of curved edges, and is able to give accuracy comparable to FEM and FIT techniques with a reduced computational burden.

***Index Terms* —** Eigenvalue, finite-difference, Helmholtz equation, waveguide modes.

I. INTRODUCTION

In finite difference time domain (FDTD) analysis of waveguide components, the knowledge of the modal expansion can reduce significantly the computation time, since it is possible to model each homogeneous waveguide trunk as a (small) set of 1D-FDTD problems [1]. This approach, however, requires the waveguide mode functions be known, either analytically, or numerically but on a grid matched to the 3D FDTD grid used in the inhomogeneous regions.

The same knowledge of mode function is useful in the analysis of waveguide junction using mode matching [2-6], solution of waveguide problems with sources [7], and the method of moments (MOM) analysis of thick-walled waveguide slot for linear [8] and circular polarization [9] and for apertures [10].

Apart from some simple geometries, mode computation cannot be done in closed forms, so that suitable numerical techniques must be used. Among them, finite difference (FD) techniques [11], despite of their long history, are still very popular both for their simplicity and computational effectiveness.

The most popular FD approach is based on the use of a standard four-point FD approximation [12] of the Laplace operator. But it requires a rectangular discretization grid, and therefore a boundary with all sides parallel to the rectangular axes. As a consequence, many geometries cannot be dealt with exactly with this approach, requiring a staircase approximation of the boundaries.

The aim of this paper is to present a FD technique for the computation of modes and eigenvalues of a waveguide whose boundary consists of segments and circular arcs, taking exactly into account the curved boundary of the waveguide and with no loss of accuracy. Among those waveguides, rounded-end rectangular waveguides (Fig. 1) are the most interesting, and will be detailed here for the technique assessment. Our approach, which uses a polar grid for the curved region and a rectangular grid for the straight ones, is not limited to rounded-end rectangular waveguides, but can be straight forwardly extended to many other geometries.

Fig. 1. Rounded-end rectangular waveguide.

This approach can be used for circular waveguides too, and the following case starts with a two-fold purpose: first, to describe the main part of our approach in a simpler way; second, to set up a test-bench to assess our approach. As a matter of fact, we will compare the results of our approach on non-standard waveguides with a commercial, general-purpose, software. The accuracy of this

Submitted On: May 31, 2011
Accepted On: October 8, 2011

software, compared to our approach, will be tested in the circular case, where the exact solution is known.

The comparison presented shows that the technique proposed here gives results comparable to those obtained with the finite element method (FEM) and the finite integration technique (FIT) [13], but with a lower computational cost.

II. DESCRIPTION OF THE TECHNIQUE

A. Technique framework

Let us consider a generic waveguide. TE modes can be found [7] from a suitable scalar eigenfunction φ, solution of the Helmholtz equation:

$$\nabla_t^2 \varphi + k_t^2 \varphi = 0 , \tag{1}$$

with the boundary condition (BC)

$$\frac{\partial \varphi}{\partial n} = 0 , \tag{2}$$

at the boundary of the waveguide. In the FD approach both the equation (1) and the BC (2) are replaced by a discretised version, i.e., replacing derivatives with finite approximations. This transform (1) into a matrix eigenvalue problem, whose eigenvectors contain the samples of φ at the discretization nodes. The matrix is sparse, so a very effective computation is possible.

If the waveguide boundary consists of straight lines, parallel to the coordinate axes, the FD method can be applied on a Cartesian grid [12]. This grid defines also a partition of the waveguide surface into rectangular cells, which completely fill the waveguide section. For every other waveguide, the section cannot be exactly partitioned using rectangular cells and this leads to numerical errors (since the eigenvalue problem is quite ill – conditioned [14]).

In order to get a high accuracy, the waveguide surface must be discretized maintaining also the correct geometry of the boundary. So a different discretization scheme should be used, which matches exactly the waveguide boundary. Therefore, the discretization nodes must be at the intersections of a suitable framework, in which the waveguide boundary is a coordinate curve. In this way, the waveguide section is exactly partitioned into a discretization cell.

The discretized equations can be obtained in two ways. The standard approach is to sum a Taylor expansion of the potentials [12]. Alternatively, we can integrate (1) over a discretization cell [11]

$$\int \nabla_t^2 \varphi dS = -k_t^2 \int \varphi dS . \tag{3}$$

Use of the Gauss theorem then gives:

$$\int_{\Gamma_F} \nabla_t^2 \varphi \cdot i_n dl = -k_t^2 \int_{S_F} \varphi dS , \tag{4}$$

i.e.

$$\int_{\Gamma_F} \frac{\partial \varphi}{\partial n} \cdot dl = -k_t^2 \varphi , \tag{5}$$

where Γ_F is the cell boundary, S_F is the cell surface and φ is evaluated at the discretization node in the right hand side. The left hand side of (5) is then divided into four (or more) sides, along the coordinate curves, and the normal derivative is evaluated in finite terms.

The two approaches apply in non-overlapping sets of cases, but when both can be used, the results are the same, as we will show later.

Since both discretizations (either the standard FD and that based on (5)) can easily include the BC (2), the resulting FD formulation to equivalent to the complete eigenvalue problem (1,2).

B. Circular waveguide

In order to explain the difference with the standard FD, and to assess our approach, we start considering a circular waveguide (see Fig. 2), using as grid lines the coordinate lines of a polar framework. We assume a regular spacing on the coordinate lines, with step Δr, $\Delta \vartheta$, and let $\varphi_{nq} = \varphi\left(n\Delta r, q\Delta \vartheta\right)$.

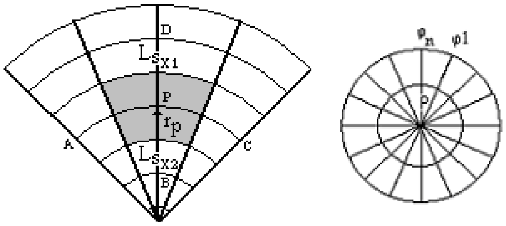

Fig. 2. A section of circular waveguide.

Let P the point of coordinates $\left(n\Delta r, q\Delta \vartheta\right)$, and consider the four nearby points A, B, C, and D, as shown in Fig. 2. For the left hand side of (5), we get

$$\frac{1}{S_F}\cdot\left[\frac{(\varphi_D-\varphi_P)}{\Delta r}\cdot L_{Sx1}+\frac{(\varphi_B-\varphi_P)}{\Delta r}\cdot L_{Sx2}+\right. \qquad , \qquad (6)$$
$$\left.+\frac{(\varphi_A-\varphi_P)}{\Delta\vartheta\cdot r_p}\cdot\Delta r+\frac{(\varphi_C-\varphi_P)}{\Delta\vartheta\cdot r_p}\cdot\Delta r\right]$$

where $S_F = r_P\cdot\Delta r\cdot\Delta\vartheta,\ L_{SX1}=\left(r_P+\frac{\Delta r}{2}\right)\cdot\Delta\vartheta$ and

$L_{SX2}=\left(r_P-\frac{\Delta r}{2}\right)\cdot\Delta\vartheta$.

Replacing and collecting the term, we get the discretized form of (1) as:

$$\frac{1}{r_p^2(\Delta\vartheta)^2}\cdot\varphi_A+\left(\frac{1}{2r_p\Delta r}+\frac{1}{(\Delta r)^2}\right)\cdot\varphi_D+$$
$$+\frac{1}{r_p^2(\Delta\vartheta)^2}\cdot\varphi_C+\left(\frac{1}{(\Delta r)^2}-\frac{1}{2r_p\Delta r}\right)\cdot\varphi_B+ \qquad (7)$$
$$-\left(\frac{2}{(\Delta r)^2}+\frac{2}{r_p^2(\Delta\vartheta)^2}\right)\cdot\varphi_P\cong-k_t^2\varphi_p^2$$

This expression can be used for all internal points, except the circle centre.

It is worth noting that (8) can be obtained also starting from the Helmholtz equation in polar coordinates.

$$\left[\frac{1}{r_p^2}\cdot\frac{\partial^2\varphi}{\partial\vartheta^2}+\frac{1}{r_p}\cdot\frac{\partial\varphi}{\partial r}+\frac{\partial^2\varphi}{\partial r^2}\right]=-k_t^2\varphi\,, \qquad (8)$$

and using a Taylor approximation.

$$\varphi_B=\varphi_P+\left.\frac{\partial\varphi}{\partial r}\right|_P\cdot(-\Delta r)+\frac{1}{2}\left.\frac{\partial^2\varphi}{\partial r^2}\right|_P\cdot(-\Delta r)^2\,, \quad (9)$$

$$\varphi_D=\varphi_P+\left.\frac{\partial\varphi}{\partial r}\right|_P\cdot(+\Delta r)+\frac{1}{2}\left.\frac{\partial^2\varphi}{\partial r^2}\right|_P\cdot(+\Delta r)^2\,. \quad (10)$$

Adding and subtracting the last two equations we find:

$$\left.\frac{\partial^2\varphi}{\partial r^2}\right|_P=\frac{1}{(\Delta r)^2}\cdot(\varphi_B+\varphi_D-2\varphi_P)\,, \qquad (11)$$

and

$$\left.\frac{\partial\varphi}{\partial r}\right|_P=\frac{\phi_D-\varphi_B}{2\cdot\Delta r}\,. \qquad (12)$$

Likely in ϑ direction

$$\left.\frac{\partial^2\varphi}{\partial\vartheta^2}\right|_P=\frac{1}{(\Delta\vartheta)^2}\cdot(\varphi_A+\varphi_C-2\varphi_P)\,. \qquad (13)$$

Collecting all those equation in (8) we get (7). It remains to consider the last point, i.e. the centre of the circle. In this point, it is not possible to use a Taylor expression since it is a point of singularity. So we are forced to use (5).

The left hand side of (5) can be expanded as (see Fig. 2)

$$\left(\frac{1}{\pi\cdot\left(\frac{\Delta r}{2}\right)^2}\right)\cdot\sum_{q=1}^{N}\frac{(\varphi_q-\varphi_P)}{\Delta r}\cdot\frac{\Delta r}{2}\cdot\Delta\vartheta\,, \qquad (14)$$

and therefore the discretized form of the equation (1) is:

$$\left(\frac{4}{\pi\cdot\Delta r^2}\right)\cdot\left(\sum_{q=1}^{N}\varphi_q\frac{\Delta\vartheta}{2}-N\frac{\Delta\vartheta}{2}\varphi_P\right)\cong-k_t^2\varphi_P\,. \quad (15)$$

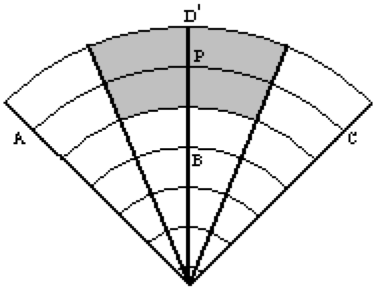

Fig. 3. Boundary point of circular waveguide.

On the boundary points in Fig. 3, for TE modes we can replace (9) by a first-order approximation $\varphi_P=\varphi_D+\left.\frac{\partial\varphi}{\partial r}\right|_D\cdot\left(\frac{\Delta r}{2}\right)$ and since the BC is $\left.\frac{\partial\varphi}{\partial r}\right|_D=0$, we get $\varphi_P=\varphi_D$.

As a consequence (11) becomes:

$$\frac{\partial^2\varphi}{\partial r^2}\Big|_P=\frac{1}{\Delta r^2}\cdot(\varphi_B-\varphi_P)\,, \qquad (16)$$

and (7) is replaced by:

$$\begin{aligned}&\frac{1}{r_p^2\Delta\vartheta^2}\cdot\varphi_A+\frac{1}{r_p^2\Delta\vartheta^2}\cdot\varphi_C+\\&+\left(\frac{1}{\Delta r^2}-\frac{1}{2r_p\Delta r}\right)\cdot\varphi_B+\\&-\left(\frac{1}{\Delta r^2}-\frac{1}{2r_p\Delta r}+\frac{2}{r_p^2\Delta\vartheta^2}\right)\cdot\varphi_P\cong -k_t^2\varphi_P\end{aligned}\quad . \qquad (17)$$

C. Rounded-end waveguide

Now consider the section of a rounded-end waveguide (see Fig. 4). The section can be divided into three regions. In the external ones, we use a polar framework; while in the central one, we can use the standard Cartesian framework, as in Fig. 4.

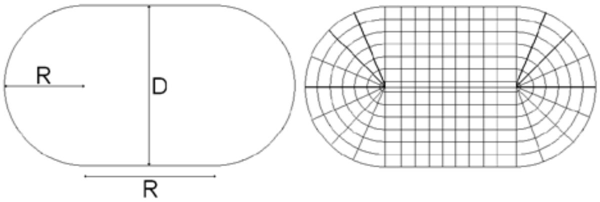

Fig. 4. A mixed mesh (Cartesian-polar) of non-standard waveguide and its dimensions.

In the Cartesian framework, we assume a regular spacing on the coordinate lines, with step $\Delta x, \Delta y$ (see Fig. 4).

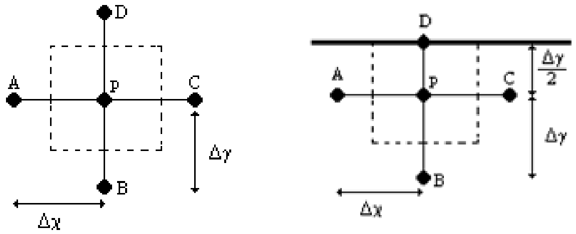

(a) (b)

Fig. 5. (a) Internal point , (b) boundary point .

For each internal point, we can use the standard expression of the Laplacian obtained by the Taylor expansion [10]:

$$\begin{aligned}&\nabla_t^2\varphi_p=\frac{\varphi_A}{\Delta x^2}+\frac{\varphi_C}{\Delta x^2}+\frac{\varphi_B}{\Delta y^2}+\frac{\varphi_D}{\Delta y^2}+\\&+\left(\frac{2}{\Delta x^2}+\frac{2}{\Delta y^2}\right)\varphi_P\end{aligned}\quad , \qquad (18)$$

and replace (1) by the discretized form:

$$\begin{aligned}&\frac{\varphi_{i,j-1}}{\Delta x^2}+\frac{\varphi_{i,j+1}}{\Delta x^2}+\frac{\varphi_{i-1,j}}{\Delta y^2}+\frac{\varphi_{i+1,j}}{\Delta y^2}+\\&+\left(\frac{2}{\Delta x^2}+\frac{2}{\Delta y^2}\right)\varphi_{i,j}=-k_t^2\varphi_{i,j}\end{aligned}\quad . \qquad (19)$$

Equation (19) cannot be used for boundary points, where BC (2) must be enforced. For a boundary point, using 3 nearby points, A,B,C, in Fig. 5b, we get:

$$\begin{aligned}&\frac{\varphi_A}{\Delta x^2}+\frac{\varphi_C}{\Delta x^2}+\frac{\varphi_B}{\Delta y^2}+\left(\frac{2}{\Delta x^2}+\frac{1}{\Delta y^2}\right)\varphi_P=\\&-k_t^2\varphi_P\end{aligned}\quad , \qquad (20)$$

and analogously one can do the same to (17). In the polar regions, we use the expression (7) and (17), so it remains to analyze the border between the polar and the Cartesian regions, Fig. 6. Since the grid geometry here is not a regular one, a new approximation of the Laplacian operator must be used, tailored to the geometry at hand. We propose here a general approach to derive such approximations in unusual geometries, which can be easily extended to discretize other differential operators.

For each point (except the centre), let us number with 0 the sampling point, and with i (i = 1, . . . , 5) its neighbouring points as in Fig. 6a. The discretized form of $\nabla_t^2\varphi$ can always be written as:

$$\nabla_t^2\phi=\frac{\partial^2\phi}{\partial x^2}+\frac{\partial^2\phi}{\partial y^2}\cong\sum_i A_i\left(\varphi_i-\varphi_0\right). \qquad (21)$$

Each difference in (21) can be expressed as a Taylor series:

$$\begin{aligned}\varphi_i-\varphi_0=&\left.\frac{\partial\varphi}{\partial x}\right|_0\cdot\Delta x_i+\left.\frac{\partial\varphi}{\partial y}\right|_0\cdot\Delta y_i+\\&+\frac{1}{2}\left.\frac{\partial^2\varphi}{\partial x^2}\right|_0\cdot\Delta x_i^{\,2}+\frac{1}{2}\left.\frac{\partial^2\varphi}{\partial y^2}\right|_0\cdot\Delta y_i^{\,2}+\\&+\left.\frac{\partial^2\varphi}{\partial x\partial y}\right|_0\cdot\Delta x_i\cdot\Delta y_i\end{aligned}\quad , \qquad (22)$$

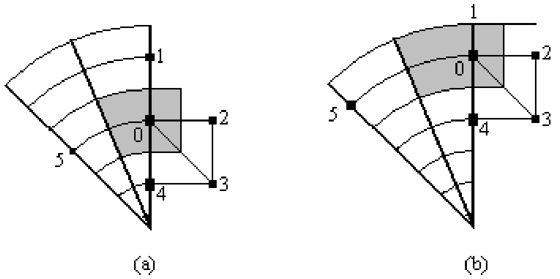

Fig. 6. (a) Point between polar and Cartesian framework. (b) Boundary point between polar and Cartesian framework.

where all derivatives of φ are computed at the sampling point, and $(\Delta x_i, \Delta y_i)$ is the position of the i–th point w.r.t point 0.

Using (21), the right hand side of (22) becomes:

$$B_1 \frac{\partial \varphi}{\partial x} + B_2 \frac{\partial \varphi}{\partial y} + B_3 \frac{\partial^2 \varphi}{\partial x^2} + B_4 \frac{\partial^2 \varphi}{\partial y^2} + B_5 \frac{\partial^2 \varphi}{\partial x \partial y} \text{,(23)}$$

where B_i in (23) are linear combination of the unknown coefficient A_i .

$$\begin{aligned}
B_1 &= A_1\Delta x_1 + A_2\Delta x_2 + A_3\Delta x_3 + A_4\Delta x_4 + A_5\Delta x_5 \\
B_2 &= A_1\Delta y_1 + A_2\Delta y_2 + A_3\Delta y_3 + A_4\Delta y_4 + A_5\Delta y_5 \\
B_3 &= A_1\Delta x_1^2 + A_2\Delta x_2^2 + A_3\Delta x_3^2 + A_4\Delta x_4^2 + A_5\Delta x_5^2 \\
B_4 &= A_1\Delta y_1^2 + A_2\Delta y_2^2 + A_3\Delta y_3^2 + A_4\Delta y_4^2 + A_5\Delta y_5^2 \\
B_5 &= A_1\Delta x_1\Delta y_1 + A_2\Delta x_2\Delta y_2 + A_3\Delta x_3\Delta y_3 + \\
&+ A_4\Delta x_4\Delta y_4 + A_5\Delta x_5\Delta y_5
\end{aligned} \text{.(24)}$$

Equation (23) is a second order approximation of the Laplace operator if

$$B_1 = B_2 = B_5 = 0 \qquad B_3 = B_4 = 1, \quad (24)$$

which is a linear system in the A_i . Its solution gives the required coefficient of (2).

For a boundary point see Fig. 6b, boundary condition (2) can be expressed as:

$$\alpha_1 \left.\frac{\partial \varphi}{\partial x}\right|_1 + \alpha_2 \left.\frac{\partial \varphi}{\partial y}\right|_1 = 0\,, \qquad (25)$$

where α_1, α_2 are the components of a unit vector normal to the boundary, (25) can be used to replace equations $B_1 = B_2 = 0$ with a single one, to compensate for the absence of one unknown (see Fig. 6b).

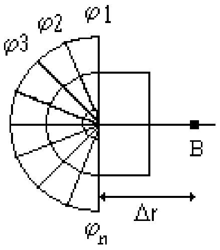

Fig. 7. Centre point between polar and Cartesian framework

For the centre of the circle, see Fig. 7, we still use (5) to get:

$$\left(\frac{8}{\pi \Delta r^2}\right) \cdot \sum_{q=1}^{N} \frac{\left(\varphi_q - \varphi_P\right)}{\Delta r} \cdot \frac{\Delta r}{2} \cdot \Delta \vartheta + \\
+ \left(\frac{2}{\Delta r^2}\right) \cdot \left(\frac{\left(\varphi_1 + \varphi_N\right)}{2} + \varphi_B - 2\varphi_P \right) = -k_t^2 \varphi_P \text{.(26)}$$

Putting together all equations, we get a matrix eigenvalue problem [14] whose solution gives the required waveguide modes.

III. NUMERICAL EXPERIMENTS

The discretized eigenvalues problem obtained in the last section must be solved by a numerical routine. As a matter of fact, a highly sparse matrix is obtained, so that the sparse matrix routines of Matlab have been used. We have first compared the first few TE eigenvalues for a circular waveguide with analytical results and with a FIT simulation performed with CST.

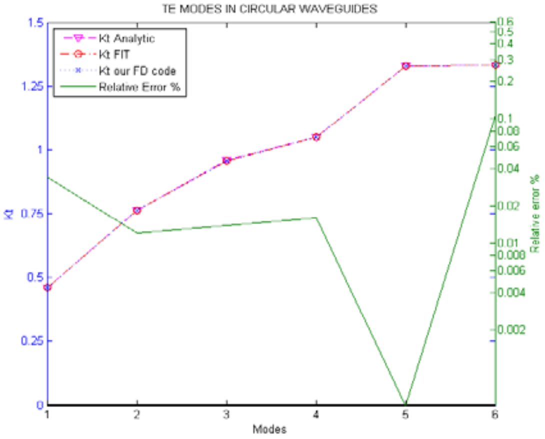

Fig. 8. Comparison between our FD code and analytic results and FIT(CST) results for TE modes in circular wave guide with r=4 mm Δr =0.0792 mm and ϑ =1°.

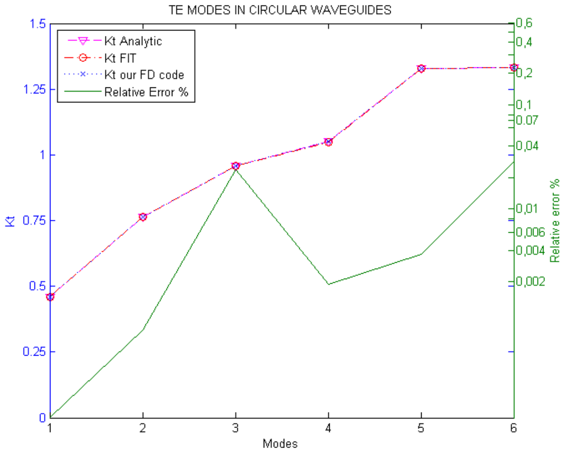

Fig. 9. Comparison between our FD code and analytic results and FIT(CST) results for TE modes in circular wave guide with r=4 mm Δr =0.0792 mm and $\Delta\vartheta$=0,5°.

We have made several tests by varying the steps (Δr, $\Delta\vartheta$). The results of Figs. 8 and 9 show that our technique has a very low error, as long as the steps are small.

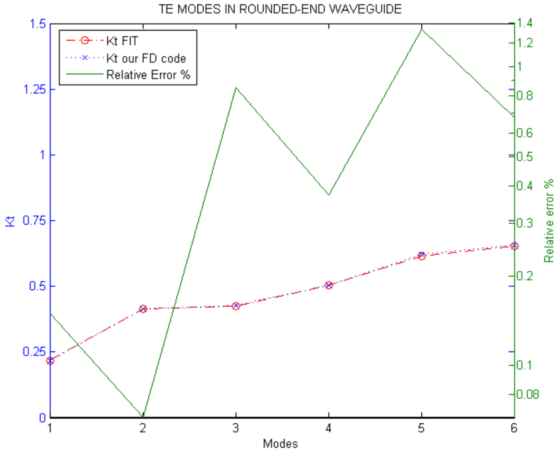

Fig. 10. Comparison between our FD code and FIT (CST) results for TE modes in rounded-end wave guide with $\Delta x = \Delta y = \Delta r = 0,1569$ mm D=B=8 mm and ϑ=1°.

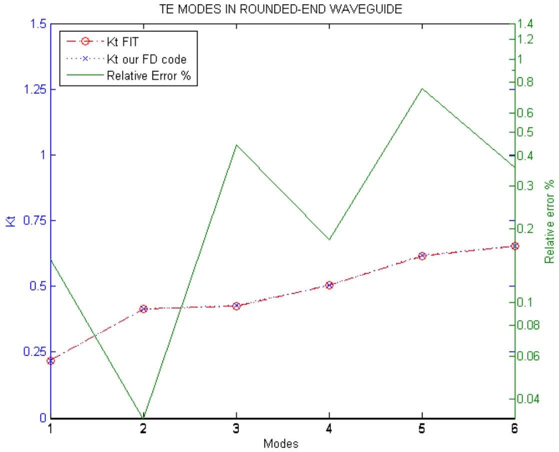

Fig. 11. Comparison between our FD code and FIT (CST) results for TE modes in rounded-end wave guide with $\Delta x = \Delta y = \Delta r = 0,0792$ mm D=B=8 mm and $\Delta\vartheta$=1°.

When compared to CST, our results are better, and can be obtained in a fraction of the computational time required by the former. However, the comparison of FIT and analytical results show that the CST is quite accurate, too, and can be used to test our approach for the rounded-end waveguide.

To assess our FD code in this case, we have evaluated a few TE modes, for different structures (see Figs. 10 - 15). Figures 10 – 15 show the comparison between our results and CST ones.

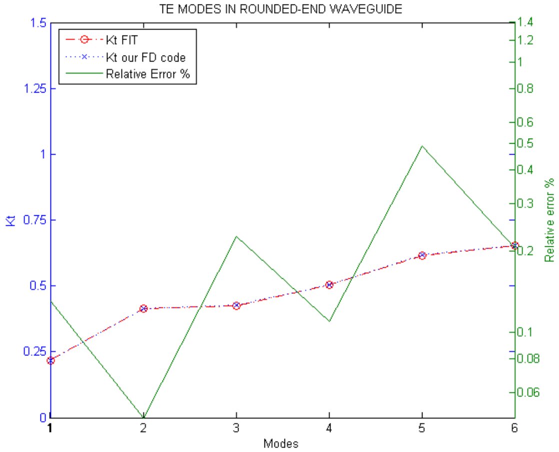

Fig. 12. Comparison between our FD code and FIT (CST) results for TE modes in rounded-end wave guide with $\Delta x = \Delta y = \Delta r = 0,03980$ mm D=B=8 mm and ϑ=1°.

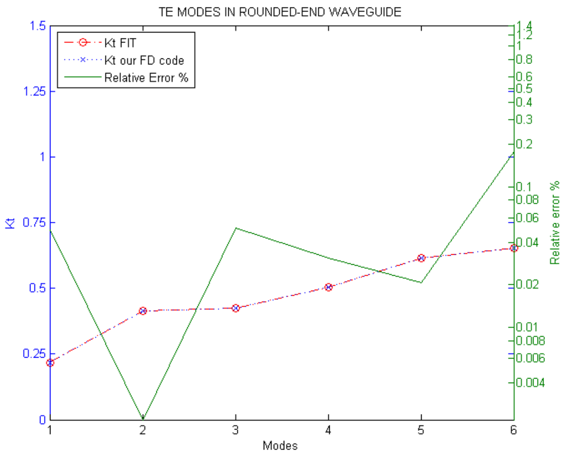

Fig. 13. Comparison between our FD code and FIT (CST) results for TE modes in rounded-end wave guide with $\Delta x = \Delta y = \Delta r = 0{,}01995$ mm D=B=8 mm and ϑ=1°.

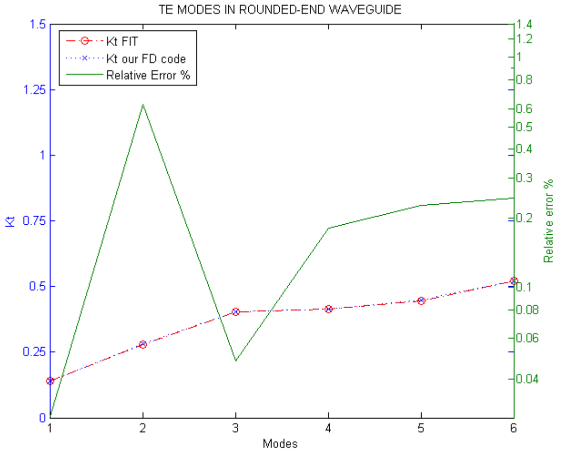

Fig. 14. Comparison between our FD code and FIT (CST) results for TE modes in rounded-end wave guide with $\Delta x = \Delta y = \Delta r =$ 0,0792 mm D=8 mm B=16 mm and ϑ=1°.

The results show that our FD approach allows a high accuracy, when the discretization step is suitably chosen. But even a quite large area, such as in Table 3, allows a quite accurate mode evaluation.

VI. CONCLUSION

A FD approach to the computation of the TE modes of the waveguide using a mixed polar-Cartesian grid has been described. The typical sparse matrix obtained by the FD allows an effective computation of the eigenvalues, with a good accuracy, as shown by our tests. The described approach can be extended to waveguides with more general geometries, as long as the guide boundary is a coordinate curve of a suitable framework.

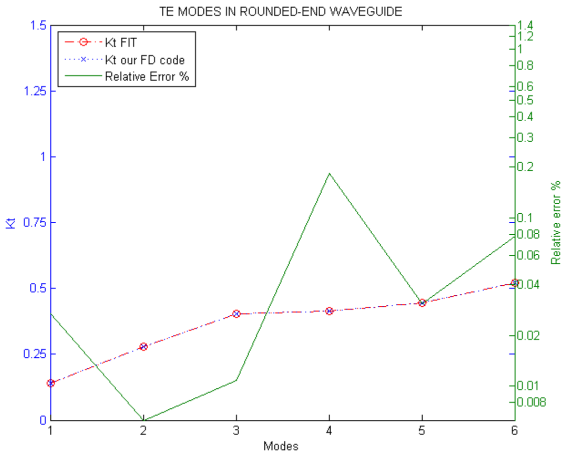

Fig. 15. Comparison between our FD code and FIT (CST) results for TE modes in rounded-end wave guide with $\Delta x = \Delta y = \Delta r =$ 0,03980 mm D=8 mm B=16 mm and ϑ=1°.

REFERENCES

[1] F. Alimenti, P. Mezzanotte, L. Roselli, and R. Sorrentino, “Efficient Analysis of Waveguide Components by FDTD Combined with Time Domain Modal Expansion,” *MGWL*, vol. 5, pp. 351-353, October 1995.

[2] A. Wexler, “Solution of Waveguide Discontinuities by Modal Analysis,” *IEEE Trans. Microwave Theory and Techniques*, vol. MTT-15, pp. 508-517, September 1967.

[3] A. Pellegrini, S. Bertini, A. Monorchio, and G. Manara, “A Mode Matching - Finite Element - Spectral Decomposition Approach for the Analysis of Large Finite Arrays of Horn Antennas,” *Applied Computational Electromagnetic Society (ACES) Journal*, vol. 24, no. 2, pp. 233–240, April 2009.

[4] K. L. Chan and S. R. Judah, “Mode-Matching Analysis of a Waveguide Junction Formed by a Circular and a Larger Elliptic Waveguide,“ *IEEE Trans. Microwaves, Antennas and Propagation, IEE Proceedings*, vol. 145, pp. 123 - 127, February 1998.

[5] S. L. Lin, L. W. Li, T. S. Yeo, and M. S. Leong, “Novel Unified Mode Matching Analysis of Concentric Waveguide Junctions,” *IEEE Trans. on Antennas and Propagation*, vol. 148, no. 6, pp. 369–374, December 2001.

[6] R. Sorrentino, F. Alessandri, M. Mongiardo, G. Avitabile, and L. Roselli, “Full-Wave Modeling of Via Hole Grounds in Microstrip by Three-Dimensional Mode Matching Technique,” *IEEE Trans. Microwave Theory and Techniques*, vol. MTT-40, no.12, pp. 2228-2234, December 1992.

[7] R. E. Collin, *Field Theory of Guided Waves*, 2nd ed, IEEE Press, N.Y., 1991.

[8] G. Mazzarella and G. Montisci, “A Rigorous Analysis of Dielectric-Covered Narrow Longitudinal Shunt Slots with Finite Wall Thickness,” *Electromagnetics*, vol. 19, pp. 407-418, October 1999.

[9] G. Montisci, M. Musa, and G. Mazzarella, “Waveguide Slot Antennas for Circularly Polarized Radiated Field,” *IEEE Trans. on Antennas and Propagation*, vol. 52, pp. 619-623, Feb. 2004.

[10] G. Mazzarella and G. Montisci, “Accurate Characterization of the Interaction between Coupling Slots and Waveguide Bends in Waveguide slot Arrays,” *IEEE Trans. Microwave Theory and Techniques*, vol. 48, issue 7, pp. 1154-1157, July 2000.

[11] K. W. Morton and D. F. Mayers, *Numerical Solution of Partial Differential Equations: An Introduction*, Cambridge University Press, 2005.

[12] M. J. Beaubien and A. Wexler, “An Accurate Finite-Difference Method for Higher Order Waveguide Modes,” *IEEE Trans. Microwave Theory and Techniques*, vol. MTT-16, no. 12, pp. 1007-1017, December 1968.

[13] U. V. Rienen, “Triangular Grids: A Review of Resonator and Waveguide Analysis with Classical FIT and Some Reflections on Yee-like FIT- and FEM-Schemes,” *Applied Computational Electromagnetic Society (ACES) Journal*, vol. 19, no. 1, pp. 73–83, March 2004.

[14] G. H. Golub and C. F. Van Loan, *Matrix Computation*, Johns Hopkins Univ. Press, 1989.

Alessandro Fanti graduated in Electronic Engineering at the University of Cagliari on 2006 and currently is a Ph.D. student in Electronic Engineering and Informatics at University of Cagliari. His research activity involves the use of numerical techniques for modes calculation in of guiding structures or in microwaves circuits.

Giuseppe Mazzarella graduated Summa with Laude in Electronic Engineering from the Università "Federico II" of Naples in 1984 and obtained the Ph.D. in Electronic Engineering and Computer Science in 1989. In 1990, he became Assistant Professor at the Dipartimento di Ingegneria Elettronica at the Università "Federico II" of Naples. Since 1992, he is with the Dipartimento di Ingegneria Elettrica ed Elettronica of the Università di Cagliari, first as associate professor and then, since 2000, as full professor, teaching courses in Electromagnetics, Microwave, Antennas and Remote Sensing. His research activity has focused mainly on: efficient synthesis of large arrays of slots, power synthesis of array factor, with emphasis on inclusion of constraints, microwave holography techniques for the diagnosis of large reflector antennas, use of evolutionary programming for inverse problems solving, in particular problems of synthesis of antennas and periodic structures. He is author (or co-author) of about 40 papers in international journals, and is a reviewer for many EM journals.

An Internal Fractional Boundary Placement Model for the Transmission-Line Modeling Method

Mark Panitz and Christos Christopoulos

George Green Institute for Electromagnetic Research
School of Electrical and Electronic Engineering
University of Nottingham, Nottingham, NG7 2RD, United Kingdom
christos.christopoulos@nottingham.ac.uk

***Abstract* ─** This paper describes a fractional boundary placement model for the transmission-line modeling method enabling the positioning of internal boundaries at non-integer cell locations. The model does not introduce any restriction on the maximum timestep of simulations. The connection of the boundary model to a regular mesh is shown and the model is validated using a band-pass waveguide filter model. Results show good agreement with the analytical solution for the waveguide problem.

Index Terms **─** Full-field electromagnetic modeling, time domain analysis, transmission-line matrix methods, waveguide.

I. INTRODUCTION

In its simplest form, the transmission-line modeling method, or matrix method, (TLM) requires space to be discretized into uniform cells of equal size [1]. The most commonly used TLM cell in three dimensions (3D) is the symmetrically condensed node (SCN), a twelve port transmission-line junction which models both electric and magnetic field components at the node centre. The modeling approach applies the equivalence of Maxwell's curl equations to the telegrapher's equations where

$$\underline{E} = -\frac{V}{\Delta l}, \quad \underline{H} = -\frac{I}{\Delta l}. \qquad (1)$$

Space is discretized using such nodes, which are then solved in an explicit manner through a two stage scatter-connect approach. Therefore, the timestep of the simulation is chosen to maintain synchronization throughout the mesh and is determined by the smallest cell size. Unlike some other numerical techniques, the TLM algorithm does not involve any convergence criteria, a property that makes it an inherently stable method [2].

In an uniform SCN mesh all cells are the same size but graded mesh formulations do exist and offer geometrical flexibility [1]. The grading of the mesh determines the smallest cell size and hence the timestep that must be used in the simulation. Typically, the smaller the cell size the smaller the timestep must be.

Perfect electric conductor (PEC) boundaries in the standard TLM method are usually realized by positioning them at cell faces. Hence, boundaries must be positioned at mesh lines within the model. The PEC boundary condition is applied in the connection stage by setting the reflected voltage, from the boundary, to be the negative of the incident voltage.

To accurately model geometry, it is often necessary to arbitrarily position object boundaries within the mesh. The structured mesh may not offer enough flexibility to conform to the model geometry and a higher mesh density or a graded mesh must be used. In both cases, the simulation timestep must be reduced, increasing the total CPU time for the problem. To maintain synchronization and stability, the maximum time step that can be used in the standard 3D TLM method is

$$\Delta t_{\max} = \frac{\Delta l_{\min}}{2c}, \qquad (2)$$

where Δl_{min} is the smallest cell edge length in the mesh.

Submitted On: May 31, 2011
Accepted On: September 12, 2011

A fractional external boundary placement model was developed in [3] where space between an arbitrarily positioned boundary and a structured mesh is modeled by a transmission-line parallel to the boundary. This approach allows the boundaries around cavity type problems to be positioned anywhere within a cell without limiting the timestep used. Here, external refers to the modeling domain, which is the boundary where the modeling space is truncated.

In order to model a general problem where structure is contained within the body of the mesh, for example a waveguide aperture problem or large scale EMC type problem, internal boundaries must be modeled. This requires the correct treatment of fields on both sides of the boundary and along the laminae edge of the boundary, such as around an aperture.

This paper extends the model in [3] to internal boundaries so that objects within the modeling domain can be positioned in an arbitrary manner without modifying the structure of the rest of the mesh. This is done without introducing restriction upon the simulation timestep.

II. TWO DIMENSIONAL FORMULATION

The boundary model is developed initially in two dimensions (2D) in order to reduce the complexity of the formulation. Extension to three dimensions is straightforward and is described in Section III. In 2D, the model will be derived to be coupled to the 2D TLM series node [1]. The series node is formed from four transmission-lines connected at a junction in a series manner.

The aim is to replace the 2D series node by a structure that models the field propagation due to a boundary positioned within the cell. The 2D series node is therefore replaced by the construction shown in Fig. 1 where, in this case, the boundary is positioned along the x-axis. A single boundary cell is present in the mesh and the connecting transmission-lines of the adjacent cell can be seen. Although the 2D node only has four ports, the port numberings are chosen to be consistent with the 3D SCN.

The boundary model is a time-domain implementation of the circuit shown in Fig. 1 which is a 1D transmission-line segment running parallel to the boundary. The boundary properties will be modeled by the inductance and capacitance of the transmission-lines. Coupling of the boundary model to the 2D series nodes is performed through the voltage sources on the transmission-lines and coupling to the boundary end through a potential divider.

Here, only cases where the skin depth is small compared to the boundary thickness are considered. Hence, it is assumed that there is no propagation across the boundary and it is a perfect electric conductor (PEC).

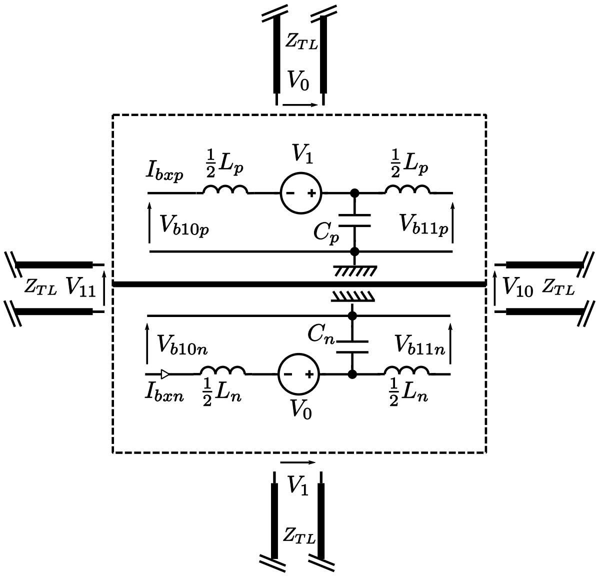

Fig. 1. 2D internal fractional boundary cell - port numbering is consistent with the 3D symmetrically condensed node (SCN).

A. Boundary properties

The two regions of space on either side of the boundary are designated the subscripts *n* and *p*, that is the region which has its normal facing negatively and positively with respect to the coordinate system.

The thickness of the boundary is given by *h* and the displacement of the boundary from the cell face is given by *d* so that

$$d_p + d_n + h = \Delta l, \tag{3}$$

where Δl is the cell spacing. Therefore, for a laminae boundary, the value of *h* is zero and for a real boundary with thickness the value of *h* is in the range $0 < h < \Delta l$. In order to model a boundary with thickness greater than Δl, the modeller must construct the boundary in more than a single plane of cells, in the same manner as would usually be applied in these cases.

The formulation proceeds from the one dimensional telegrapher's equations where, for the positive side of the boundary;

$$-\Delta l \frac{\partial V_{bp}}{\partial x} = L_p \frac{\partial I_{bxp}}{\partial t} - V_1, \tag{4}$$

$$-\Delta l \frac{\partial I_{bxp}}{\partial x} = C_p \frac{\partial V_{bp}}{\partial t}. \tag{5}$$

The per-unit-length capacitance and inductance and characteristic impedance are determined by the volume of space adjacent to the boundary. The capacitance and inductance not modeled by the transmission-lines themselves will be modeled by the transmission-line stubs [1]. The per-unit-length capacitance and inductance and characteristic impedance that are to be modeled by the boundary model are

$$C_p = \frac{C}{\Delta l} = \frac{\varepsilon_0 \Delta l}{d_p}, \tag{6}$$

$$L_p = \frac{L}{\Delta l} = \frac{\mu_0 d_p}{\Delta l} \tag{7}$$

and

$$Z_{bp} = \sqrt{L_p / C_p} = \eta_0 \left(\frac{d_p}{\Delta l} \right). \tag{8}$$

Converting equations (4) and (5) to travelling wave format [3, 4] yields the boundary voltage and current expressions

$$V_{bp} = \frac{\left(V^i_{b10p} + V^i_{b11p} + V^i_{bCp} \right)}{\sqrt{2}}, \tag{9}$$

$$I_{bxp} = \frac{\left(V^i_{b10p} - V^i_{b11p} - V^i_{bLpx} + \tfrac{1}{2} V_1 \right)}{\sqrt{2} Z_{bp}}. \tag{10}$$

In (10), the voltage coupled from the bulk mesh is given by

$$V_1 = 2V_0^r - I_{bxp} Z_{TL}, \tag{11}$$

where V_0^r is the reflected port voltage on the series node coupling to the boundary model.

The stub impedances are expressed here in terms of Z_{bp} and have been obtained in the same manner as in [3] where speed of light propagation along the transmission-line is required. This requires the introduction of the stubs to model additional capacitance and inductance within the boundary model. These expressions define the TLM equivalent circuit of the boundary model which is shown in Fig. 2 for both sides of the boundary.

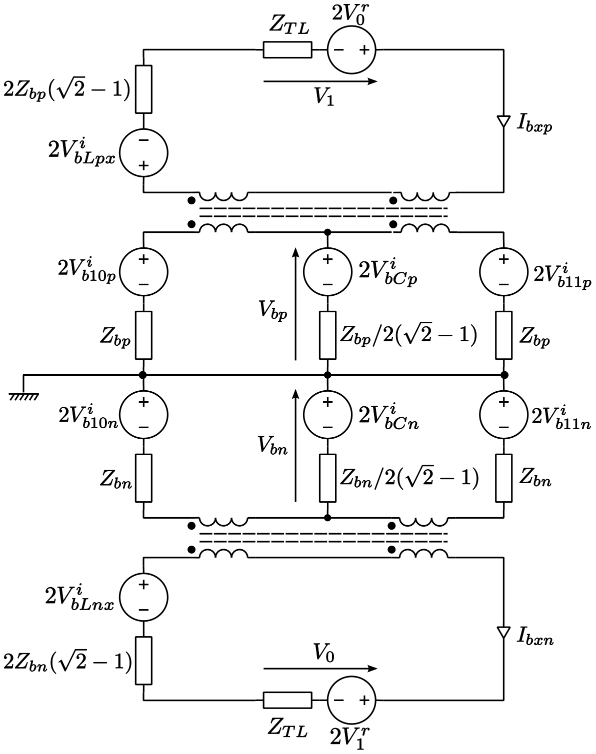

Fig. 2. Thevenin equivalent circuit of the 2D internal fractional boundary model - port numbering is consistent with the 3D symmetrically condensed node (SCN).

B. Boundary update

The boundary model is updated during the connection stage of the TLM algorithm. Therefore, the boundary model uses the reflected voltage from the adjoining cell as its inputs. Following scattering throughout the mesh, the voltage and current in the boundary cells are calculated using equations (9) and (10). The boundary scatter then proceeds by calculating the voltages reflected along the boundary length given by

$$V^r_{b10p} = V_{bp} - I_{bxp} Z_{bp} - V^i_{b10p} \tag{12}$$

and

$$V^r_{b11p} = V_{bp} + I_{bxp} Z_{bp} - V^i_{b11p}. \tag{13}$$

The stub voltages are updated for the next timestep in the usual way so that for the inductive stub

$${}_{k+1}V^i_{bLpx} = -\left({}_{k}V^i_{bLpx} + 2\left(\sqrt{2}-1\right) I_{bxp} Z_{bp} \right) \tag{14}$$

and for the capacitive stub

$$ {}_{k+1}V^i_{bCp} = V_{bp} - {}_kV^i_{bCp}. \tag{15}$$

These expressions complete the update of voltages within the boundary model. Connection must also be made to the nodes of the bulk mesh adjacent to the boundary nodes, which is described in the following subsection.

C. Boundary connection

Three types of connection must take place in the boundary model: connection along the boundary, connection to the mesh normal to the boundary, and connection to the mesh at the ends of the boundary.

Connection along the length of the boundary is performed by calculating the total voltage at the connecting ports. Connection of the *n*th boundary node to the (*n*+1)th boundary node would yield a total voltage of

$$V_{b11,10p} = \left(2\,{}_kV^r_{b11p}(n)Z_{bp}(n+1) + 2\,{}_kV^r_{b10p}(n+1)Z_{bp}(n)\right) / \left(Z_{bp}(n)+Z_{bp}(n+1)\right) \tag{16}$$

and hence, the incident voltages at the next timestep are given by

$$ {}_{k+1}V^i_{b11p}(n) = V_{b11,10p} - {}_kV^r_{b11p}(n) \tag{17}$$

and

$$ {}_{k+1}V^i_{b10p}(n+1) = V_{b11,10p} - {}_kV^r_{b10p}(n+1). \tag{18}$$

This connection procedure allows the boundary displacement or thickness to vary between boundary cells and ensures conservation of energy as a result of these variations.

Connection to the bulk mesh normal to boundary is simply carried out through the voltage source on the boundary transmission-line. The mesh is updated using the expression

$$ {}_{k+1}V^i_0 = {}_kV^r_0 - {}_kI_{bxp}Z_{TL}. \tag{19}$$

Finally, connection to the edge of the boundary is performed by calculating the loop current at the boundary end given by

$$ {}_kI_{b10,11} = \frac{-2\left({}_kV^r_{b10p} + {}_kV^r_{b10n}\right) + 2\,{}_kV^r_{11}}{Z_{TL} + Z_{bp} + Z_{bn}}, \tag{20}$$

where ${}_kI_{b10,11}$ denotes the current loop due to the boundary ports *10p* and *10n* and the regular TLM port *11*. The reflected port currents are then given by

$$ {}_{k+1}V^i_{11} = {}_kV^r_{11} - {}_kI_{b10,11}Z_{TL}, \tag{21}$$

$$ {}_{k+1}V^i_{b10p} = {}_kV^r_{b10p} + {}_kI_{b10,11}Z_{bp}, \tag{22}$$

and

$$ {}_{k+1}V^i_{b10n} = {}_kV^r_{b10n} + {}_kI_{b10,11}Z_{bn}. \tag{23}$$

These expressions form a potential divider circuit at the boundary edge to ensure that the incident field is split between either side of the boundary in the correct manner. These expressions complete the boundary to bulk mesh updates and provide the incident voltages for the next iteration of the model.

III. EXTENSION TO THREE DIMENSIONS

The internal boundary model has been defined in 2D based on the series TLM node. Extension to three dimensions (3D) is realised by modeling the boundary as a 2D shunt grid adjacent to the boundary, rather than the 1D line used for the 2D model.

Following the same procedure as in 2D and starting from the telegrapher's equations for the 2D shunt grid:

$$-\Delta l\,\frac{\partial V_{bp}}{\partial x} = L_p\,\frac{\partial I_{bxp}}{\partial t} - V_1, \tag{24}$$

$$-\Delta l\,\frac{\partial V_{bp}}{\partial y} = L_p\,\frac{\partial I_{byp}}{\partial t} - V_7, \tag{25}$$

and

$$-\Delta l\,\frac{\partial I_{bxp}}{\partial x} - \Delta l\,\frac{\partial I_{byp}}{\partial y} = C_p\,\frac{\partial V_{bp}}{\partial t}, \tag{26}$$

yields the circuit equivalent equations that are to be solved. The boundary impedance remains the same as in 2D and is given by (8) and the update equations are given

$$V_{bp} = \frac{\left(V^i_{b8p} + V^i_{b9p} + V^i_{b10p} + V^i_{b11p}\right)}{4}, \tag{27}$$

$$I_{bxp} = \frac{\left(V^i_{b10p} - V^i_{b11p} - V^i_{bLpx} + \tfrac{1}{2}V_1\right)}{4Z_{bp}}, \tag{28}$$

and

$$I_{byp} = \frac{\left(V^i_{b8p} - V^i_{b9p} - V^i_{bLpy} + \tfrac{1}{2}V_7\right)}{4Z_{bp}}. \tag{29}$$

In the 3D case, there is no capacitive stub as all the required capacitance is modeled by the link lines.

The link line voltages are scattered in the same manner as in (12) and (13) and the stub voltage is updated as in (14), where in this case the inductive stub impedance is simply $2Z_{bp}$.

A. Boundary connection

The boundary connection in 3D is performed in the same manner as in 2D. At each connecting port, the total field is calculated and the reflected field is then obtained and is dependent on the displacement and thickness of the boundary. When connecting the boundary edge to the 3D SCN, the coupling requires treatment of the voltage port that does not have a corresponding boundary port, such as port V_5 as shown in Fig. 3.

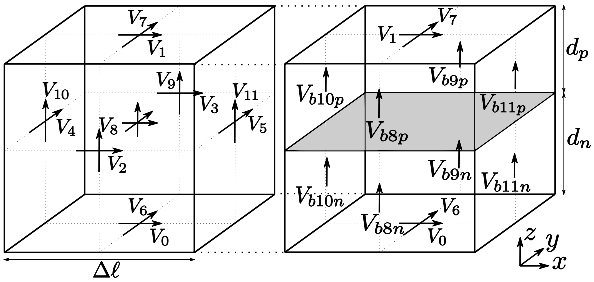

Fig. 3. Port numberings of the 3D boundary model (right) and a connecting adjacent SCN (left) showing the unmatched SCN port (V_5).

Connection of the other port, normal to the boundary, is performed in the same way as in 2D. The total field is calculated and the reflected voltages are then obtained. In the case of a boundary in the *x*-*y* plane as shown in Fig. 3, the electric field polarised normal to the boundary is assumed to be continuous at the boundary edge, permitting direct connection between the two regions. The unmatched port of the SCN (V_5) is polarised in the plane of the boundary however.

The boundary displacement must be less than the cell it is within, hence less than *Δl*. Furthermore, as a rule of thumb, the mesh cell size, *Δl*, should be smaller than one-tenth of the wavelength of interest to provide suitable accuracy and reduce dispersion [1]. Hence, it is assumed that the field polarised in the plane of the boundary in the region adjacent to the boundary is zero. This component is not modeled by the boundary model, and furthermore, this assumption implies that the field polarised parallel to and incident upon the edge to the boundary plate sees a PEC boundary condition. Hence, this port of the SCN is updated through

$$ {}_{k+1}V_5^i = -{}_kV_5^r , \qquad (30) $$

in the same manner as the PEC boundary condition is usually applied to the SCN cell.

IV. COMPUTATIONAL PERFORMANCE

The computational performance of this numerical method is assessed with respect to the scattering process within a free-space series node in 2D and the free-space SCN node in 3D. The rationale for this is that the internal boundary model described here replaces the whole TLM cell and, although solved during the connection process, the update of the internal boundary cell can be considered an equivalent scattering process for the cell.

The computational requirements of the boundary model with the normalised free-space TLM cell are compared for 2D in Table 1 and in 3D in Table 2, where for the free-space cells the circuit based algorithm described in [4] is used.

Table 1: Comparison of the computational requirements of the free-space series node and the internal boundary node in 2D

	Free-space	**Boundary**
Variables	4	12
Calculations	7	14

Table 2: Comparison of the computational requirements of the free-space SCN and the internal boundary node in 3D

	Free-space	**Boundary**
Variables	12	18
Calculations	18	22

An expected increase in variables and computations can be seen for the boundary cells. However, it is not expected that this increase will affect the computational performance of the full TLM model greatly as the number of boundary cells would be only a small fraction of the total cells in the simulation model.

The most significant computational advantage of this procedure is that no modification of the simulation timestep is required to accommodate the boundary displacement. The transmission-line impedances are determined by the offset of the boundary from the cell edges as in (8). It can be seen that all transmission-line impedances for the link lines and stubs are positive for all positive displacements. Hence, there is no restriction to the simulation timestep necessary to maintain stability of the model as is required in a graded approach. Even as the boundary displacement tends to zero the simulation timestep can still be maintained at the maximum of the bulk mesh. Hence, any value of h in the limit $0 < h < \Delta l$ and d in the limit $0 < d < \Delta l$ can be used providing (3) is satisfied without a reduction in timestep.

Furthermore, as the timestep is not affected by the introduction of the boundary model it is not necessary to load the bulk mesh with stubs to adjust its timestep, as required in a graded mesh. Therefore, this model avoids the unwanted dispersion effects of the stub loaded TLM mesh [1] giving improved model accuracy over graded approaches.

V. VALIDATION

Validation of the boundary model addresses the two parts of the algorithm: the displacement of the boundary within the cell and the connection of the boundary to the surrounding mesh.

Regarding the displacement of the boundary, the accuracy of the external boundary model is determined in detail in [3] it is shown that the propagation velocity and boundary displacement have errors of only 0.00003% and 0.01%, respectively. The displacement model used here is based on the same procedure as that in [3], therefore the errors in the propagation velocity and boundary displacement will be identical to that of the external boundary.

To validate the model in this paper, it must be ensured that the procedure used to couple the ends of the boundary to the regular mesh is valid and that the displacement model functions correctly on both sides of the boundary. The validation is performed using a waveguide band-pass filter model in the following subsection.

A. Waveguide band-pass filter

The boundary model developed here takes into account two modes of connection to the bulk mesh, that is perpendicular and normal to the boundary. Here, this model is validated using a case requiring use of both the displacement and connection of the boundary model.

A waveguide filter within a WR-28 (f_c = 31GHz) waveguide is chosen consisting of four inductive apertures with periodic separation. A schematic of the structure is shown in Fig. 4. where the H_{10} (TE_{10}) mode is excited so that the electric field is orientated vertically in the waveguide.

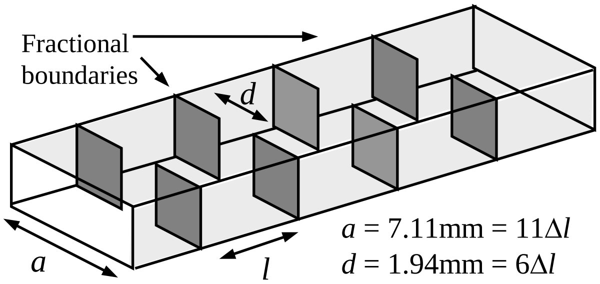

Fig. 4. Waveguide band-pass filter with the apertures modeled using the boundary model.

The admittance of each of the inductive apertures is given in [5] where

$$Y/Y_0 = -\left(j\lambda_g/a\right)\cot^2\left(\pi d/2a\right). \qquad (31)$$

In (31) λ_g is the guide wavelength, Y_0 is the admittance of the waveguide without the aperture and the dimensions are as labeled in Fig. 4. Hence, combining the multiple apertures shown in Fig. 4. yields an analytical reflection coefficient of

$$\cosh\left(\Gamma\right) = \cos\left(\frac{2\pi l}{\lambda_g}\right) + \frac{\lambda_g}{2a}\cot^2\left(\frac{\pi d}{2a}\right)\sin\left(\frac{2\pi l}{\lambda_g}\right). \qquad (32)$$

In the pass-band $|\Gamma|<1$ and the reflection coefficient has no real part. The geometry is initially modeled using only the usual TLM boundary model where the aperture spacing is chosen to be an integer number of cells, so that a = 7.11mm = $11\Delta l$ and the aperture width is d = 1.94mm = $6\Delta l$. Using the standard boundary model, the aperture spacing was set to $l = 20\Delta l$ and $19\Delta l$ and the |S21| response of the filter was simulated. The H_{10} mode was propagated down the waveguide and the response was taken with and without the filter inserted.

The internal fractional boundary model was then used on the first and third apertures to model a separation of $19.5\Delta l$, i.e. with a boundary displacement of $0.5\Delta l$. The boundary developed here allows this case to be modeled without any change to the mesh spacing or the simulation timestep. The response of the three aperture placements are shown in Fig. 5.

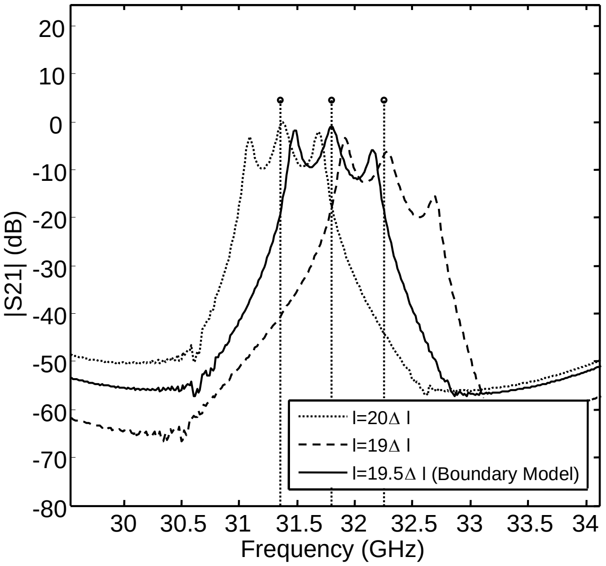

Fig. 5. |S21| response of the waveguide filter using three different aperture separations and the corresponding analytical solutions (vertical lines).

The pass-band of the waveguide filter can be easily identified in each case and the spacing of the apertures can be seen to adjust the centre frequency of the filter. The boundary model has been used to model the intermediate aperture spacing. The result shows that the model has allowed modeling of this intermediate case as the pass-band can be seen to be directly between the two extreme cases.

There is excellent agreement with the analytical solution calculated using (32) for the centre frequency of the filter, where the analytical results are shown by the vertical dotted lines terminated by small circles in Fig. 5. It was possible to obtain this numerical result without any modification of the rest of the mesh or any adjustment of the simulation timestep. This makes the model very suitable for optimisation problems where it may be necessary to modify the position of structures by small amounts between simulations.

VI. CONCLUSION

An internal boundary model for the TLM method has been developed allowing unrestricted boundary placement with no deleterious effect on the timestep. This model allows PEC structures to be positioned anywhere within a structured TLM mesh without the need for a graded mesh approach. This offers significant advantages in computational runtimes and modeling accuracy.

Coupling of the boundary to the bulk mesh has been discussed for connection both perpendicular and parallel to the boundary. Validation using a band-pass waveguide filter shows that the model allows the filter apertures to be arbitrarily and accurately positioned. The results agree well with the analytical centre frequencies of the band-pass models.

ACKNOWLEDGMENT

The authors would like to acknowledge the support of BAE Systems and EPSRC (GR/S71552/01).

REFERENCES

[1] C. Christopoulos. *The Transmission-line Modelling Method*, Piscataway, NJ: IEEE Press, 1995.
[2] R. Ciocan, N. Ida, E. Ciocan, and H. Jiang. “Applications of the Transmission Line Matrix Method to Microwave Scanning Microscopy,” *Applied Computational Electromagnetic Society (ACES) Journal*, 19(1), pp. 94-100, Mar. 2004.
[3] M. Panitz, J. Paul, and C. Christopoulos, “A Fractional Boundary Placement Model using the Transmission-Line Modelling Method,” *IEEE Transactions on Microwave Theory and Techniques,* 57(3), 2009.
[4] J. Paul, *Modelling of General Electromagnetic Material Properties in TLM*, Ph.D. dissertation, School of Electrical and Electronic Engineering, The University of Nottingham, Oct. 1998.
[5] S. Ramo, J. R. Whinnery, and T. Van Duzer, *Fields and Waves in Communication Electronics*. NY: Wiley, 3rd ed, 1994.

Mark Panitz was born in Scunthorpe, U.K., in 1983. He received the M.Sci.degree in Physics from the University of Nottingham, U.K., in 2006. He received his Ph.D. in Electrical and Electronic Engineering from the University of Nottingham. U.K., in 2011. His research involved the numerical modeling and characterisation of highly reverberant, low-loss, time-varying environments with an assessment of their impact on wireless communication systems and protocols. Currently he is working with BAE Systems, U.K., as a research scientist. His research interests include Computational Electromagnetics and Electromagnetic Compatibility. He is the author of many papers in wireless propagation modeling in resonant systems and computational electromagnetic modeling.

Christos Christopoulos was born in Patras, Greece, on September 17th, 1946. He received the Diploma in Electrical and Mechanical Engineering from the National Technical University of Athens in 1969 and the M.Sc. and D.Phil. from the University of Sussex.

He is currently Professor of Electrical Engineering at the University of Nottingham. His interests include Computational Electromagnetics, Electromagnetic Compatibility and Protection of Power Networks.

He is the author of over 350 publications, seven books, and seven chapter contributions. He is a member of the IET and an IEEE Fellow. He is a past Executive Team Chairman of the IEE Professional Network in EMC and Associate Editor of the IEEE EMC Transactions.

Implications of Galilean Electromagnetism in Numerical Modeling

Francesca Rapetti and Germain Rousseaux

Department of Mathematics "J.-A. Dieudonné "
C.N.R.S. & Univ. de Nice, Parc Valrose, 06108 Nice cedex 02, France
Francesca.Rapetti@unice.fr, Germain.Rousseaux@unice.fr

Abstract – The purpose of this article is to present a wider frame to treat the quasi-static limit of Maxwell's equations. We discuss the fact that there exists not one but indeed two dual Galilean limits, the electric and the magnetic one. We start by a re-examination of the gauge conditions and their compatibility with Lorentz and Galilean covariance. By means of a dimensional analysis on fields and potentials we first emphasize the correct scaling yielding the equations in the two limits. With this particular point of view, the gauge conditions of classical electromagnetism are continuity equations whose range of validity depend on the relativistic or Galilean nature of the underlying phenomenon and have little to do with mathematical closure assumptions taken without physical motivations. We then present the analysis of the quasi-static models in terms of characteristic times and visualize their domains of validity in a suitable diagram. We conclude by few words on the Galilean electrodynamics for moving media, underlying the transformation laws for fields and potentials which are valid in the different limits.

Index Terms – Dimensional analysis, gauge conditions, quasi-static approximation of Maxwell's eqs, transformation laws in moving frames.

I. INTRODUCTION

A detailed electromagnetic analysis of electrotechnical devices often relies on theoretical and numerical tools applied to approximated low frequency models of Maxwell's equations. These quasi-static models are obtained from the full set of Maxwell's equations by neglecting particular couplings of electric and magnetic quantities, depending on the system dimensions, time constants, values of the coefficients appearing in the physical laws, etc. The electroquasistatic (EQS) approximation usually fits when high-voltage technology and microelectronics are involved, as the capacitive and resistive effects prevail over the inductive ones. The magnetoquasistatic (MQS) approximation must be adopted when inductive effects have to be taken into account, as it occurs in transformers or electrical machine design. These models are known as Galilean limits (GL) of classical electromagnetism [1, 2, 3].

In this publication, we present a wider frame to state the validity of the quasi-static model versus the particular electromagnetic phenomenon under exam. By relying on a dimensional analysis first and on the characteristic times secondly, we start by reasoning in terms of field equations. We then extend the analysis to scalar and vector potentials and to the gauge conditions normally inferred to ensure potential's uniqueness. We conclude by few words on the Galilean electrodynamics of moving media, and remark that the transformation laws of fields and potentials from a moving reference to a fixed one depend on the Galilean limit characterizing the considered problem.

Dimensional analysis is a tool historically well established in the field of fluid mechanics and other fields of physics [4] that allows to simplify a problem by reducing the number of system parameters (Newton in 1686 and Maxwell in 1865 played a major role in establishing modern use of dimensional analysis by distinguishing mass, length, and time as fundamental units, while referring to other units as derived). Dimensional analysis is based on the fact that a physical law must be independent of the units used to measure the physical variables. As direct applications, it can be used to check equations (they must have the same dimensions in the left and in the right hand sides) as well as the consistency of derived models, as in the present paper. Moreover, it can be

Submitted On: May 11, 2011
Accepted On: September 16, 2011

used to reason on complex physical situations by analyzing reduced models (a model of a few centimeters can give insight on the dynamics of jet airplane, for example). The main difficulty with dimensional analysis is the selection of the fundamental parameters for a given problem. In Sections II and III, we apply dimensional analysis to derive the Galilean quasi-static models and in Section IV, we explain how the scalings characterizing these models can be deduced on the basis of fundamental physical parameters by applying the famous Pi theorem of Vaschy-Buckingham [5].

II. GALILEAN LIMITS OF MAXWELL'S EQUATIONS

An electromagnetic phenomenon happens in a spatial arena of extension ℓ in a duration τ. The arena is a continuous medium with constitutive properties ϵ, μ, and σ, which are supposed to be constant for simplicity (otherwise they are time and space dependent tensors). Applying the Vaschy-Buckingham theorem of dimensional analysis, we can construct dimensionless parameters which would characterize the electromagnetic response of the continuous medium. As we will deal with Galilean approximations, we introduce the typical velocity v of the system with modulus $|v| = \ell/\tau$ and we compare it with the light celerity in the continuous medium $c_m = 1/\sqrt{\epsilon\mu}$. The Galilean limit (quasi-static approximation) corresponds to $|v| \ll c_m$. This assumption is not sufficient to choose between the MQS or the EQS approximations. Let us set $E = e\mathcal{E}$ and $B = b\mathcal{B}$, where e, b are reference quantities and $\mathcal{E}$, $\mathcal{B}$ are non-dimensional quantities of order 1. We just recall that in dimensional analysis the spatial (resp. time) differentiation $\partial_x E$ (resp. $\partial_t E$) is equivalent to $\frac{e}{\ell}$ (resp. $\frac{e}{\tau}$). Moreover, we adopt the notation $a \sim b$ to say that the quantities a and b have the same magnitude order, whereas $a \simeq b$ when a and b are approximatively equal.

In the empty space, Faraday's law and the expression of $|v|$ yield

$$\nabla \times E = -\partial_t B, \quad \frac{e}{\ell} \sim \frac{b}{\tau}, \quad e \sim |v|\, b. \tag{1}$$

The generalized Ampère's law and the expression of c_m, which equals the light speed $c = 1/\sqrt{\epsilon_0\mu_0}$, result in

$$\nabla \times H = -\partial_t D, \quad \frac{b}{\mu_0 \ell} \sim \frac{\epsilon_0 e}{\tau}, \quad b \sim \frac{|v|}{c^2}\, e. \tag{2}$$

Thus, two scalings appear, the first $e \sim |v|\, b$ and the second $b \sim \frac{|v|}{c^2}\, e$. In the relativistic regime, *i.e.* $|v| \sim c$, the two scalings are the same. In the Galilean regime, *i.e.* $|v| \ll c$, the two scalings are different and if one replaces the expression of b given in (2) into the expression of e given in (1), we gets $|v| \sim c$ which is in contradiction with the Galilean assumption $|v| \ll c$. This means that in the Galilean regime, the two scalings are not simultaneously valid, thus the Faraday's and generalized Ampère's laws cannot be coupled. To choose the scaling, we have to look at the sources (charges or currents) of the electromagnetic phenomenon under consideration. Let us suppose to be once again in the empty space. The Gauss's theorem yields

$$\nabla \cdot D = \rho, \quad \frac{\epsilon_0 e}{\ell} \sim \rho, \tag{3}$$

and Ampère's theorem results in

$$\nabla \times H = J, \quad \frac{b}{\mu_0 \ell} \sim J. \tag{4}$$

Then, "dividing" (4) by (3), we get

$$\frac{\frac{b}{\mu_0 \ell}}{c\frac{\epsilon_0 e}{\ell}} \sim \frac{J}{c\rho}, \quad \frac{J}{c\rho} \sim \frac{b}{c\,\epsilon_0 \mu_0 e}, \quad \frac{J}{c\rho} \sim \frac{c\, b}{e}. \tag{5}$$

Therefore, if $J \gg \rho\, c$, that is when the dielectric effect of charges is negligible, we obtain $e \ll c\, b$ and the MQS approximation is the correct one. On the contrary, if $J \ll \rho\, c$, that is when the conducting effect is negligible, we get $e \gg c\, b$ and the EQS approximation has to be adopted. In fact, the conditions $|v| \ll c$ and $e \ll c\, b$ are compatible with the MQS scaling $e \sim |v|\, b$ (with the EQS scaling we would obtain $c\, b \gg c\, b$ that is a nonsense). On the contrary, the conditions $|v| \ll c$ and $e \gg c\, b$ are compatible with the EQS scaling $c\, b \sim \frac{|v|}{c} e$ (with the MQS scaling we would obtain $|v|\, b \gg c\, b$, thus $|v| \gg c$ against the Galilean regime assumption $|v| \ll c$). From the above considerations, slowly time varying fields can be described by either the Galilean electric limit of Maxwell's equations given by

$$\begin{aligned} \nabla \times E \simeq 0, &\quad \nabla \times H = J + \partial_t D, \\ \nabla \cdot D = \rho, &\quad \partial_t \rho + \nabla \cdot J = 0, \end{aligned} \tag{6}$$

or the Galilean magnetic limit given by

$$\begin{aligned} \nabla \times E = -\partial_t B, &\quad \nabla \times H \simeq J, \\ \nabla \cdot B = 0, &\quad \nabla \cdot J = 0, \end{aligned} \tag{7}$$

or the Galilean stationary limit of Maxwell's equations, also known as quasi-stationary conduction (QSC) approximation, where no time derivative appears at very low frequencies

$$\begin{array}{ll} \nabla\times E \simeq 0, & \nabla\times H \simeq J, \\ \nabla\cdot D = \rho, & \nabla\cdot B = 0. \end{array} \tag{8}$$

All models have to be completed with classical constitutive relations and suitable boundary and initial conditions. The internal consistency of models (6) and (7) by using the Jefimenko form [7] of the solutions to the wave equation for fields works out neatly. It can be easily shown that the two scalings (1) and (2) obtained here by dimensional analysis are in agreement with those expressed in terms of fields and time scalings given in [6]. Note however that the existence of two Galilean limits is not so obvious if we naively take the limit $c \to +\infty$ in equations (6) and (7) (see [3] for the details). The two limits can be traced back to the possibility of keeping either one of the two constants ϵ_0, μ_0 finite, while the second one "approaches to zero", even if we are aware of the fact that these two physical quantities never tend to zero in real life. As explained in the conclusion of [1], we may understand the magnetic limit by keeping μ_0 only, and by writing $\epsilon_0 = 1/(\mu_0\, c^2)$ where c approaches infinity; for the electric limit, we reverse the role of μ_0 and ϵ_0. One can anyway be bothered by the presence of light speed c in the above expressions despite we are considering phenomena where $|v| \ll c$. In Galilean electromagnetism, the appearing velocity is $c_u = 1/\sqrt{\epsilon_0\mu_0}$. This velocity is independent of specific units (same value with Gaussian or SI units) and arises from using only action-at-a-distance forces in which an instantaneous propagation is assumed [8]. It can thus be considered as a fundamental constant in nature. We are used to identify c_u with c the speed of light in vacuum because these velocities have the same numerical value. We have to remember that the speeds c_u and c emerge from different physical considerations (Maxwell indeed has been the first one who stated $c_u = c$ in 1862) but we are not going to develop this point here.

III. POTENTIALS AND GAUGE CONDI--TIONS IN THE GALILEAN REGIME

We now focus on the magnetic vector potential A and the scalar electric one V associated to E and B by the well-known relations

$$E = -\partial_t A - \nabla V, \qquad B = \nabla\times A. \tag{9}$$

The equations of classical electromagnetism in terms of potentials are

$$\left(\frac{1}{c^2}\partial_{tt} - \Delta\right)\begin{pmatrix} A \\ V \end{pmatrix} = \begin{pmatrix} \mu_0\, J \\ \rho/\epsilon_0 \end{pmatrix}$$

and their quasi-static approximation for $|v| \ll c$ yields

$$-\Delta A \simeq \mu_0 J, \quad -\Delta V \simeq \rho/\epsilon_0. \tag{10}$$

In terms of magnitude orders, let us write again $A = a\mathcal{A}$ and $V = \mathtt{V}\mathcal{V}$, then "dividing" in (10) the first equation by the second one, we get

$$\frac{a}{\mathtt{V}} \sim \frac{J}{\rho\, c^2}, \quad \frac{c\, a}{\mathtt{V}} \sim \frac{J}{\rho\, c}. \tag{11}$$

As already seen, in the MQS approximation $J \gg \rho\, c$ so $c\, a \gg \mathtt{V}$ (in fact, the correct scaling is $\mathtt{V} \approx |v|\, a$) and in the EQS approximation $J \ll \rho\, c$ so $c\, a \ll \mathtt{V}$ (and the correct scaling is $a \approx \frac{|v|}{c^2}\mathtt{V}$). Let us look back to (9): $B = \nabla\times A$ gives *always* $b \sim \frac{a}{\ell}$ whereas $E = -\partial_t A - \nabla V$ yields $e \sim \frac{a}{\tau} + \frac{\mathtt{V}}{\ell}$. On the one hand, when $c\, a \ll \mathtt{V}$, with $|v| \ll c$,

$$|v|\, a \ll \mathtt{V}, \quad \frac{\ell}{\tau} a \ll \mathtt{V}, \quad \frac{a}{\tau} \ll \frac{\mathtt{V}}{\ell}, \tag{12}$$

so $e \sim \frac{\mathtt{V}}{\ell}$, thus $E = -\nabla V$ which is compatible with the EQS model where $\nabla\times E = 0$. On the other hand, if $c\, a \gg \mathtt{V}$,

$$a \gg \mathtt{V} \;\text{ but }\; |v| \ll c, \quad \frac{a}{\tau} \sim \frac{\mathtt{V}}{\ell}, \tag{13}$$

so $E = -\partial_t A - \nabla V$ is compatible with the MQS equation $\nabla\times E = -\partial_t B$. Let us finally consider the well-known gauge conditions usually adopted in the QS context for A and V. From the Lorenz condition $\nabla\cdot A + \frac{1}{c^2}\partial_t V = 0$ we get $c\, a + \frac{|v|}{c}\mathtt{V} \sim 0$. In the MQS approximation, the Lorenz condition becomes the Coulomb one ($\nabla\cdot A = 0$) as $c\, a \gg \mathtt{V}$ and $|v| \ll c$. But in the EQS limit, as $c\, a \ll \mathtt{V}$ but $|v| \ll c$, the two terms $\nabla\cdot A$ and $\frac{1}{c^2}\partial_t V$ have the same magnitude order, and thus Lorenz gauge condition holds. Coulomb and Lorenz conditions in the empty space are in reality a particular case of a more general condition, that reads

$$\nabla\cdot A + \mu\epsilon\partial_t V = -\mu\sigma V, \tag{14}$$

valid in a medium with electric permittivity ϵ and magnetic permeability μ, introduced by Stratton

[9] in 1941 to cope with the propagation of electromagnetic waves in Ohmic conductors with electric conductivity $\sigma \neq 0$.

IV. THE GALILEAN REGIME AND ITS CHARACTERISTIC TIMES

Quasi-static models are valid when $\tau_{em} = \ell/c$, the light transit time in the medium, is small compared to τ (cf. Table 1).

Table 1: Range of the characteristic time τ for the different models derived from Maxwell's eqs

Full set of Maxwell's eq.	Quasi-static regime	Static regime
$0 \leq \tau \leq \tau_{em}$	$\tau_{em} \leq \tau \leq \tau_m, \tau_e$	$\tau \geq \tau_m, \tau_e$

Together with τ_{em}, we need to define three other quantities, namely $\ell^\star = \frac{1}{\sigma}\sqrt{\frac{\epsilon}{\mu}} = \frac{1}{\sigma\eta}$, the constitutive length (η is the medium impedance), $\tau_e = \epsilon/\sigma$, the electric charge diffusion time (*i.e.*, the characteristic time with which the unpaired electric charge decays in a conductor), and $\tau_m = \mu\sigma\ell^2$, the current density diffusion time (*i.e.*, the characteristic time with which the current density and hence the magnetic field penetrates in a conductor). A natural question arises: "where do these quantities come from ?". Moreover, "which is the role of these constants in the definition of the quasi-static regimes ?".

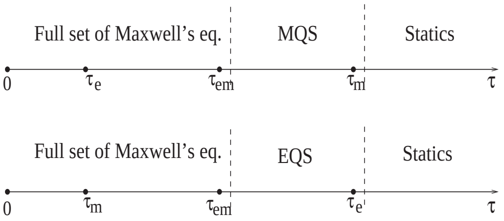

Fig. 1. Case $\tau_m > \tau_e$ (up) and $\tau_m < \tau_e$ (down).

To understand their origin and importance, we perform a dimensional analysis of the Stratton condition (14), that yields

$$\frac{a}{\ell} + \mu\epsilon\frac{\mathtt{V}}{\tau} \sim \mu\sigma\mathtt{V}, \qquad I + II \sim III.$$

By computing three dimensionless ratios, namely II/I, III/I, and III/II, we see appearing the characteristic time constants:

$$\begin{aligned} \frac{II}{I} &\sim \frac{|v|}{c}\frac{\mathtt{V}}{ca} = \frac{\tau_{em}}{\tau}\frac{\mathtt{V}}{ca}, \qquad \frac{III}{II} \sim \frac{\tau}{\tau_e}, \\ \frac{III}{I} &\sim \frac{\ell}{\ell^*}\frac{\mathtt{V}}{ca} = \frac{\tau_m}{\tau_{em}}\frac{\mathtt{V}}{ca} = \frac{\tau_{em}}{\tau_e}\frac{\mathtt{V}}{ca} \end{aligned}$$

(here c denotes $c_u = 1/\sqrt{\mu\epsilon}$). We start by remarking that $\tau_{em} = \sqrt{\tau_e\tau_m}$, *i.e.* τ_{em} defines the geometric mean of the previously defined quantities τ_e and τ_m. The three time constants can be arranged in two different ways, either $\tau_m > \tau_e$ or $\tau_m < \tau_e$ (Fig. 1).

In order to underline the dependence of τ_m and τ_e on the length ℓ, it is better to consider a two-dimensional visualization, where one axis reflects the effect of τ and the other that of ℓ, as firstly proposed in [10]. We thus consider the plane (x, y) where $x := \log(\tau/\tau_{em})$ and $y := \log(\ell/\ell^*)$ and we separate it in sectors by remarking that

$$\begin{aligned} &\tau = \tau_{em}, && \log(\tau/\tau_{em}) = \log(1) && (x = 0), \\ &\tau = \tau_e, && \log(\tau/\tau_{em}) = \log(\ell^*/\ell) && (y = -x), \\ &\tau = \tau_m, && \log(\tau/\tau_{em}) = \log(\ell/\ell^*) && (y = x). \end{aligned}$$

The Galilean regime, characterized by $\tau_{em} \ll \tau$, is located where $x > 0$ on the plane (x, y) of Fig. 2. On the one hand, the expansion $b \sim (\tau_m/\tau)b + (\tau_{em}/\tau)^2 b$, resulting from the generalized Ampere's theorem, with the MQS scaling $e \sim |v|b$, has to be truncated at the first term in (τ_m/τ) as the second term in $(\tau_{em}/\tau)^2$ is negligible (this means $J \gg \partial_t D$). On the other hand, in the expansion $b \sim (\tau/\tau_e)b + b$, resulting from the generalized Ampere's theorem, with the EQS scaling $e \sim (c^2/|v|)b$, the first term in (τ/τ_e) is negligible with respect to the second one (this means $J \ll \partial_t D$).

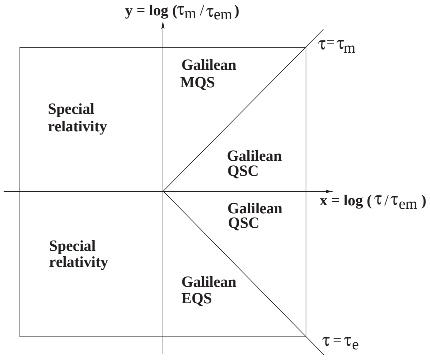

Fig. 2. Graphical representation of electromagnetic model validity.

Let us go back to the gauge condition validity. From Stratton condition with the MQS scaling ($\mathtt{V} \approx |v|a$) we get $a + (\tau_{em}/\tau)^2 a \sim (\tau_m/\tau)a$, with the term in $(\tau_{em}/\tau)^2$ negligible with respect to the term in (τ_m/τ). Stratton's condition results in $\nabla \cdot A \simeq -\mu\sigma V$, as indicated in Table 2. If the EQS scaling ($a \approx (|v|/c^2)\mathtt{V}$) is adopted, we get

$a + a \sim (\tau_{em}/\tau_e)(\mathtt{V}/c)$, thus the right-hand side in Stratton's condition is negligible with respect to the left-hand side. Stratton's condition yields $\nabla \cdot A + \mu\epsilon\partial_t V \simeq 0$, as indicated in Table 2.

Table 2 : Model versus gauge condition validity

Model	gauge condition
Special relativity	$\nabla \cdot A + \mu\epsilon\partial_t V = -\mu\sigma V$
Galilean EQS	$\nabla \cdot A + \mu\epsilon\partial_t V \simeq 0$
Galilean MQS	$\nabla \cdot A \simeq -\mu\sigma V$
Galilean QSC	$\nabla \cdot A \simeq -\mu\sigma V$

The dimensional analysis of Stratton condition allows to introduce τ_{em}, τ_e and τ_m. In reality, these three quantities appear as soon as we represent τ and ℓ in terms of the fundamental physical parameters ϵ, μ and σ. In the MKSA system, that is expressed in terms of mass M (Kg), length L (m), time T (s) and current I (A), the variables' dimensions, denoted with square brackets, are

$$\begin{aligned}[\mu] &= [L][M][T]^{-2}[I]^{-2},\\ [\epsilon] &= [L]^{-3}[M]^{-1}[T]^{4}[I]^{2},\\ [\sigma] &= [L]^{-3}[M]^{-1}[T]^{3}[I]^{2}.\end{aligned}$$

In Table 3 we summarize the physical parameter units in the MKSA system.

Table 3 : Parameter units in the MKSA system

	μ	ϵ	σ	τ	ℓ
L	1	-3	-3	0	1
M	1	-1	-1	0	0
T	-2	4	3	1	0
I	-2	2	2	0	0

Considering the numerical part of Table 3 as a 4×5 matrix, and remarking that the last two columns of the so-defined matrix contain just one non-zero unitary entry and that the last line is minus twice the second, the matrix rank is 3. Two parameters (τ and ℓ) can be expressed as functions of three others (μ, ϵ and σ). To this purpose, we seek for α, β, γ, c_1, c_2, and c_3 reals such that the following two ratios are dimensionless :

$$\tau/(\mu^{\alpha}\epsilon^{\beta}\sigma^{\gamma}) = O(1), \qquad \ell/(\mu^{c_1}\epsilon^{c_2}\sigma^{c_3}) = O(1).$$

The first ratio yields the following linear system

$$\begin{cases} \alpha - 3\beta - 3\gamma = 0 \\ \alpha - \beta - \gamma = 0 \\ -2\alpha + 4\beta + 3\gamma = 1 \\ -2\alpha + 2\beta + 2\gamma = 0 \end{cases}$$

whose solution is $\alpha = 0$, $\beta = 1$, and $\gamma = -1$ (the fourth equation coincides with the second one up to a multiplicative factor -2). We introduce the first quantity $\tau_e = \epsilon/\sigma$ and we have $\tau/\tau_e = O(1)$. For the second ratio, we have to find c_1, c_2, and c_3 solution of a similar linear system with right-hand side equal to $(1, 0, 0, 0)^t$. We thus get $c_1 = -1/2$, $c_2 = 1/2$, and $c_3 = -1$. We introduce $\ell^\star = (\sqrt{\epsilon/\mu})/\sigma$ and we have $\ell/\ell^\star = O(1)$. Since $\ell/\ell^\star = \mu\sigma\ell c = \mu\sigma\ell^2(c/\ell)$, a natural choice is to set $\tau_{em} = \ell/c$ and $\tau_m = \mu\sigma\ell^2$. The quantity τ_m is called magnetic diffusion time as the magnetic diffusion coefficient is $D_m = 1/(\mu\sigma)$ which has dimension $[L]^2[T]^{-1}$ and $\tau_m = \ell^2/D_m$. With these choices, $\tau_{em}^2 = \tau_e\tau_m$.

We note that τ and ℓ are fixed by the problem features. Depending on the physical parameters μ, ϵ, and σ we specify the time intervals and thus the EQS or MQS model to use. As an example, we consider a homogeneous system with $\ell = 1$ filled with either water or copper or corn oil, respectively, with $\mu = \mu_0$ and σ, ϵ given in Table 4. The time intervals for τ allowing to use different models are given in Table 4.

Table 4: Media and time ranges for the different models [10] (the notation e$\pm n$ stands for $10^{\pm n}$)

	water	copper	corn oil
ϵ	$81\epsilon_0$	ϵ_0	$3.1\epsilon_0$
σ	0.2	5.7e+7	5.e-11
ℓ^*	0.12	4.7e-11	1.e+8
τ_{em}	3.e-8	3.e-9	5.8e-9
Full eqs.	$[0, \tau_{em}[$	$[0, \tau_{em}[$	$[0, \tau_{em}[$
MQS	$[\tau_{em}$, 3.e-7 s$[$	$[\tau_{em}$, 3.e+2 s$[$	–
EQS	–	–	$[\tau_{em}$, 5.8e-1 s$[$
QSC	[3.e-7 s, $\infty[$	[3.e+2 s, $\infty[$	[5.8e-1 s, $\infty[$

V. GALILEAN ELECTRODYNAMICS OF MOVING MEDIA

We conclude with few words on the Galilean electrodynamics of moving media, a rather long subject to develop deeply here even if still open to research as many aspects have not been completely understood yet. From now on, quantities with "primes" are related to the moving reference system $\mathcal{R}'$ and those without are related to the fixed reference system $\mathcal{R}$. A Lorentz transformation acts on space-time coordinates as follows [11]

$$\begin{aligned} x' &= x - \gamma\, v\, t + (\gamma - 1)\tfrac{v(v\cdot x)}{|v|^2}, \\ t' &= \gamma(t - \tfrac{v\cdot x}{c^2}),\ \gamma = 1/\sqrt{1 - \tfrac{|v|}{c^2}}, \end{aligned} \qquad (15)$$

where v is the relative velocity between $\mathcal{R}'$ and $\mathcal{R}$ and $|v|$ its modulus. When $|v| \ll c$ (that yields

$\gamma \sim 1$), under the validity of the causality principle $\Delta x = |v|\Delta t \ll c\Delta t$, transformations (15) reduce to Galilean ones

$$x' = x - v\,t,\; t' = t. \tag{16}$$

It can be proven that, with a suitable re-definition of the involved fields, Galilean models (6)-(8) are co-variant (or form invariant) under transformations (16), and this is the origin of the "Galilean electromagnetism" terminology. For the fields, as given by Einstein and Laub in 1908 [12], we have

$$\begin{aligned} E' &= \gamma(E + v \times B) + (1-\gamma)\tfrac{v(v\cdot E)}{|v|^2}, \\ B' &= \gamma(B - \tfrac{v\times E}{c^2}) + (1-\gamma)\tfrac{v(v\cdot B)}{|v|^2}, \\ D' &= \gamma(D + \tfrac{v\times H}{c^2}) + (1-\gamma)\tfrac{v(v\cdot D)}{|v|^2}, \\ H' &= \gamma(H - v \times D) + (1-\gamma)\tfrac{v(v\cdot H)}{|v|^2}. \end{aligned} \tag{17}$$

To take the limit for $|v| \ll c$ is not only sufficient to set $\gamma \sim 1$ in (17). Indeed, one would obtain for example $E' = E + v\times B$ and $B' = B - (v\times E)/c^2$ which do not respect the group composition property (note that the group composition property is a key point to understand the validity of a physical transformation). Two limits appear by choosing $|v| \ll c$ AND either $e \ll cb$,

$$\begin{aligned} &E' = E + v \times B, && B' = B, \\ &D' = D + (v \times H)/c^2, && H' = H, \\ &\rho' = \rho - v \cdot J/c^2, && J' = J, \end{aligned} \tag{18}$$

or $e \gg cb$,

$$\begin{aligned} &E' = E, && B' = B - (v \times E)/c^2, \\ &D' = D, && H' = H - v \times D, \\ &\rho' = \rho, && J' = J - \rho v. \end{aligned} \tag{19}$$

Starting from (17) with $\gamma \sim 1$, if $e \ll cb$, the term $B - (v/c) \times (E/c)$ gives $b - (|v|/c)(e/c) \sim b$, thus we get (18). On the other hand, if $e \gg cb$, the two terms $(|v|/c)$ and (e/c) equilibrate each other and have to be kept, whereas $e + |v|b \sim e$ and thus (19) hold. Note that in the Galilean regime, we make the assumption that the force F and the charge q are invariant when going from $\mathcal{R}$ to $\mathcal{R}'$, *i.e.*, $F' = F$ and $q' = q$. The relation $F' = q'E'$ gives $F = q(E + v\times B)$ in the magnetic limit and $F = qE$ in the electric.

Constitutive relations as well depend on the considered Galilean limit. We recall that in the moving reference $\mathcal{R}'$, the constitutive relation between B and H reads $B' = \mu H'$. When reported all quantities to $\mathcal{R}$, in the magnetic limit, one has

$$\begin{aligned} &H = B/\mu, \\ &D \simeq \epsilon E + (\epsilon - \tfrac{1}{\mu c^2}) v \times B, \end{aligned}$$

but in the electric limit one should rather use

$$\begin{aligned} &H \simeq B/\mu - (\epsilon - \tfrac{1}{\mu c^2})\tfrac{v\times E}{c^2}, \\ &D = \epsilon E, \end{aligned}$$

with $c = c_u$. Similarly, for the potentials we have

$$\begin{aligned} &A' = A - \gamma\tfrac{vV}{c^2} + (\gamma - 1)\tfrac{v(v\cdot A)}{|v|^2}, \\ &V' = \gamma(V - v \cdot A). \end{aligned} \tag{20}$$

Two limits appear by choosing $|v| \ll c$ AND either $a \ll cV$, which implies $A' = A - \frac{vV}{c^2}$, $V' = V$, or $a \gg cV$, that yields $A' = A$, $V' = V - v \cdot A$.

VII. REMARKS AND CONCLUSIONS

Few remarks before concluding. First, the two-dimensional plot of Fig. 2 (Table 2 for gauge condition validity) can be used as a heuristic tool to specify the model to use. Its main advantage is to select important terms avoiding the computation of irrelevant ones. Second, the considered approach is local. This means that in a system composed of different media, it can happen that in a domain the MQS limit holds and in another domain the EQS limit has to be considered. The fields of the whole system cannot be computed under one single limit, and we have to consider the proper formulation according to the subdomain features. A nice example of this situation arises when one wishes to solve a RCL circuit, and has to use the MQS limit outside C and the EQS limit in C to explain how the magnetic and electric fields are generated by the current in the circuit. Third, the presented analysis relies on the use of dimensional analysis, a classical tool in Fluid Mechanics, that becomes powerful if driven by the experience of researchers (in this case, a mathematician and a physicist of fluids). This tool allows to make a very simple and didactic presentation of the subject, and to underline the key points when studying a physical phenomenon, namely which are the relevant parameters of the problem and thus how to obtain a reduced model, to analyze the consistency of the reduced model and its domain of validity. We believe that emphasis on dimensional reasoning would be useful to students in many branches of physics. We underline that analogous conclusions to the ones obtained in the present paper for the MQS limit can be obtained by asymptotic analysis [13] too. The EQS limit is more difficult to analyze and its asymptotic counterpart is still missing. The applicability of the quasi-static models was investigated firstly relying on a dimensional analysis and then making a connection with the characteristic times of the considered problem. We have underlined as the physical parameters of the problem as well as the sources of the fields determine the (high frequency or low frequency) model to use. If one works with potentials, the gauge condition to use has to be compatible with the problem physics.

REFERENCES

[1] M. Le Bellac and J.-M. Lévy-Leblond, “Galilean Electromagnetism,” *Il Nuovo Cimento*, vol. 14, pp. 217-233, 1973.

[2] J. R. Melcher and H. A. Haus, *Electromagnetic Fields and Energy*, Prentice Hall, 1980.

[3] M. de Montigny and G. Rousseaux, “On Some Applications of Galilean Electrodynamics of Moving Bodies,” *Am. J. Phys.*, vol. 75, pp. 984-992, 2007.

[4] G. I. Barenblatt, *Scaling*, Cambridge University Press, 2003.

[5] E. Guyon, J.-P. Hulin, L. Petit and C. D. Mitescu, *Physical Hydrodynamics*, Oxford University Press, 2001.

[6] T. Steinmetz, S. Kurz and M. Clemens, “Domains of Validity of Quasistatic and Quasistationary Field Approximations,” *COMPEL*, vol. 30, no. 4, pp. 1237-1247, 2011.

[7] O. D. Jefimenko, “A Neglected Topic in Relativistic Electrodynamics: Transformation of Electromagnetic Integrals”, *arXiv:physics/0509159v1*, pp. 1-9, 2005.

[8] J. A. Heras, “The c Equivalence Principle and the Correct Form of Writing Maxwell’s Equations,” *European Journal of Physics*, vol. 31, pp. 1177-1185, 2010.

[9] J. A. Stratton, *Electromagnetic Theory*, McGraw-Hill, New York, 1941.

[10] G. Benderskaya, *Numerical Methods for Transient Field-Circuit Coupled Simulations Based on the Finite Integration Technique and a Mixed Circuit Formulation*, PhD, 2007.

[11] H. Goldstein, *Classical Mechanics*, 2nd ed., Addison-Wesley Reading, MA, 1981.

[12] A. Einstein and J. Laub, 1908, articles available at `http://einstein-annalen.mpiwg-berlin.mpg.de/home`.

[13] H. Ammari, A. Buffa and J.-C. Nédélec, “A Justification of Eddy Currents Model for the Maxwell Equations,” *SIAM J. Appl. Math.*, vol. 60, no. 5, pp. 1805-1823, 2000.

Francesca Rapetti has studied mathematics at the University of Milan (IT) and got her degree in 1995. She then worked two years as junior researcher at the CRS4 Lab. in Sardinia (IT), in the group of applied mathematics. In 1997, thanks to an individual TMR fellowship from the European Community, she could reach the University of Pierre et Marie Curie in Paris (FR) and start a Ph.D. thesis that she defended in 2000. After a one-year post-doc in Paris, she got a permanent position as assistant professor in applied mathematics at the University of Nice (FR) where she defended her HdR in 2008. Her main research interests cover domain decomposition techniques for PDEs, Maxwell equations and Galilean electromagnetism, differential forms and Whitney finite elements in scientific computing, h, p, and hp-finite element/spectral element methods on simplices, numerical simulations for industrial applications, linear algebra and computer code development.

Germain Rousseaux has graduated both in Physics and Mechanical Engineering from the Grenoble Institute of Technology, he made his Ph.D. thesis in Paris 6 University (FR) on Hydrodynamics and Granular Physics. He reached the CNRS in 2007 and he is presently at the Dieudonné Laboratory of the University of Nice. He is a Natural Philosopher and a Maxwellian, mainly interested by the Physics of the Nineteenth century and its history. With Marc de Montigny, he demonstrated the existence of the Galilean Limits of Maxwell equations postulated by Lévy-Leblond and Le Bellac. As a true follower of

Maxwell, he advocates the physical interpretation in Classical Physics of both the vector and scalar potentials (the so-called Maxwell-Lodge effect) as well as the so-called gauge conditions. He has extended the mechanical analogy of Maxwell between fluid mechanics and electromagnetism to the case of acoustic waves. He is now working on the curved space-time extension of it: the so-called analogue gravity program where acoustic dumb holes mimic astrophysical black holes.

2011 INSTITUTIONAL MEMBERS

DTIC-OCP LIBRARY
8725 John J. Kingman Rd, Ste 0944
Fort Belvoir, VA 22060-6218

AUSTRALIAN DEFENCE LIBRARY
Northcott Drive
Canberra, A.C.T. 2600 Australia

BEIJING BOOK CO, INC
701 E Linden Avenue
Linden, NJ 07036-2495

DARTMOUTH COLLEGE
6025 Baker/Berry Library
Hanover, NH 03755-3560

DSTO EDINBURGH
AU/33851-AP, PO Box 830470
Birmingham, AL 35283

SIMEON J. EARL – BAE SYSTEMS
W432A, Warton Aerodome
Preston, Lancs., UK PR4 1AX

ENGINEERING INFORMATION, INC
PO Box 543
Amsterdam, Netherlands 1000 Am

ETSE TELECOMUNICACION
Biblioteca, Campus Lagoas
Vigo, 36200 Spain

GA INSTITUTE OF TECHNOLOGY
EBS-Lib Mail code 0900
74 Cherry Street
Atlanta, GA 30332

TIMOTHY HOLZHEIMER
Raytheon
PO Box 1044
Rockwall, TX 75087

HRL LABS, RESEARCH LIBRARY
3011 Malibu Canyon
Malibu, CA 90265

IEE INSPEC
Michael Faraday House
6 Hills Way
Stevenage, Herts UK SG1 2AY

INSTITUTE FOR SCIENTIFIC INFO.
Publication Processing Dept.
3501 Market St.
Philadelphia, PA 19104-3302

LIBRARY – DRDC OTTAWA
3701 Carling Avenue
Ottawa, Ontario, Canada K1A OZ4

LIBRARY of CONGRESS
Reg. Of Copyrights
Attn: 407 Deposits
Washington DC, 20559

LINDA HALL LIBRARY
5109 Cherry Street
Kansas City, MO 64110-2498

MISSOURI S&T
400 W 14th Street
Rolla, MO 56409

MIT LINCOLN LABORATORY
Periodicals Library
244 Wood Street
Lexington, MA 02420

NATIONAL CHI NAN UNIVERSITY
Lily Journal & Book Co, Ltd
20920 Glenbrook Drive
Walnut, CA 91789-3809

JOHN NORGARD
UCCS
20340 Pine Shadow Drive
Colorado Springs, CO 80908

OSAMA MOHAMMED
Florida International University
10555 W Flagler Street
Miami, FL 33174

NAVAL POSTGRADUATE SCHOOL
Attn:J. Rozdal/411 Dyer Rd./ Rm 111
Monterey, CA 93943-5101

NDL KAGAKU
C/0 KWE-ACCESS
PO Box 300613 (JFK A/P)
Jamaica, NY 11430-0613

OVIEDO LIBRARY
PO BOX 830679
Birmingham, AL 35283

DAVID PAULSEN
E3Compliance
1523 North Joe Wilson Road
Cedr Hill, TX 75104-1437

PENN STATE UNIVERSITY
126 Paterno Library
University Park, PA 16802-1808

DAVID J. PINION
1122 E Pike Street #1217
SEATTLE, WA 98122

KATHERINE SIAKAVARA
Gymnasiou 8
Thessaloniki, Greece 55236

SWETS INFORMATION SERVICES
160 Ninth Avenue, Suite A
Runnemede, NJ 08078

YUTAKA TANGE
Maizuru Natl College of Technology
234 Shiroya
Maizuru, Kyoto, Japan 625-8511

TIB & UNIV. BIB. HANNOVER
DE/5100/G1/0001
Welfengarten 1B
Hannover, Germany 30167

UEKAE
PO Box 830470
Birmingham, AL 35283

UNIV OF CENTRAL FLORIDA
4000 Central Florida Boulevard
Orlando, FL 32816-8005

UNIVERSITY OF COLORADO
1720 Pleasant Street, 184 UCB
Boulder, CO 80309-0184

UNIVERSITY OF KANSAS – WATSON
1425 Jayhawk Blvd 210S
Lawrence, KS 66045-7594

UNIVERSITY OF MISSISSIPPI
JD Williams Library
University, MS 38677-1848

UNIVERSITY LIBRARY/HKUST
Clear Water Bay Road
Kowloon, Honk Kong

CHUAN CHENG WANG
8F, No. 31, Lane 546
MingCheng 2nd Road, Zuoying Dist
Kaoshiung City, Taiwan 813

THOMAS WEILAND
TU Darmstadt
Schlossgartenstrasse 8
Darmstadt, Hessen, Germany 64289

STEVEN WEISS
US Army Research Lab
2800 Powder Mill Road
Adelphi, MD 20783

YOSHIHIDE YAMADA
NATIONAL DEFENSE ACADEMY
1-10-20 Hashirimizu
Yokosuka, Kanagawa,
Japan 239-8686

APPLIED COMPUTATIONAL ELECTROMAGNETICS SOCIETY JOURNAL
http://aces.ee.olemiss.edu

INFORMATION FOR AUTHORS

PUBLICATION CRITERIA

Each paper is required to manifest some relation to applied computational electromagnetics. **Papers may address general issues in applied computational electromagnetics, or they may focus on specific applications, techniques, codes, or computational issues.** While the following list is not exhaustive, each paper will generally relate to at least one of these areas:

1. **Code validation.** This is done using internal checks or experimental, analytical or other computational data. Measured data of potential utility to code validation efforts will also be considered for publication.

2. **Code performance analysis.** This usually involves identification of numerical accuracy or other limitations, solution convergence, numerical and physical modeling error, and parameter tradeoffs. However, it is also permissible to address issues such as ease-of-use, set-up time, run time, special outputs, or other special features.

3. **Computational studies of basic physics.** This involves using a code, algorithm, or computational technique to simulate reality in such a way that better, or new physical insight or understanding, is achieved.

4. **New computational techniques** or new applications for existing computational techniques or codes.

5. **"Tricks of the trade"** in selecting and applying codes and techniques.

6. **New codes, algorithms, code enhancement, and code fixes.** This category is self-explanatory, but includes significant changes to existing codes, such as applicability extensions, algorithm optimization, problem correction, limitation removal, or other performance improvement. **Note: Code (or algorithm) capability descriptions are not acceptable, unless they contain sufficient technical material to justify consideration.**

7. **Code input/output issues.** This normally involves innovations in input (such as input geometry standardization, automatic mesh generation, or computer-aided design) or in output (whether it be tabular, graphical, statistical, Fourier-transformed, or otherwise signal-processed). Material dealing with input/output database management, output interpretation, or other input/output issues will also be considered for publication.

8. **Computer hardware issues.** This is the category for analysis of hardware capabilities and limitations of various types of electromagnetics computational requirements. Vector and parallel computational techniques and implementation are of particular interest.

Applications of interest include, but are not limited to, antennas (and their electromagnetic environments), networks, static fields, radar cross section, inverse scattering, shielding, radiation hazards, biological effects, biomedical applications, electromagnetic pulse (EMP), electromagnetic interference (EMI), electromagnetic compatibility (EMC), power transmission, charge transport, dielectric, magnetic and nonlinear materials, microwave components, MEMS, RFID, and MMIC technologies, remote sensing and geometrical and physical optics, radar and communications systems, sensors, fiber optics, plasmas, particle accelerators, generators and motors, electromagnetic wave propagation, non-destructive evaluation, eddy currents, and inverse scattering.

Techniques of interest include but not limited to frequency-domain and time-domain techniques, integral equation and differential equation techniques, diffraction theories, physical and geometrical optics, method of moments, finite differences and finite element techniques, transmission line method, modal expansions, perturbation methods, and hybrid methods.

Where possible and appropriate, authors are required to provide statements of quantitative accuracy for measured and/or computed data. This issue is discussed in "Accuracy & Publication: Requiring, quantitative accuracy statements to accompany data," by E. K. Miller, *ACES Newsletter,* Vol. 9, No. 3, pp. 23-29, 1994, ISBN 1056-9170.

SUBMITTAL PROCEDURE

All submissions should be uploaded to ACES server through ACES web site (http://aces.ee.olemiss.edu) by using the upload button, journal section. Only pdf files are accepted for submission. The file size should not be larger than 5MB, otherwise permission from the Editor-in-Chief should be obtained first. Automated acknowledgment of the electronic submission, after the upload process is successfully completed, will be sent to the corresponding author only. It is the responsibility of the corresponding author to keep the remaining authors, if applicable, informed. Email submission is not accepted and will not be processed.

EDITORIAL REVIEW

In order to ensure an appropriate level of quality control, papers are peer reviewed. They are reviewed both for technical correctness and for adherence to the listed guidelines regarding information content and format.

PAPER FORMAT

Only camera-ready electronic files are accepted for publication. The term **"camera-ready" means that the material is neat, legible, reproducible, and in accordance with the final version format listed below.**

The following requirements are in effect for the final version of an ACES Journal paper:

1. The paper title should not be placed on a separate page.

The title, author(s), abstract, and (space permitting) beginning of the paper itself should all be on the first page. The title, author(s), and author affiliations should be centered (center-justified) on the first page. The title should be of font size 16 and bolded, the author names should be of font size 12 and bolded, and the author affiliation should be of font size 12 (regular font, neither italic nor bolded).

2. An abstract is required. The abstract should be a brief summary of the work described in the paper. It should state the computer codes, computational techniques, and applications discussed in the paper (as applicable) and should otherwise be usable by technical abstracting and indexing services. The word "Abstract" has to be placed at the left margin of the paper, and should be bolded and italic. It also should be followed by a hyphen (—) with the main text of the abstract starting on the same line.

3. All section titles have to be centered and all the title letters should be written in caps. The section titles need to be numbered using roman numbering (I. II. ….)

4. Either British English or American English spellings may be used, provided that each word is spelled consistently throughout the paper.

5. Internal consistency of references format should be maintained. As a guideline for authors, we recommend that references be given using numerical numbering in the body of the paper (with numerical listing of all references at the end of the paper). The first letter of the authors' first name should be listed followed by a period, which in turn, followed by the authors' complete last name. Use a coma (,) to separate between the authors' names. Titles of papers or articles should be in quotation marks (" "), followed by the title of journal, which should be in italic font. The journal volume (vol.), issue number (no.), page numbering (pp.), month and year of publication should come after the journal title in the sequence listed here.

6. Internal consistency shall also be maintained for other elements of style, such as equation numbering. Equation numbers should be placed in parentheses at the right column margin. All symbols in any equation have to be defined before the equation appears or right immediately following the equation.

7. The use of SI units is strongly encouraged. English units may be used as secondary units (in parentheses).

8. Figures and tables should be formatted appropriately (centered within the column, side-by-side, etc.) on the page such that the presented data appears close to and after it is being referenced in the text. When including figures and tables, all care should be taken so that they will appear appropriately when printed in black and white. For better visibility of paper on computer screen, it is good to make color figures with different line styles for figures with multiple curves. Colors should also be tested to insure their ability to be distinguished after black and white printing. Avoid the use of large symbols with curves in a figure. It is always better to use different line styles such as solid, dotted, dashed, etc.

9. A figure caption should be located directly beneath the corresponding figure, and should be fully justified.

10. The intent and meaning of all text must be clear. For authors who are not masters of the English language, the ACES Editorial Staff will provide assistance with grammar (subject to clarity of intent and meaning). However, this may delay the scheduled publication date.

11. Unused space should be minimized. Sections and subsections should not normally begin on a new page.

ACES reserves the right to edit any uploaded material, however, this is not generally done. It is the author(s) responsibility to provide acceptable camera-ready files in pdf and MSWord formats. Incompatible or incomplete files will not be processed for publication, and authors will be requested to re-upload a revised acceptable version.

COPYRIGHTS AND RELEASES

Each primary author must execute the online copyright form and obtain a release from his/her organization vesting the copyright with ACES. Both the author(s) and affiliated organization(s) are allowed to use the copyrighted material freely for their own private purposes.

Permission is granted to quote short passages and reproduce figures and tables from and ACES Journal issue provided the source is cited. Copies of ACES Journal articles may be made in accordance with usage permitted by Sections 107 or 108 of the U.S. Copyright Law. This consent does not extend to other kinds of copying, such as for general distribution, for advertising or promotional purposes, for creating new collective works, or for resale. The reproduction of multiple copies and the use of articles or extracts for commercial purposes require the consent of the author and specific permission from ACES. Institutional members are allowed to copy any ACES Journal issue for their internal distribution only.

PUBLICATION CHARGES

All authors are allowed for 8 printed pages per paper without charge. Mandatory page charges of $75 a page apply to all pages in excess of 8 printed pages. Authors are entitled to one, free of charge, copy of the printed journal issue in which their paper was published. Additional reprints are available for $ 50. Requests for additional re-prints should be submitted to the managing editor or ACES Secretary.

Corresponding author is required to complete the online form for the over page charge payment right after the initial acceptance of the paper is conveyed to the corresponding author by email.

ACES Journal is abstracted in INSPEC, in Engineering Index, DTIC, Science Citation Index Expanded, the Research Alert, and to Current Contents/Engineering, Computing & Technology.